Doctoral Dissertation
Doctoral Program in Electrical, Electronics and Communications Engineering
(37^{th} Cycle)

Development of Molecularly Imprinted Polymers by Advanced Technologies

By

Elena Camilli

******

Supervisors:
Prof. M. Cocuzza
Prof. F. Frascella
Dr. S. L. Marasso

Doctoral Examination Committee:
Prof. Annalisa Chiappone, Università degli Studi di Cagliari
Dr. Nicola Coppedè, CNR-IMEM
Dr. Gianluca Di Profio, CNR-ITM
Prof. Arnaud Spangenberg, Institut de Science des Matériaux de Mulhouse (IS2M)

Politecnico di Torino
2025

Declaration

I hereby declare that, the contents and organization of this dissertation constitute my own original work and does not compromise in any way the rights of third parties, including those relating to the security of personal data.

Elena Camilli

2025

* This dissertation is presented in partial fulfillment of the requirements for **Ph.D. degree** in the Graduate School of Politecnico di Torino (ScuDo).

To the amazing women I have had the honour of looking up to in my life, who have shown me the path to be free and independent.

To my parents, who have given me the privilege to follow it.

Acknowledgments

First and foremost, I thank my supervisors for guiding me through this journey, and for the trust they placed in me: Prof. Matteo Cocuzza, Prof. Francesca Frascella, and Dr. Simone Marasso. A special mention to Ignazio Roppolo, who provided essential support to my work. I also extend my gratitude to Valentina Bertana for being there from the beginning as a source of advice and help.

I thank Professor T. Minami and his entire team for the opportunity to work in their laboratories and to experience a nation that has forever remained in my heart. A special thanks to Wei Tang for his help and friendship, and to Ms. Tsuchiya Mina, Ms. Kato, and Mr. Tsuchiya for their kindness.

I want to express my heartfelt thanks to Arianna Leone, Sara Vallero, and Arianna Diano, talented and dedicated engineers who contributed to my work during their master's thesis projects. Guiding you was an enriching experience, and engaging with you was always insightful.

Abstract

Molecularly Imprinted Polymers (MIPs) as artificial receptors have received considerable scientific attention in the past few decades, as material for biomimetic molecular recognition. This thesis explores the fabrication of MIPs by Additive Manufacturing (AM), an emerging and largely unexplored field. Specifically, Digital Light Processing (DLP) technology was employed to fabricate 3D-printed, self-standing MIP structures with tailored geometries and functionalities.

The developed MIPs target environmental remediation applications, focusing on the selective removal of antibiotics from water. Oxytetracycline (OTC), a widely used antibiotic and common environmental contaminant, was chosen as the template molecule. The optimized MIP formulation also included Methacrylic Acid as the functional monomer, Dipropylene Glycol Diacrylate as the crosslinker, and Dimethyl Sulfoxide as the solvent. Density Functional Theory (DFT) calculations were used to model the interactions between the template and functional monomer, guiding the formulation development. Experimental work revealed that 3D-printed MIPs exhibit promising selectivity and removal efficiency, influenced by factors such as geometry, surface area, and polymer composition. Additional investigations into micrometric porosity and reusability were conducted, though challenges in reproducibility and structural integrity highlighted areas for improvement. The results underscore the potential of 3D-printed MIPs as a platform for advanced environmental remediation and sensing solutions, while also identifying key challenges and opportunities for future research.

Beyond environmental remediation, the versatility of MIPs was further explored in electrochemical sensing applications. A side project investigated the electrodeposition of MIPs onto nanostructured gold electrodes, aiming to integrate them into electrochemical sensor platforms. The electrodeposited MIPs were tailored for the selective detection of OTC, demonstrating their potential in molecular recognition-based sensors.

Contents

List of Figures

List of Tables

Chapter 1

Introduction

1.1 Research Framework And Objectives

Water contamination by antibiotics has become a pressing environmental issue, exacerbated by their extensive use in medicine and agriculture. These pollutants contribute to antimicrobial resistance and pose significant ecological and health risks. Molecular Imprinting Polymers (MIPs) offer a promising solution for the targeted removal of such pollutants from aquatic environments by creating synthetic materials with selective binding sites tailored to specific target molecules. Despite the advancements, conventional MIP formats, such as particles and thin films, have limitations in scalability and integration into functional devices. Additive manufacturing, particularly Digital Light Processing (DLP) 3D printing, provides a transformative approach by enabling the fabrication of self-standing and geometrically complex MIP structures.

The primary objective of this thesis is to explore the potential of 3D printing in MIP fabrication, representing an innovative methodology with limited existing precedent. Specifically, the research focuses on the development of materials for environmental remediation, targeting the removal of antibiotics from water. By integrating experimental investigations with computational modelling, this work aims to bridge the molecular recognition capabilities of MIPs with practical engineering applications.

Additionally, as a secondary project, this thesis examines the potential of electrodeposited MIPs for integration into sensor systems designed for antibiotic detection. MIPs have demonstrated considerable promise in sensing applications, frequently serving as recognition elements in electrochemical sensors due to their high specificity for target analytes. The design and fabrication of such electrochemical sensors were conducted during a six-month internship at the University of Tokyo, under the supervision of Professor T. Minami.

1.4 Thesis Outline

The thesis begins with the current *Introduction*, which provides a comprehensive overview of the research framework, the structure of the dissertation, and the objectives pursued. The following chapter, *Molecularly Imprinted Polymers*, discusses the fundamental principles behind MIPs, including their design and synthesis. The chapter also explores various polymerization methods and application fields, with a specific focus on environmental remediation.

The third chapter, *Development of 3D-printed MIPs*, focuses on the experimental methodology to 3D print MIPs. This includes the rationale behind the experiments, the description of the formulation of printable resins, and an overview on the characterization techniques. Computational insights derived from DFT calculations are integrated into this chapter to support the optimization in the design of the formulations. Subsequently, the chapter on *Experimental Apparatus and Methodologies* describes the materials, equipment, and techniques employed throughout the study.

An additional chapter, *Electrodeposited MIPs*, examines the use of electropolymerization as an alternative fabrication method. This chapter highlights the specific applications of electrodeposited MIPs in sensor development, discussing their performance, challenges in reproducibility, and potential integration into advanced sensing devices like transistor-based platforms.

Chapter 2

Molecularly Imprinted Polymers

Biological living systems have, during billions of years of evolution, developed an endless plethora of strategies to detect and respond to different internal and external stimuli, ensuring their adaptation to changing environmental conditions. The possible stimuli can be classified into two main categories: physical (such as electrical, mechanical, or light stimulation) and chemical [1]. In the latter, a prominent role is played by molecular recognition [2]. During evolution, living species have optimized enzymes, antibodies, and receptors, to recognize molecules, as a fundamental scheme to guarantee their survival and proliferation [3]. With the development of bioengineering devices, science tried to replicate this strategy, striving to mimic the level of complexity of Nature in systems controllable by humans [4][5].

In this frame, **biological receptors** play paramount importance in biomedical and bioengineering devices, serving as elements capable of detecting and quantifying specific biological molecules in a wide range of applications [6]. The most conventional way to use these types of receptors is by employing them directly into the devices, as in standard Enzyme-Linked Immunosorbent Assay (ELISA) [7] as well as in biosensors, through surface interaction [8] and functionalization [9][10][11]. However, their inherent fragility and instability outside their native environment pose challenges, complicating industrial integration and limiting their

applicability [12]. Additionally, natural receptors are unavailable for some target molecules [13].

In this context, **Molecular Imprinting Technology** (MIT) addresses these limitations by creating synthetic recognition materials, emerging as an innovative approach. Indeed, MIT directly employs the molecules to be recognized as a template during the fabrication process to obtain a synthetic mould of the molecules [14]. The most extensively developed products of MIT are **Molecularly Imprinted Polymers** (MIPs).

MIPs are usually referred to as *artificial antibodies*, a simplistic but insightful definition that contains their primary function: synthetic materials designed to replicate the molecular recognition capabilities of biological receptors (Figure 1).

Through molecular imprinting, a three-dimensional polymer matrix is synthesized in the presence of the molecule of interest, called the template. Functional and crosslinking monomers are copolymerized around this template, incorporating it into the growing polymer network [13]. Once the polymerization process is complete, the template is removed by washing, leaving behind cavities that match the template molecule in both shape and chemical functionality. This imparts the polymer with a form of memory allowing it to selectively recognize and bind the target molecule in future applications.

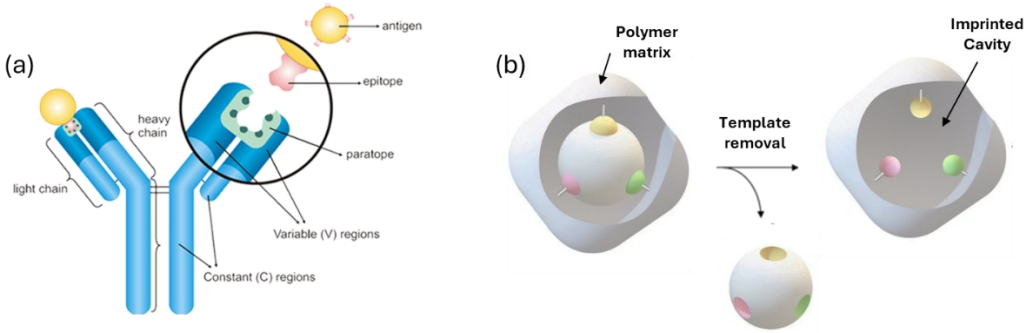

Figure 1: Schematic comparison between a natural receptor (a), and a synthetic MIP (b).

Before diving into the functioning and fabrication of MIPs, the historical background is briefly described in the next section.

2.1 Historical Background

The concept of molecular imprinting can be traced back to the 1930s, when synthetic strategies for "material memory" were first considered by the chemist M.V. Polyakov [15]. However, the modern development of MIPs is conventionally attributed to Wulff and colleagues in the 1970s [16], who introduced the idea of using covalent bonding interactions between functional monomers and a template molecule during a polymerization process. A similar study was published simultaneously by Takagishi et al. [17]. This covalent approach was a significant step in achieving molecular imprinting, but it had limitations in terms of practicality and the range of molecules that could be imprinted.

A few years later, Mosbach and his team proposed a non-covalent imprinting approach [18], where functional monomers form non-covalent interactions (e.g. hydrogen bonding, electrostatic interactions) with the template. These studies are considered the milestones of molecular imprinting techniques.

From this point on, MIP research expanded rapidly (Figure 2). The non-covalent approach paved the way for MIPs to be used in practical applications due to easier removal of the template after polymerization and the possibility of creating imprints for target molecules of all sizes and types, including ions [19], macromolecules [20], viruses [21] and even micro-organisms and cells [22]. A wide range of functional monomers and crosslinkers, as well as organic solvents or aqueous media, have been explored.

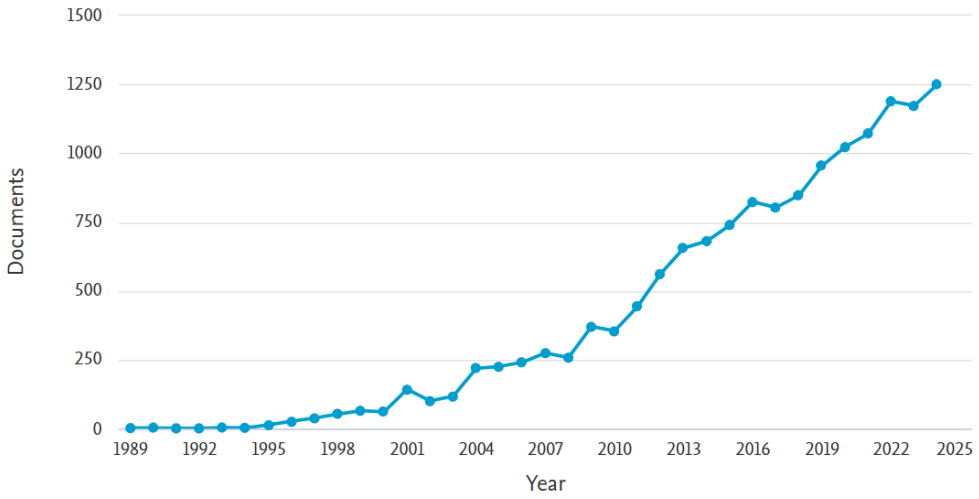

Figure 2: Trend of the publication regarding MIPs, between 1989 and 2024. Via Scoups.

The techniques developed in the following decades diversified significantly, and as MIPs matured as a technology, their applications expanded beyond simple separation processes (Figure 3). They became key materials in sensing, biomedical, and environmental applications.

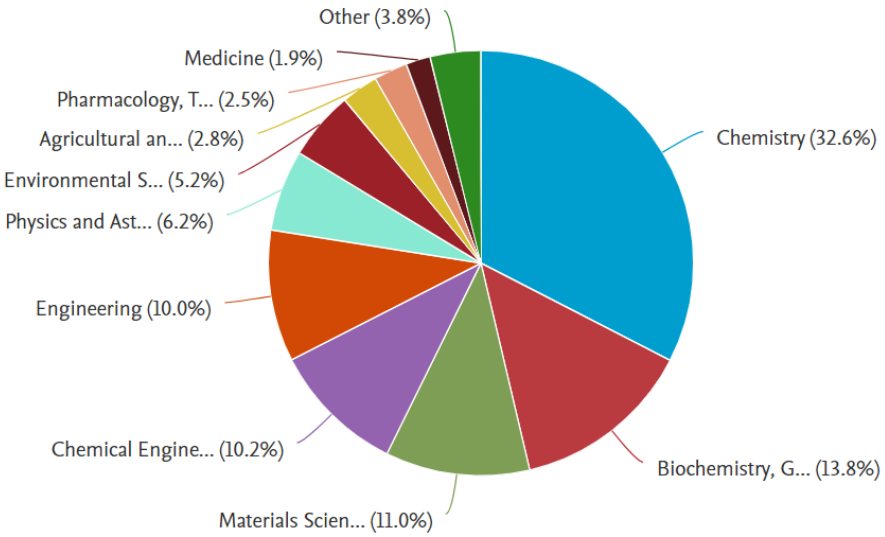

Figure 3: Documents published between 1989 and 2024, divided into subject areas. Via Scopus.

Moreover, the development of combinatorial chemistry and high-throughput screening methods allowed for more efficient optimization of MIP formulations. An overview of the main polymerization methods and the application fields will be presented in the following paragraphs.

2.2 Fundamentals of MIPs: Mechanisms and Building Blocks

The ability of MIPs to selectively bind target molecules stems from their fabrication process, which involves polymerizing functional monomers around a template molecule, followed by the removal of such template. This leaves behind cavities structurally and chemically tailored to the template, allowing for high specificity in binding. The schematic process can be visualized in the image below (Figure 4).

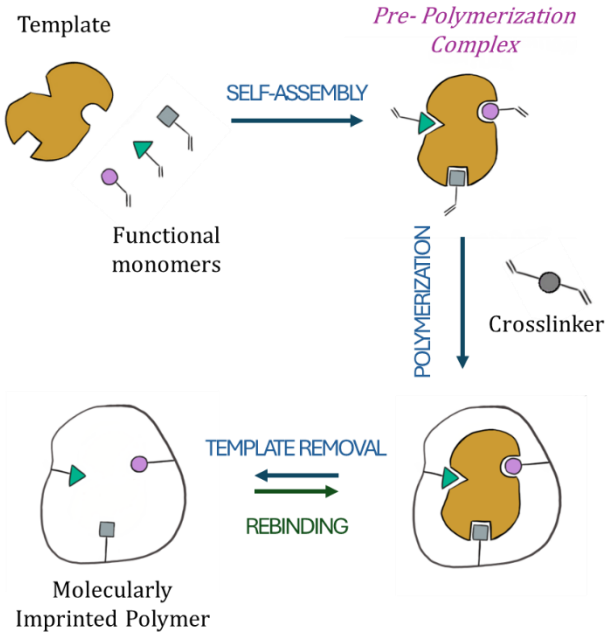

Figure 4: Simplified illustration of the molecular imprinting process.

It's important to remark that MIPs mimic the function of biological receptors, but in terms of structure, they differ significantly, as extensively explained in the reference work of K. Haupt et al [13]. In proteins, amino acids are organized in a defined sequence, resulting in a precise three-dimensional structure. In contrast, MIPs incorporate monomers randomly, with uncontrolled chain lengths, and a high degree of crosslinking that further disorganizes the network. While imprinting creates specific binding sites, these are often heterogeneous due to complex equilibria during template-monomer interaction and polymerization. This can lead to uneven pore sizes and slow mass transfer, as binding sites are buried within the polymer. These characteristics can limit MIPs from substituting in certain applications the biological counterpart.

The choice of ingredients in the design of MIPs is crucial because each component directly influences the polymer's performance [23].

2.2.1 Template

At the core of MIP functionality is the template molecule, which represents the specific molecule that the MIP is designed to recognize. The template should respect some basic characteristics, such as being soluble in the imprinting conditions. The template should remain chemically stable throughout the

polymerization process and should not interfere with or hinder the reaction [24]. Moreover, and most importantly, the template molecule must contain some functional groups capable of forming reversible or non-reversible bonds with the functional monomers, usually polar groups such as carbonyl (-C=O), carboxyl (-COOH), amino ($-NH_2$), or hydroxyl (-OH) groups [25].

Sizes and characteristics of the template molecule drive the choice of the fabrication technique. For example, while small molecules are supposed to diffuse through the polymer matrix of a bulk/particle MIP, in the case of macromolecules, the imprinting should take place on the polymer's surface [26].

After the polymerization process in MIP synthesis, the template molecule is removed from the polymer, to expose the imprinted cavities that match its shape, size, and functional groups. For effective removal, the template must be chosen such that it is soluble in the washing solvents without damaging the polymer matrix or altering the imprinted structure [27]. A significant concern with template removal is incomplete extraction, where residual template molecules remain trapped in the polymer matrix. These residuals can cause "template leakage", where traces of the original template leach out during subsequent applications. This not only interferes with the rebinding of the target molecule but can also result in false positives or reduced specificity, particularly in analytical or sensing applications. In some recent studies, this issue is addressed by employing *dummy templates* or *pseudo-templates*, namely alternative molecules that differ slightly from the target yet are capable of creating specific binding sites [28].

2.2.2 Functional Monomer

The selection of functional monomers is just as critical as the template. These monomers form chemical interactions with the template before the polymerization process, with covalent or non-covalent bonds, depending on the type of MIP (the two different strategies are described in Section 2.3). The nature and strength of these interactions determine how well the polymer can "remember" the template once is removed.

The design of the MIP must therefore carefully consider the functional groups present in both the template and the monomers to create a complex as stable as possible, especially in the case of non-covalent MIPs. Generally, alkaline templates pair with acidic monomers such as methacrylic acid (MAA) or acrylic acid (AA), acidic templates tend to associate with basic monomers like 2-vinylpyridine (2-VP),

and neutral templates are compatible with acidic or neutral monomers, such as styrene or acrylamide (AM) [25]. Some of the most commonly used functional monomers [29][24][30] for covalent and non-covalent imprinting are depicted in Figure 5 and Figure 6 respectively.

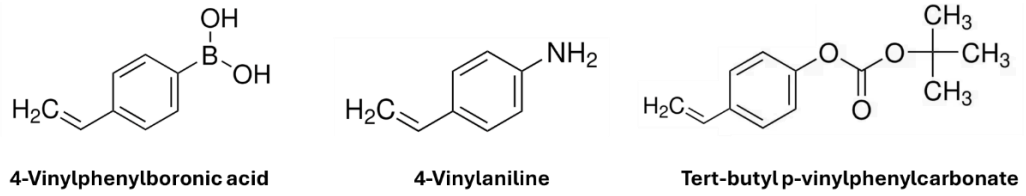

Figure 5: Example of functional monomers employed for covalent imprinting

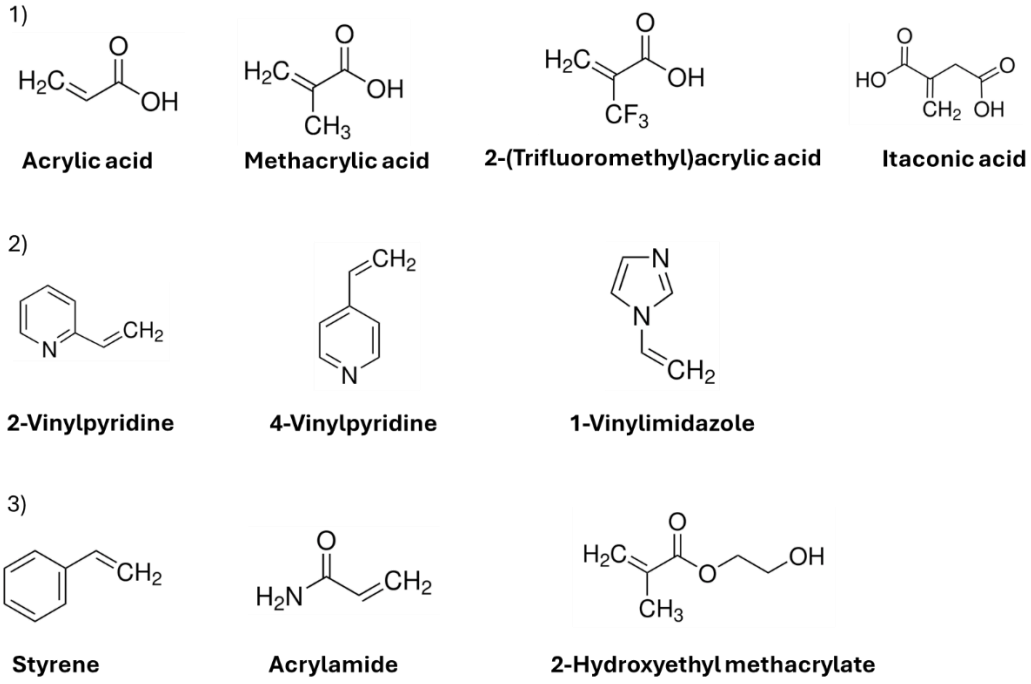

Figure 6: Example of functional monomers employed for non-covalent imprinting, containing 1) acidic, 2) basic, and 3) neutral functional groups.

The choice of the ratio between template and functional monomers is one of the key aspects of MIP design. In the covalent approach, the number of functional monomers that bind to the template is stoichiometrically determined [23]. Conversely, in the non-covalent approach, the molar ratio between the template and the functional monomers must be optimized empirically or computationally.

As a general indication, a lower template-to-monomer ratio may induce a reduced number of binding sites in the polymer, because the monomer-monomer interaction would prevail over the template-monomer [25]. On the other side, an excessive ratio may lead to the formation of heterogeneous binding pockets, increasing non-specific binding [31]. Different studies report the successful employment of more than one functional monomer [32], even if the optimization process needs to take into account more variables, becoming more complex.

Last but not least, it's important to consider that the functional monomer acts as the bridge between the template and the polymeric framework, thus it should have a part that binds to the template and one that polymerizes with the crosslinker [33].

2.2.3 Crosslinker

The crosslinker, while often overlooked in the design of MIPs, is essential in preserving the structural integrity of the polymer. They form the framework of the template-functional monomer complex and help maintain the shape and functionality of the binding sites once the template is removed. The choice of crosslinking agent and its concentration must be balanced [23].

Crosslinking monomers typically contain two or more reactive groups (e.g., divinyl compounds like divinylbenzene or diacrylate compounds like ethylene glycol dimethacrylate). These reactive groups allow the monomer to form connections with multiple polymer chains, creating a three-dimensional network structure. Some commonly used crosslinkers are shown in Figure 7.

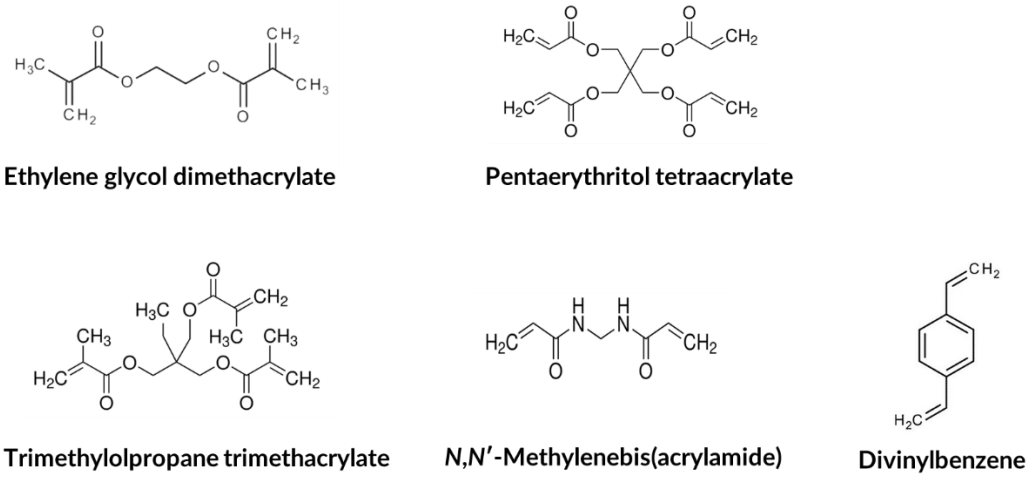

Figure 7: Example of commonly employed crosslinking monomers in molecular imprinting.

The amount and type of monomer determine the final MIP's crosslinking density, that is the number of crosslinks between chains, present within a polymer network per unit volume or molecular weight (Figure 8). A high crosslinking density may result in a more rigid and stable polymer, but it can also make the binding sites less accessible to the target molecule. Conversely, low crosslinking might enhance flexibility and accessibility but at the cost of the polymer's stability. Accordingly, the choice of crosslinkers must balance the two features, aligning with the application's specific needs.

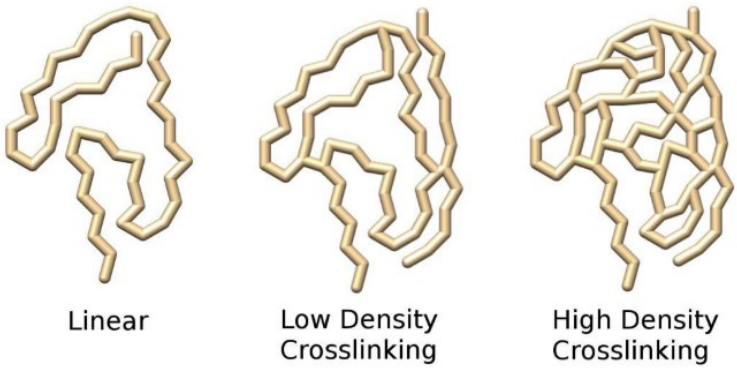

Figure 8: Schematic depiction of increasing crosslinking density. Reprint from [29].

2.2.3 Initiators

The choice of initiator depends on the polymerization method and the specific conditions under which the MIP is synthesized. Additionally, the initiator must be

compatible with all the other ingredients and the solvent environment. In the case of MIPs fabricated by free radical polymerization, the reaction may be initiated thermally or photochemically. In the first case, azobisisobutyronitrile (AIBN) and benzoyl peroxide are widely used [24].

On the other hand, photopolymerized MIPs are often prepared using conventional UV-A photopolymerization at wavelengths around 365 nm. At this wavelength many photoinitiators are active, such as 2-hydroxy-2-methylpropiophenone and phenylbis(2,4,6-trimethylbenzoyl)phosphine oxide (BAPO), while monomers like acrylates demonstrate weak absorption, ensuring their relative stability during the process [34]. The molecular structures of the cited initiators are shown in Figure 9.

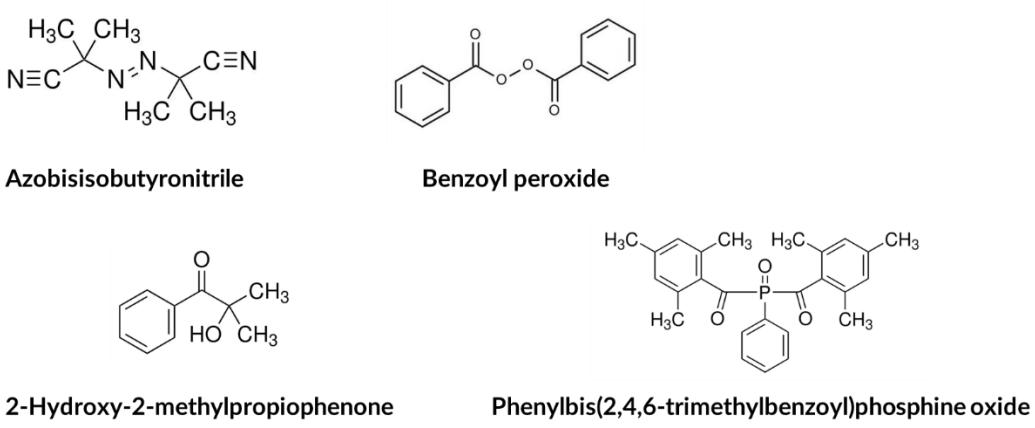

Figure 9: Some of the most commonly employed initiators.

2.2.4 Solvent

The solvent, or porogen, used in the polymerization process also plays a pivotal role. It influences the final MIP's porosity and morphology, directly affecting the polymer's ability to host and release the template molecules. A well-chosen solvent can facilitate the proper dissolution of the template and the interaction between the template and the monomers. This is particularly true in the case of non-covalent MIP, where the polarity of the solvent affects the pre-polymerization complex. Less polar solvents facilitate polar non-covalent interactions, while more polar solvents tend to dissociate such interactions [23].

2.3 Molecular Imprinting Strategies

As just seen, the simplest and most typical MIP synthesis involves a template, a functional monomer, a crosslinker, a polymerization initiator, and a solvent. The functional monomer interacts with the template during the imprinting process, playing a crucial role in forming the functional groups within the binding sites of the MIP.

Based on the nature of these bonds, MIPs are generally classified into **covalent** and **non-covalent** types. This fundamental categorization of molecular imprinting strategies shapes the resulting polymer's design and performance. As seen in the introduction paragraph, the two approaches derive from the two basilar studies of Wulff [16] and Mosbach [18], respectively. The differences, along with their respective advantages and limitations, will be highlighted in the next sections.

2.2.1 Covalent MIPs

In the covalent MIPs, the template is bound to the functional monomer by reversible covalent linkages before polymerization, meaning a chemical synthesis is required. Not without reason this protocol is referred to as the *chemist approach* by Haupt [13]. After polymerization, these covalent bonds are cleaved to release the template, leaving behind specific binding sites. The same covalent bond is re-formed when the target molecule binds to the MIP. The process is schematically depicted in Figure 10.

The most intuitive advantage of this technique lies in the durability of the complex during the polymerization, guaranteeing a high level of precision in the imprinting, a homogeneous distribution of the binding sites, and minimization of non-specific sites [24]. The strength of the complex does not come without disadvantages: difficulty in the removal of the template during the de-binding procedure, and slow kinetics during the rebinding [35].

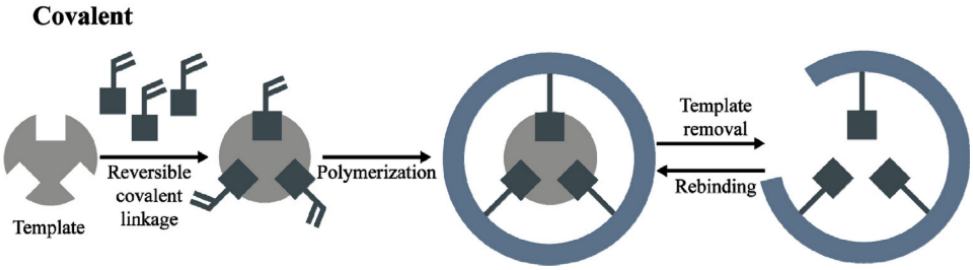

Figure 10: Schematic representation of the covalent imprinting strategy in MIP synthesis. Adapted from [36]

2.2.2 Non-covalent MIPs

Mosbach's non-covalent approach [18] follows the fact that the biological recognition mechanisms imply non-weak interactions. This approach is also known as the *self-assembly approach* due to the spontaneous assembly of the functional monomers around the template, by weak forces [13], as illustrated in Figure 11. The types of interaction usually employed are for example hydrogen bonds, ionic bonds, van der Waals forces, and hydrophobic effect [37].

The lower strength of these forces to covalent bonds allows easier removal of the template and in general, a more straightforward process, because the template molecule does not require chemical modification prior to polymerization. Also, it's a quite flexible method, considering the great variety of functional monomers to choose from, depending on the desired template. All these characteristics lead to the fact that the non-covalent approach is by far the most employed imprinting strategy. The disadvantages of this approach are complementary to the covalent one: heterogeneous binding sites [38], the presence of non-specific sites due to non-reacted monomers (functional monomer is usually added in excess) [39], and overall lower binding affinity.

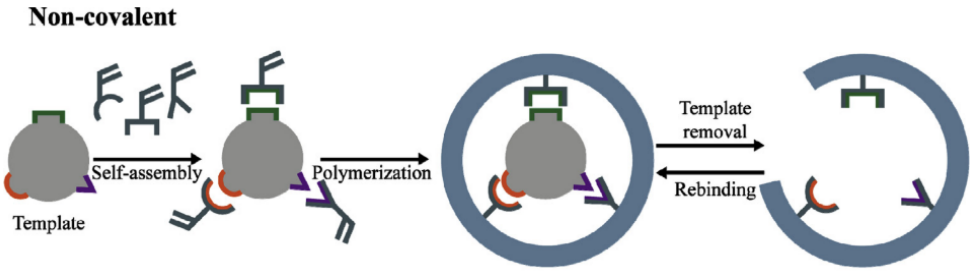

Figure 11: Schematic representation of the non-covalent imprinting strategy in MIP synthesis. Adapted from [36]

2.4 Polymerization Methods and Format

When synthesizing a MIP, the choice of polymerization initiation method directly influences the reaction conditions and, consequently, the properties of the final polymer. Generally, MIPs are produced through thermal, photochemical, electrochemical, or redox-initiated polymerizations (excluding silica-based MIPs synthesized by sol-gel processes) [34].

Among these, **photopolymerization** has become widely popular for its specific advantages: radicals are generated through photoinduced dissociation, meaning the reactions can occur at low temperatures. This aspect is valuable to preserve the interactions in the pre-polymerization complex and to prevent the degradation of sensitive template molecules [40]. This technique also allows precise spatial and temporal control over the polymerization process, being the photopolymerization precisely localizable.

Aside from the trigger, the polymerization method by far more common is **free radical polymerization** (FRP) [41]. FRP is a chain-growth polymerization, whose process unfolds in four main stages: initiation, propagation, chain propagation, and termination, as illustrated in Figure 12. In the initiation stage, free radicals are generated by the decomposition of an initiator. These radicals then react with monomers, initiating the propagation stage, where the free radical reacts with additional monomers, forming new radicals that further propagate the chain. The process concludes during termination when two free radicals combine or one is quenched, thus halting the growth of the polymer chain.

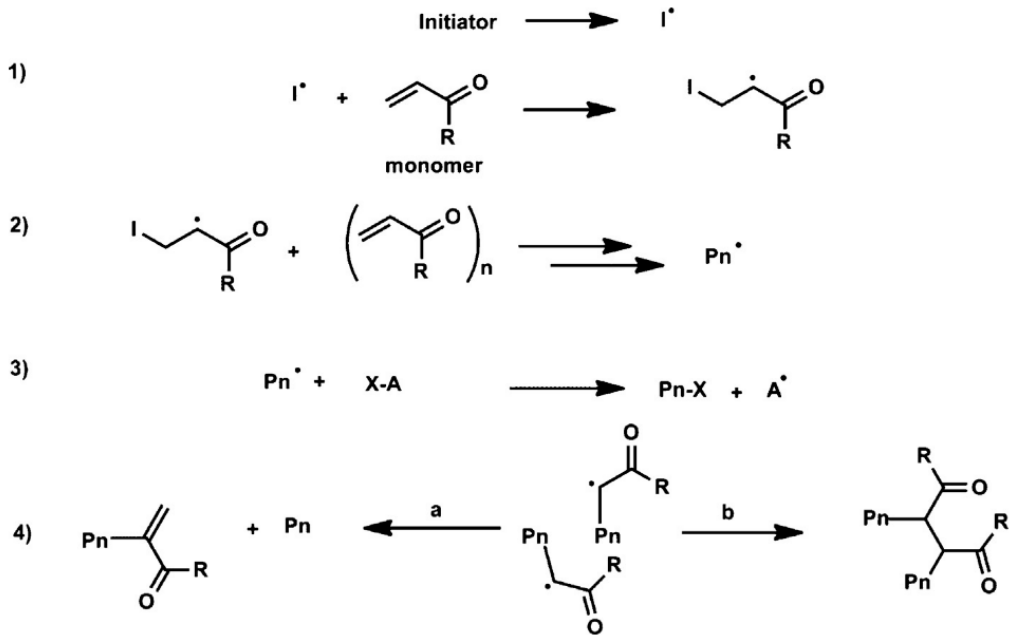

Figure 12: Mechanism of free radical polymerization: 1) initiation, 2) propagation, 3) chain transfer, 4) termination via (a) disproportionation and (b) combination. Picture reproduced from [41].

In MIP synthesis, FRP is valued for its simplicity, versatility, and ability to produce high-molecular-weight polymers quickly. Also, the wide diffusion is due to the large choice of accessible monomers. The main disadvantage of FRP is that it can't provide good control on the polymerization process, due to a fast chain-propagation and irreversible termination [34]. These features usually lead to heterogeneous inner morphology and binding sites distribution [13]. The issue may be addressed by employing Controlled Radical Polymerization (CRP), which allows better control of the reaction kinetics, facilitating the production of nanostructured MIPs and thin films [42].

Several techniques can be employed to fabricate MIPs, each with its advantages and limitations. The choice of the polymerization process depends on the desired characteristics and format of the polymer. Traditionally, the focus has been on producing spherical particles to maximize the surface area, thus providing more accessible binding sites and enhancing interactions with target molecules. These particle-based formats, including micro- and nanoparticles, have found widespread applications, particularly in chromatography and separation processes. Over time, new methods have been developed, and existing techniques have been adapted to the synthesis of MIPs in tailored physical forms [43], as beads, thin films, or deposition on surfaces.

The following sections will explore some of the key polymerization techniques to obtain particle-based and thin-film MIPs.

2.4.1 Polymerization Techniques for Particles

MIPs in the form of particles can be fabricated using a wide variety of methods, leveraging techniques that have been extensively developed in the field of polymer science. A visual representation of the processes discussed below is provided by Figure 13.

- **Bulk Polymerization** is the simplest and most common method used to produce MIPs. In this approach, the template, functional monomer, and crosslinker are polymerized in a large volume, resulting in a highly crosslinked bulk material. The bulk polymer is then ground into particles, which may result in irregular size (between 20 μm and 50 μm [43]) and shape, and heterogeneous binding sites [44]. These are the main reasons why methods with better control on the shape of the particles have been developed. Moreover, it is a method affected by a very low yield: about 30% of the polymer is recovered at the end of the process [45]. Despite these limitations, bulk polymerization remains widely used due to its simple protocol and the low-tech equipment needed.

- **Precipitation Polymerization** occurs in a large volume of solvent, which acts as a precipitation medium. As the polymer grows, it becomes insoluble in the reaction mixture and precipitates. The polymeric beads are then collected by centrifugation [46]. The obtained samples consist of mono-disperse spherical polymer particles, with a size range choice from hundreds of microns to nanometers depending on the chosen parameters [47]. This method avoids the need for post-polymerization grinding, producing more homogenous particles with greater control over size and distribution.

- **Suspension Polymerization** involves suspending the polymerizable phase in a non-solvent medium, usually water, where the polymerization takes place within droplets. This method allows for better control over particle size, producing micron-grade spherical beads with high uniformity [48]. It is often used when the target application requires spherical particles with controlled morphology [49].

- **Emulsion Polymerization** uses surfactants to create stable emulsions of monomers in the aqueous phase [50]. Polymerization occurs within these emulsions, producing fine polymer particles, with nanoscopic sizes typically in the range of 50 to 500 nm.

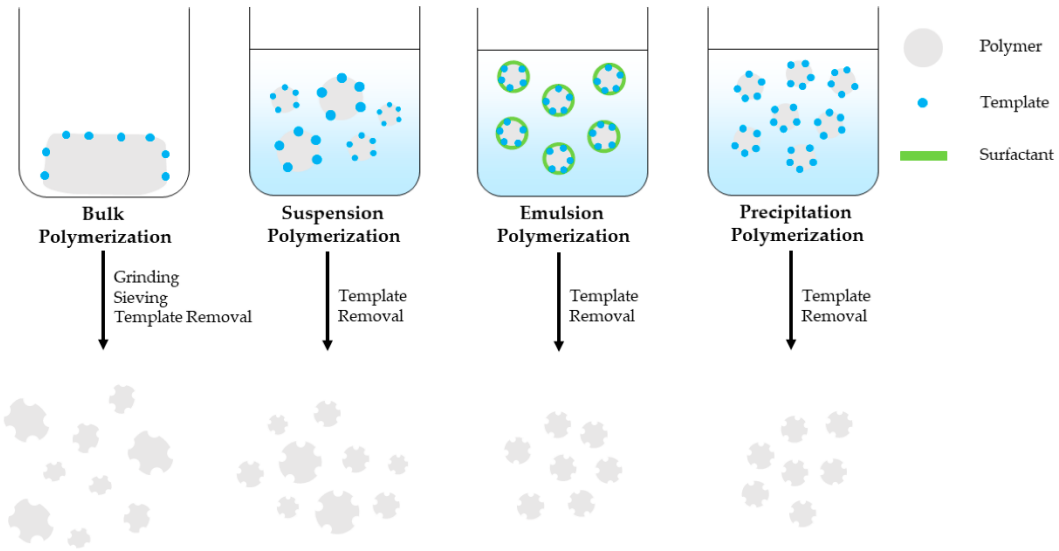

Figure 13: Free radical polymerization techniques used for MIP preparation, reprint from [51]

- **Core-Shell Polymerization** is a technique that creates particles with a core material surrounded by a polymer shell. In the context of MIPs, the shell contains the imprinted sites, while the core provides structural stability [52], as illustrated in Figure 14. Essentially, thin layers of MIP are grafted on the surface of prefabricated particles. The core may be organic or inorganic, typically silica or magnetic particles.

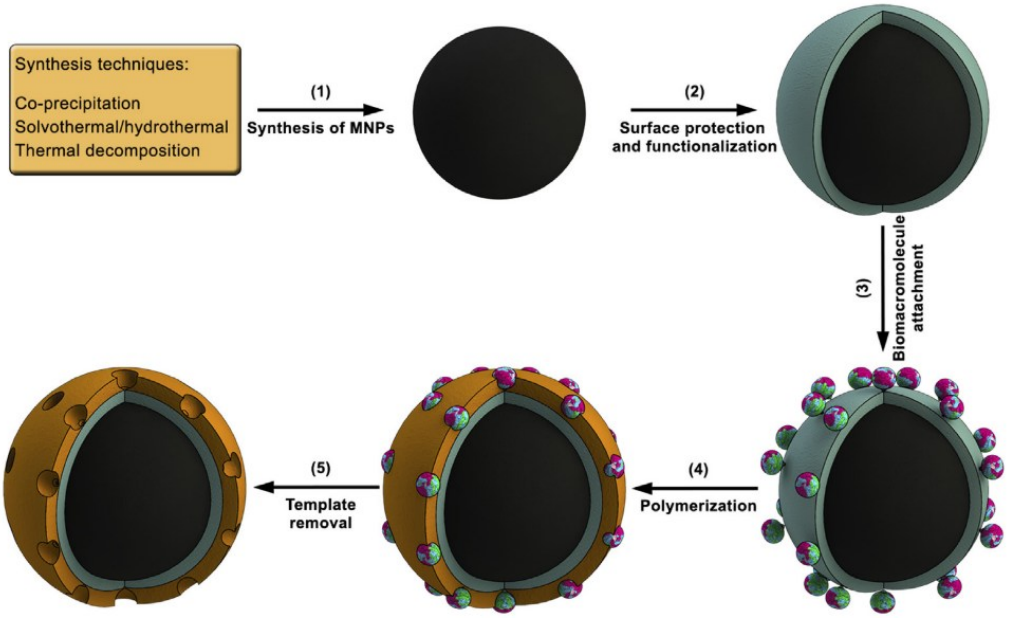

Figure 14: Example of the preparation of core-shell magnetic MIPs for biomacromolecules. Reprint from [36]

2.4.2 Polymerization Methods for Thin Layers

Various polymerization methods have been developed to fabricate MIPs as thin layers, enabling the use of molecular imprinting in surface-based applications.

- **Electropolymerization** is a technique that involves applying an electrical potential to drive the polymerization of functional monomers on an electrode surface (Figure 15). This method is ideal for creating thin, uniform MIP layers, which are highly suitable for sensor applications [53]. Electropolymerized MIPs offer excellent binding site accessibility and can be finely tuned in terms of thickness and morphology. A focus on this technique is in Chapter 5.

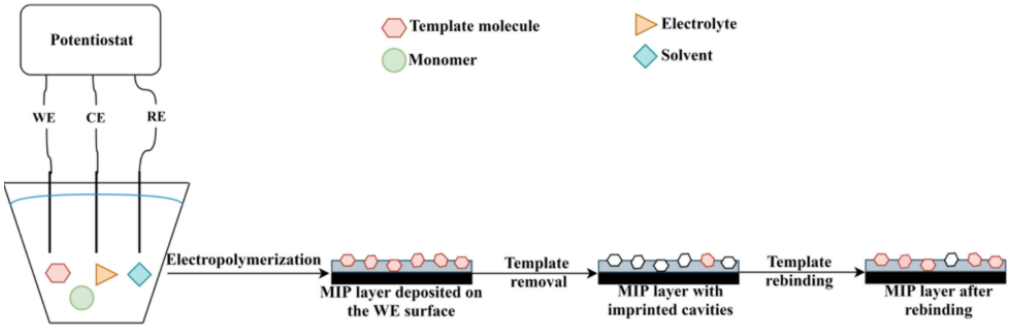

Figure 15: MIP deposition by electropolymerization. Reprint from [54].

- **Surface Imprinting** involves polymerization reactions that take place on the surface of solid-phase matrices. In this process, the recognition sites are primarily located on the outer layer or surface of the substrates [55]**.** The main advantage of this technique is that it avoids the "embedding" of the rebinding sites, which may characterize other imprinting techniques.

2.4.3 The novelty of 3D printed MIPs

The conventional polymerization methods described in the previous sections have formed the foundation for MIP synthesis, providing materials with satisfactory binding affinities and specificities. However, despite many significant benefits, the use of nanoparticles or thin films also implies the limitation of not having self-supporting and arbitrary structures. As MIP technology has evolved, with the purpose of developing more and more advanced fabrication techniques, **Additive Manufacturing** (AM) has emerged as an innovative approach. AM, or **3D printing**, can indeed offer unprecedented control over MIP structure and functional arrangement, aiming to bridge the versatility of 3D printing with the binding properties of MIPs. Through layer-by-layer construction, 3D printing enables the precise design of MIP architectures tailored to specific applications, paving the way for advancements in sensor technology, filtration, and other fields where spatial control and material specificity are essential.

Photon-based lithography and micro-stereolithography have been explored as a micro and nano-fabrication technique to photostructure MIPs. The insightful review of E. Paruli et al. provides a detailed comparison and analysis of the different photon-based lithographic approaches [34]. Complex, high resolution, three-dimensional structures were obtained for the first time by L. P. Chia Gomez et al. [56] who fabricated 3D MIP microsensors by Two-Photon Stereolithography

(TPS). In this study, an MIP formulation compatible with TPS was developed and used to fabricate an all-organic microelectromechanical sensor. This was the first example of how 3D printing can bring a level of versatility and customization not feasible with traditional polymerization methods. However, TPS bears some limitations related to the long printing time and a maximum build size of hundreds of nanometers.

More recently, the employment of **Digital Light Processing** (DLP) to fabricate MIPs was reported for the first time by R. Rezanavaz et al. [19]. DLP printing has been used to create highly structured MIPs for capturing copper(II) ions. Using photopolymerizable formulations with varied ratios of water and methanol, emulsions were formed to yield MIPs with cauliflower-like multiscale structures. Tests confirmed that 3D-printed MIPs absorbed copper up to ten times more efficiently than bulk-prepared versions.

A new report on using DLP to fabricate MIP was recently published by B. Keitel et al. [57]. This study presents a 3D-printable formulation for the emulsion-free fabrication of porous MIPs in highly structured macroscopic geometries, using polymerization-induced phase separation. A porous lattice cube imprinted with 17β-estradiol was fabricated. Notably, incubation tests showed that the 3D-printed MIPs had roughly twice the binding capacity compared to non-imprinted control polymers.

DLP technology seems particularly useful for the development of complex MIPs. First, operating with liquid formulations, DLP allows a wide choice of functional monomers for constituting the polymer network. Then, it allows direct mixing of the target molecule, without undergoing thermal stresses which may lead to its degradation. Finally, it enables high complexity and high resolution (down to features smaller than 100 μm), keeping at the same time a good printing rate and the possibility to fabricate macroscopic objects [58]. Due to its features and advantages, DLP was selected to be investigated in this thesis as a promising fabrication method of complex-structured MIPs.

In the following paragraph, a brief overview of the DLP printer and its operation is provided.

2.4.4 Digital Light Processing

Digital Light Processing (DLP) is a straightforward 3D printing technique that uses a digital light projector to selectively cure photosensitive resin layer by layer. It is a vat polymerization (VP) technique, in which a vat filled with liquid formulation is selectively exposed to the light source, solidifying controlled layers of resin [59]. The object is built layer by layer on the moving printing platform, submerged in the liquid resin.

The printing apparatus and process are shown in Figure 16. A 3D model designed using CAD software is sliced into thin layers, each representing a cross-section of the final object. These layers are sequentially projected onto a photosensitive resin using a **digital micromirror device** (DMD), comprising thousands of tiny mirrors, to reflect the light source and project the pattern of each layer. The resolution is determined by the size of the micromirrors, which establishes the dimensions and number of pixels in the projected image. The light cures the resin in areas that correspond to the projected shape, building the 3D model layer by layer.

The layer thickness is determined by the distance between the printing platform (or the last printed layer) and the bottom of the vat. As each layer cures, the build platform gradually lifts to allow the next layer to form. The cured layer adheres to the previously cured one, creating over time a solid structure. This technology, along with the quick conversion of the resin from liquid to solid achievable through the photopolymerization reaction, makes DLP suitable for the creation of flat vertical surfaces with minimal distortion and excellent shape accuracy [60].

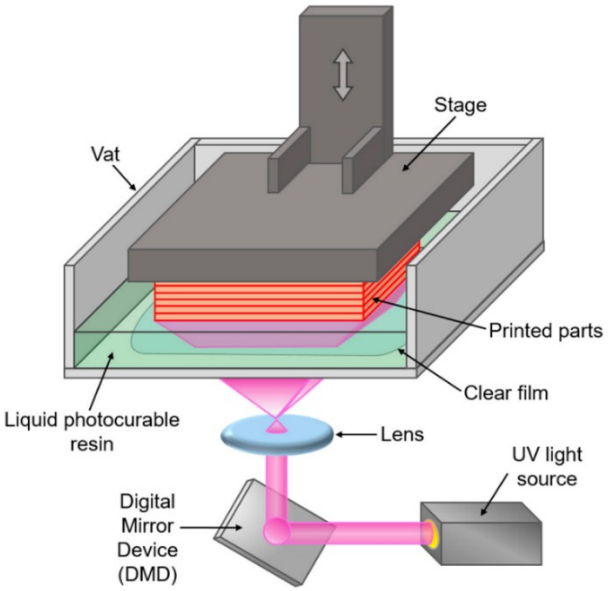

Figure 16: Schematic representation of DLP printer's working principle. Reprint from [61]

2.5 Computational Strategies in MIPs Design: Introduction to Density Functional Theory (DFT)

The significant advancements in software development and increased computing power in recent years have expanded simulation capabilities across numerous fields, including the intricate processes involved in MIP synthesis [24]. **Computational simulations** work as a predicting tool in the design and development of MIPs, offering insights that enhance both the efficiency and selectivity of these materials. By leveraging computational tools, researchers can predict key aspects of the molecular interactions involved in the imprinting process, which allows for the rational design of MIPs with tailored properties for specific target molecules.

Indeed, molecular modelling techniques can be remarkably helpful in producing a rational design of the MIP, identifying optimal functional monomers and appropriate template–monomer ratios [62]. As seen in the previous sections, the degree of affinity between the two components determines the properties of the final polymer [63]. By analysing interactions between template molecules and functional monomers under polymerization conditions, these methods reveal the best candidate monomers capable of complexing with the target template. They also

provide insights into binding energies, stoichiometry, and interaction types (e.g., hydrogen bonding, self-association, π–π stacking, and ionic interactions) [64], addressing the traditional trial-and-error approaches in MIP fabrication, offering more systematic and data-driven methods. The calculated binding energy between template and functional monomers gives a quantitative assessment of the interaction: the most stable monomer-template pair can be determined, based on the most negative (strongest) binding energy [65]. The calculations rely on input data on the chemical structure, including atomic arrangements and charge distribution. The workflow of the study by Karlsson et al. is reported as example in Figure 17.

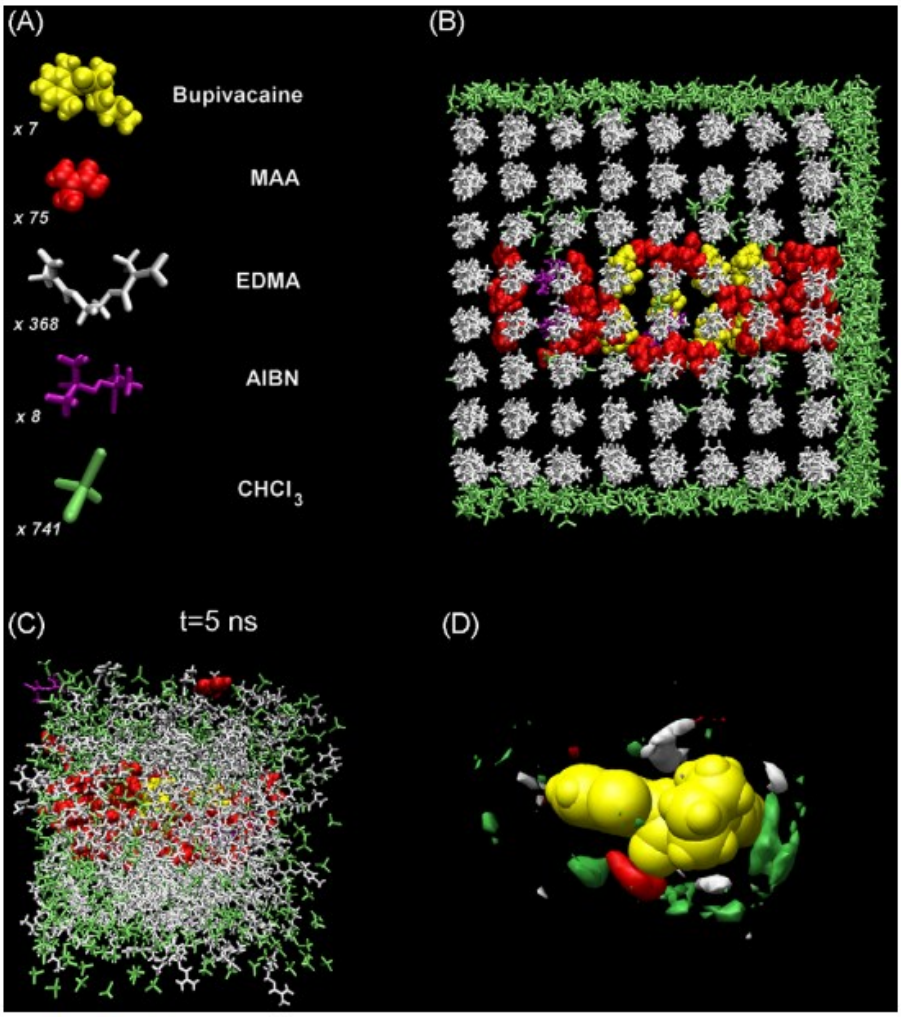

Figure 17: Schematic representation of the steps involved in a typical molecular dynamics simulation. (A) Components included in the model, (B) Model setup, (C) Pre-polymerisation mixture after equilibration (D) Statistical analysis of the various pre-polymerisation complexes formed. Reprint from [66].

The computational design of MIPs may have three main approaches: molecular modelling (quantum mechanics), molecular mechanics, and molecular dynamics.

- The **Molecular modelling** (or **quantum mechanics** (QM)) approach directly describes the electronic structure of molecules, focusing on how electrons interact within atoms and bonds. Quantum mechanical methods are highly accurate but computationally demanding [24].
- **Molecular Mechanics** (MM) approximates molecules as systems of interacting particles, using predefined parameters to model energy without explicitly calculating electron interactions [67]. It's less detailed than the previous approach, but faster and suitable for larger systems.
- **Molecular Dynamics** (MD) is a very powerful tool that uses MM principles but adds the dimension of time by Newton's laws of motion, modelling how a molecular system evolves over time [68].

Many extensive reviews detail the evolution of computational approaches in MIP research, providing a thorough foundation for computational strategies in MIP design [69] [67] [70].

The most popular approach employed for MIP design is a common quantum mechanical method: Density Functional Theory (DFT) [69]. The popularity of DFT lies in its combination of a controlled computational cost and good accuracy [71]. DFT allows for the detailed study of the electronic structure and binding energies between the template molecule and the functional monomers. Through DFT, the optimal monomers that will interact most strongly with the template molecule can be identified.

In QM modelling, usually the following equation (Eq. 1) is used to obtain the **binding energy**, ΔE, that reflects the stability of the interaction between the monomer and template [72]:

$$\Delta E = E_c - (E_T + \sum E_M) \qquad \text{Eq.1}$$

where E_C represents the total energy of the monomer-template complex, E_T is the energy of the template, and E_M is the combined energy of the functional monomers involved. The comparison of ΔE values among different combinations helps in predicting which complex is more stable.

For these calculations, the hybrid functional B3LYP (Becke 3-parameter Lee-Yang-Parr) is frequently applied as it combines the strengths of DFT and Hartree-

Fock (HF) methods [73]. HF methods calculate electronic properties by iteratively solving the Schrödinger equation to reach a consistent result for molecular energy. While accurate, this process is computationally intensive. DFT, on the other hand, simplifies electronic structures by focusing on electron density rather than individual atomic orbitals, treating electron bands as continuous rather than discrete atomic orbitals. This approximation is computationally simpler but introduces limitations, particularly with electron correlation and repulsion effects. Hybrid functionals (like B3LYP) address this by blending DFT's density-based approach with HF's principles, improving accuracy for complex systems [69].

Moreover, when integrated with specific models DFT may include the presence of a solvent in the simulation [67]. This represents a key feature, considering how significant the influence of the solvents is in the pre-polymerization complex interactions. When the Polarizable Continuum Model (PCM) is used to consider the interaction between the complex and the solvent the following equation (Eq. 2) is employed:

$$\Delta E = E_{solvent} - E_{vacuum} \qquad \text{Eq. 2}$$

where the interaction energy between complex and solvent (ΔE) is obtained as the difference between the energy of the complex within the solvent ($E_{Solvent}$) and the one in vacuum (E_{Vacuum}) [72]. PCM simulates the solvent as a continuous medium around the molecular system, providing a more realistic representation of the environment without having to include the individual solvent molecules.

Overall, computational simulations have become a key tool in MIP design, offering predictive understandings that complement experimental work, leading to the creation of more efficient, selective, and application-specific MIPs.

2.6 Applications of MIPs

Molecularly Imprinted Polymers represent a breakthrough in the development of materials capable of selective molecular recognition. The potential lies in the huge versatility of MIPs in terms of the target molecule and fabrication method, and consequently their application. As a result, MIPs have gained importance across an extensive variety of areas.

An aspect that deserves attention is that, despite their advantages, MIPs have seen slow commercial adoption, with a strong discrepancy between the number of

published works and the few patented commercial products [29]. This gap is due to difficulties in producing consistently effective receptors for practical uses. While promising in lab trials, MIPs have yet to demonstrate a clear competitive edge over existing technologies. Challenges such as low receptor homogeneity and unspecific binding [74], or the lack of a universal production and characterization protocol [75] have limited their wider use in industry.

Since the discussion of the application fields of MIP is such a broad and interdisciplinary topic, the first part of this section will provide an overview of the general state of the art in MIP applications, highlighting their role in various industries. Following this general overview, dedicated paragraphs will explore the application of interest of this work, as well as one of the most critical and current: environmental remediation and water treatment.

2.6.1 General overview of application fields of MIPs

Analytical chemistry and separation science were likely the first application fields of MIPs. Since the beginning**,** MIPs have been widely used in chromatographic [76] and solid-phase extraction techniques [77] to isolate and purify specific compounds from complex samples [78]. Their selectivity makes them suitable for all those applications in which the efficient separation and quantification of specific analytes are required, even in complex mixtures such as biological [79] and food samples [80][81].

Nowadays, one of the most common applications of MIPs is in **sensing**, where the molecular recognition properties enable the detection of specific analytes [74]. The inherent versatility of MIPs has enabled their integration into a variety of sensing technologies, leading to the development of diverse MIP-based sensors [82]. Indeed, MIPs have been used as the recognition element in several detection platforms, including electrochemical [83], optical [84], and piezoelectric [85] sensors, usually in the form of thin layers [54]. The compatibility with multiple sensing platforms has driven substantial innovation in MIP-based detection methods and has expanded their application to complex real-world environments. As a result, MIP-based sensors have been studied for the detection of analytes like pollutants [86], pesticides [87] and food toxins [88]. MIPs have been extensively employed in **biosensing** as well, to detect for example drug molecules [89], proteins [20] and microorganisms [90]. So, MIP-based sensors demonstrated significant potential in fields where conventional sensors may be limited in specificity or robustness.

Other than biosensing, the biomedical application of MIPs also comprises the use in **drug delivery systems** to achieve controlled and targeted release of therapeutic agents [91]. MIPs can be designed to release a drug in response to a specific environmental stimulus (e.g., pH or temperature change) or to selectively release drugs at the target site [92]. Their stability, ease of synthesis, and tunable properties make them attractive for developing smart drug delivery systems that reduce side effects and improve therapeutic efficacy.

In **biotechnology**, MIPs are employed as synthetic receptors for biomolecular recognition in various assays [93] and diagnostics [94]. As already highlighted, MIPs' ability to withstand harsh conditions (such as high temperatures or extreme pH) gives them an edge over their biological counterparts, making them suitable for use in industrial processes and laboratory environments.

2.6.2 Application in Environmental Remediation

In **environmental applications**, MIPs may be employed as highly selective adsorbents or as recognition elements in sensor platforms [86]. Their engineered selectivity enables the removal, detection, or quantification of specific molecules within complex environmental matrices, such as water, soil, and air [95]. Primarily, MIPs play a crucial role in pollutant removal, where they demonstrate high efficiency in adsorbing and capturing various environmental contaminants, including polycyclic aromatic hydrocarbons (PAHs) [96], pesticides [87], pharmaceuticals [97] and endocrine-disrupting compounds [98]. This versatility extends MIPs' applicability to a wide range of environmental issues, from trace contaminant detection to industrial waste treatment, wastewater purification, and soil remediation.

In particular, the next paragraph will focus on the employment of MIPs for the removal and recovery of antibiotics from water, being the issue of interest in this thesis.

2.6.3 Water Treatment Approaches: Focus on MIPs for Antibiotic Removal

Antibiotics are fundamental agents in medicine, widely used to treat and prevent infections caused by pathogenic bacteria. Since the discovery of penicillin in the early 20th century, antibiotics have become a primary tool in managing bacterial infections, significantly reducing associated mortality and morbidity. By

targeting bacterial growth and replication, they are effective in both treatment and preventive applications.

Unfortunately, their excessive or inappropriate prescription and their overuse in agriculture and livestock farming are fostering **ecological damage** [99] and **antimicrobial resistance** (AMR), a global health concern. AMR is the ability of microorganisms (like bacteria, viruses, and fungi) to survive and grow despite the presence of drugs meant to kill or inhibit them, such as antibiotics [100]. Indeed, prolonged exposure to these drugs can lead certain pathogens to adapt and develop mechanisms that neutralize or evade the drug's effects, rendering treatments less effective or even ineffective.

The World Health Organization classified AMR as one of the main threats to global health [101], as it can make standard infections harder to treat, leading to longer illnesses, higher medical costs, and an increased risk of death. In particular, antibiotic dispersion in the ecosystem starts primarily through pharmaceutical manufacturing, agricultural runoff, and improper disposal of medications, resulting in the contamination of aquatic environments (Figure 18).

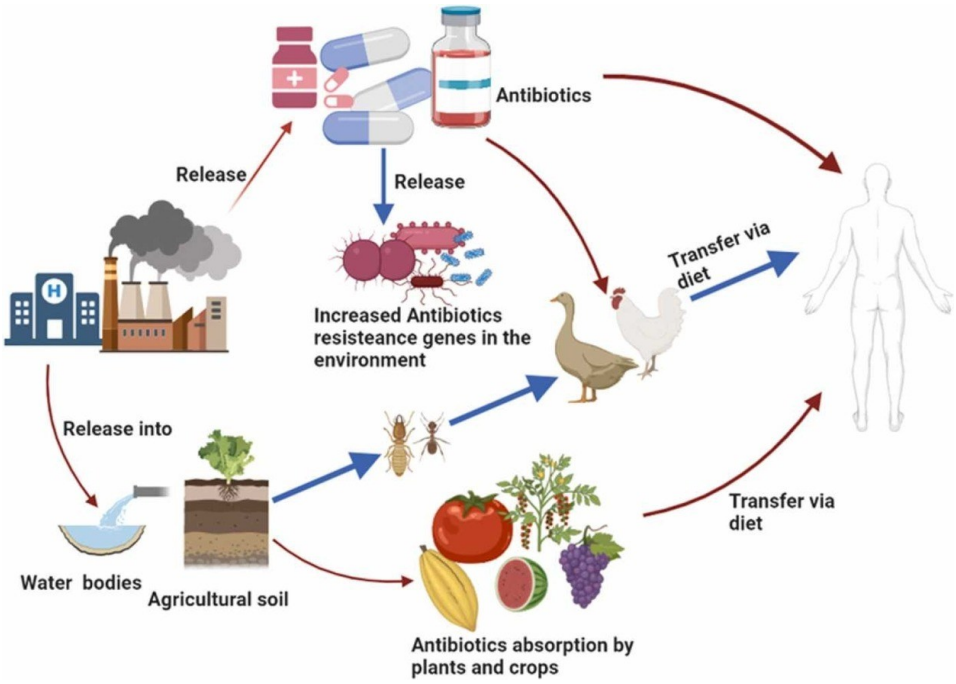

Figure 18: Schematic illustration of the vicious circle of the antibiotic routes toward water environment, soil, food, animals, and human beings. Picture reported from [102].

Traditional water treatment methods, such as filtration, chlorination, and activated carbon adsorption, often struggle to fully remove these micropollutants, particularly at low concentrations. Moreover, they usually lack selectivity against interfering compounds in the analysed medium [103].

In response to these challenges, MIPs have emerged as a promising alternative for the selective removal of antibiotics from water [104]. MIPs offer a tailored approach to address this issue, as their design allows them to recognize and bind specific antibiotic molecules with high affinity. The specificity enables MIPs to selectively remove targeted antibiotics, reducing the extraction of interferents. This aspect is particularly useful when the recovery of the analyte is followed by the analysis of the sample with accurate methods such as chromatography [86]. Moreover, often the MIPs can be regenerated by washing with a suitable solvent, allowing reusability for repeated cycles of adsorption and desorption.

MIPs have been developed for a range of antibiotic classes [105], including tetracyclines [64], sulfonamides [106], fluoroquinolones [107], beta-lactams [108] and so on. Among them, the main interest of this work is focused on tetracyclines. The **tetracyclines** family is a pervasive contaminant of soils and water, a consequence of the abuse of its utilization in modern zootechnics as well as in human curative medicine [99]. Tetracyclines are indeed extensively employed in the livestock industry, and the administration to animals is the first step to a chain of events that causes environmental pollution, and contamination of human food, supporting AMR. To capture and monitor this antibiotic from water-based media, a plethora of MIPs have been developed in the last decades [109][110], including traditional bulk polymers [111], particles [112], membranes [113], electropolymerized layers [114] magnetic particles [115], etc.

Despite their potential, several challenges must be addressed to fully implement MIPs in large-scale water treatment systems. One challenge is the need to enhance the binding kinetics of MIPs to ensure fast and efficient antibiotic removal in continuous water flow systems. Additionally, the scalability of MIP fabrication must be optimized to make the production process cost-effective for large-scale applications.

Future research on MIPs for water treatment aims to develop multi-target systems capable of simultaneously removing various classes of antibiotics and emerging pollutants [105]. Advancing greener synthesis methods is fundamental to align the production of MIPs with principles of sustainability and ecological

responsibility. Furthermore, increasing attention is being directed towards the combination of MIPs with other materials [95], such as nanoparticles or membranes. Finally, the interest is being also focused on exploring new fabrication techniques, such as 3D printing, to obtain greater control over the polymer architecture in the design of MIPs.

Chapter 3

Development of 3D printed MIPs

As already mentioned, the purpose of the thesis is to combine DLP 3D printing and imprinting technology. From an experimental point of view, this means to develop a formulation suitable for light-induced 3D printing with inherent recognition properties for a selected molecule of interest, while ensuring high-resolution outcomes during the printing process.

It's important to remark that the concept of three-dimensionality in this work operates on two distinct but complementary levels. At the **molecular scale**, the MIP material consists of a three-dimensional polymer network. This network incorporates binding cavities specifically tailored to the template molecule, providing molecular recognition. These cavities are formed during the polymerization process and represent the intrinsic molecular-level 3D architecture. At the **macroscopic scale**, the MIP formulations were processed using DLP 3D printing. This technique enabled the fabrication of high-resolution structures with complex geometries. The resulting printed objects maintain the molecular-level features while offering customizable shapes and designs for practical applications, such as filters or sensors.

These two levels of 3D structure are interconnected. The molecular-level architecture ensures the material's functionality, while the macroscopic 3D design

determines its usability in real-world applications. The integration of these scales, schematically depicted in Figure 19, underscores the novelty of this approach, bridging molecular recognition with practical engineering solutions.

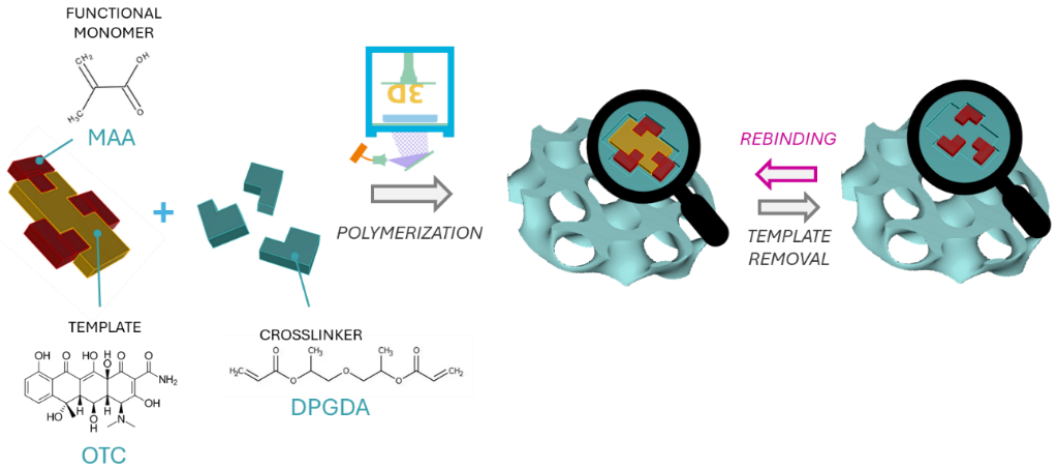

Figure 19: Simplified representation of the 3D printing of a MIP.

The experimental work for this thesis was conducted in two distinct stages. The first stage focused on familiarization with the materials, techniques, and methodologies associated with the printing of MIPs. This initial phase implied an important iterative learning process, that allowed for a foundational understanding of the capability of the material and the potentiality of the work, along with their limitations. The second phase built upon this knowledge, emphasizing the optimization and refinement of the polymer formulations and fabrication procedures, and going deeper with the characterizations. The next sections will delve into all of the aspects of the work.

3.1 First Phase: Initial Exploration and Method Development

This section was written based on the published study: "*E. Camilli, V. Bertana, F. Frascella, M. Cocuzza, S. Luigi, I. Roppolo, Digital light processing 3D printing of molecularly imprinted polymers for antibiotic removal, React. Funct. Polym. 208 (2025)"* [116].

3.1.1 Resin Development

The initial aspect to be investigated was the feasibility of creating a printable resin that included the antibiotic as a filler. This required a systematic study of each component of the MIP formulation.

First of all: the choice of the template molecule. As outlined in the introduction (Section 2.6.3), the primary focus of this study is the removal of antibiotic pollutants from water. In particular, **oxytetracycline** (OTC) was chosen as the template molecule. OTC, an antibiotic belonging to the tetracycline family, is a widespread contaminant of soil and water systems, whose presence in natural aquatic environments necessitates strict monitoring. As evident by its chemical structure (Figure 20), OTC contains multiple functional groups well-suited for non-covalent interactions with functional monomers during the synthesis of MIPs. These groups enhance the formation of specific recognition sites in the polymer matrix, making OTC an effective template for this application.

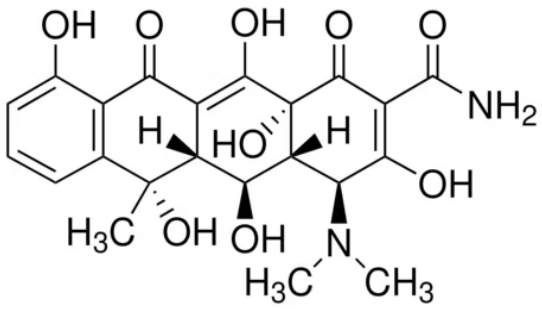

Figure 20: Chemical structure of Oxytetracycline.

The choice of OTC as a template molecule was further justified by its distinctive and readily identifiable absorption peak in the UV spectrum. This feature is particularly advantageous for indirect monitoring of processes like template removal and rebinding. The UV-Vis Spectrum is shown in Figure 21.

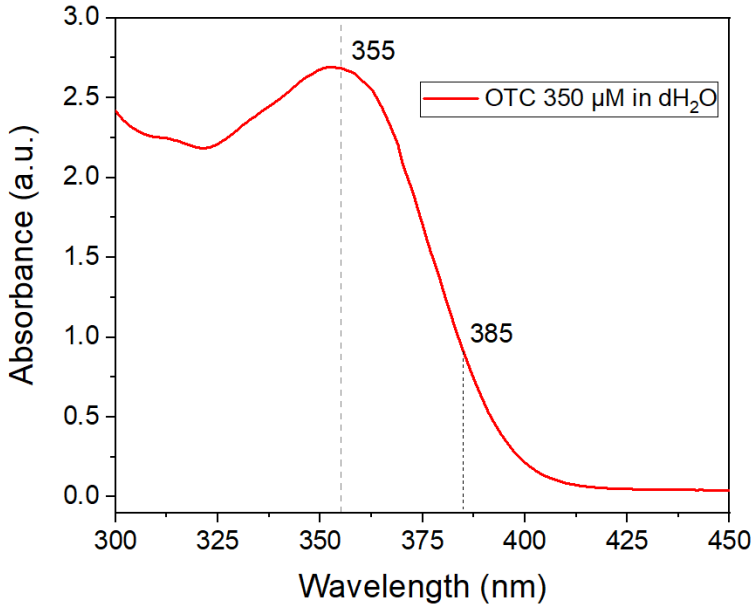

Figure 21: UV-visible absorbance spectra of a solution 350 µM of Oxytetracycline in deionized water. The characteristic peak at 355 nm and the absorbance at the LED light of the printer (385nm) are highlighted.

The next step of the working flow focused on selecting a suitable functional monomer. This decision was guided by a detailed review of prior studies on MIPs for tetracyclines [110][117][113][112]. Of particular relevance was the work of W. Cai and R.B. Gupta [111], which demonstrated the successful use of MIPs as selective adsorbents for tetracycline, with **methacrylic acid** (MAA) as the functional monomer, and ethylene glycol dimethacrylate (EGDMA) as the crosslinker. Their findings highlight that the carboxyl group in methacrylic acid can form hydrogen bonds with the hydroxyl and amide groups present in tetracycline molecules. Following this rationale, MAA was preferred as the functional monomer over other possibilities, due to its demonstrated compatibility and frequent application in MIP, specifically for its prominent use in studies with tetracyclines as the template.

In the literature, the molar ratios employed for MIP formulation vary significantly even with the same template and functional monomers, reflecting diverse approaches to optimizing MIP's fabrication. In this work, the chosen molar ratio was inspired by the recommendations from reference studies [23], along with the consideration that OTC has a limited number of functional groups available for interactions. Thus, the template-to-functional-monomer ratio of 1:4 was adopted. A schematic representation of a possible interaction between one OTC molecule and

four MAA molecules is shown in Figure 22, resembling the method reported in the reference work [111].

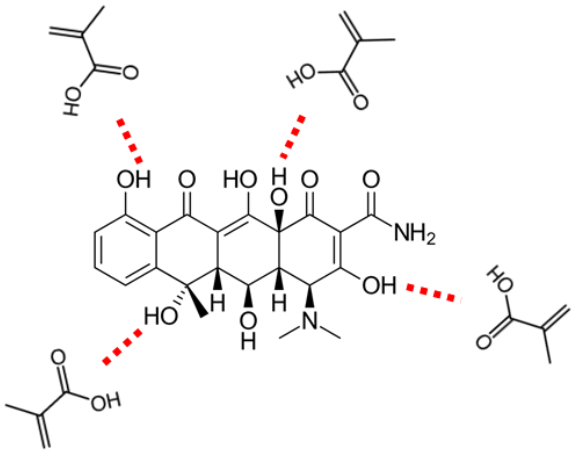

Figure 22: Schematic depiction of a possible pre-polymerization complex between OTC and MAA.

The solubility of the template in the chosen functional monomer plays a key role in ensuring effective interactions and uniform distribution during the pre-polymerization stage. A transparent and homogeneous solution implies the correct dissolution of the OTC, which is in the form of a fine powder. Attempts to dissolve it directly in the functional monomer were unsuccessful, as the resulting solution appeared opaque. To address this, a series of easily removable solvents with low boiling points, including ethanol, acetone, and acetonitrile, were tested, aiming for their subsequent removal after dissolving OTC. However, these solvents proved unsuitable to effectively solubilize the antibiotic.

Therefore, the choice fell on **dimethyl sulfoxide** (DMSO), in which the OTC solubilizes more easily. DMSO is a solvent with moderate polarity compared to water [29], meaning it can dissolve a wide range of organic compounds while allowing non-covalent interactions to remain intact. Specifically, DMSO does not excessively disrupt the polar interactions between OTC and MAA, particularly the hydrogen bonds between the hydroxyl or amide groups of OTC and the carboxyl group of MAA [111], while still providing enough solvating power to dissolve OTC effectively. However, the challenge with DMSO lies in its relatively high boiling point, making it harder to remove from the final formulation. For this reason, the minimum volume necessary to dissolve the OTC was determined and used, minimizing the amount of solvent in the final formulation. Specifically, the selected amount was 15%phr.

The next step was the choice of the crosslinker. Various monomers were taken into consideration, evaluating primarily the length of the chain (molecular weight) and the number of functionalities (acrylate groups). The selected crosslinker must be appropriate both for the DLP printer and for the interaction with the functional monomer so that it generates an accessible yet stable polymeric matrix.

Among many, **dipropylene glycol diacrylate** (DPGDA), a di-functional acrylate, was selected (Figure 23). This monomer was chosen over more conventional crosslinkers (such as EGDMA) due to the better performance in 3D printing. In fact, unlike more rigid crosslinkers, like EGDMA itself, DPGDA didn't show cracking due to shrinkage stresses after 3D printing, keeping a good balance between the ability to form the cavity structures and the maintenance of sufficient flexibility and swellability, to allow the permeation of the solvent during the washing and rebinding steps.

The crosslinker must be present in excess relative to both the template and the functional monomer, usually around 80mol% [23]. The molar ratio of template to functional monomer to crosslinker was set at 1:4:20.

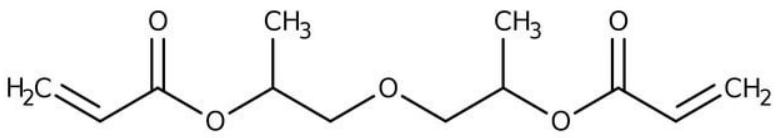

Figure 23: Chemical structure of Dipropylene glycol diacrylate (DPGDA)

As the photoinitiator, **Phenylbis(2,4,6-trimethylbenzoyl)phosphine** oxide (BAPO) was used (Figure 24). BAPO is a type I photoinitiator, meaning it undergoes homolytic cleavage upon UV irradiation to generate reactive free radicals. These radicals initiate polymerization by attacking the double bonds in monomers such as acrylates or methacrylates. Type I photoinitiators are considered the best option in MIP's synthesis [34]. In particular, BAPO was selected because its broad absorption spectrum, covering both UV-A (320–400 nm) and part of the visible light spectrum (400–500 nm), makes it suitable for the irradiation wavelength of the employed 3D printer (385 nm).

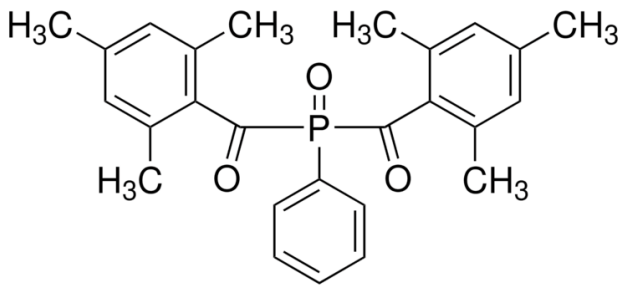

Figure 24: Chemical structure of Phenylbis(2,4,6-trimethylbenzoyl)phosphine oxide (BAPO) .

Other than the interaction between the template and the functional monomer, it's important to address the reaction between the functional monomer and the crosslinker. Upon UV exposure, the photoinitiator activates, initiating the polymerization that involves both the methacrylate group of MAA and the two acrylate groups of DPGDA. This process results in a highly crosslinked network due to the bifunctionality of DPGDA, with MAA becoming integrated into the polymer on one side and interacting with OTC on the other. A simplified representation of this process is shown in Figure 25.

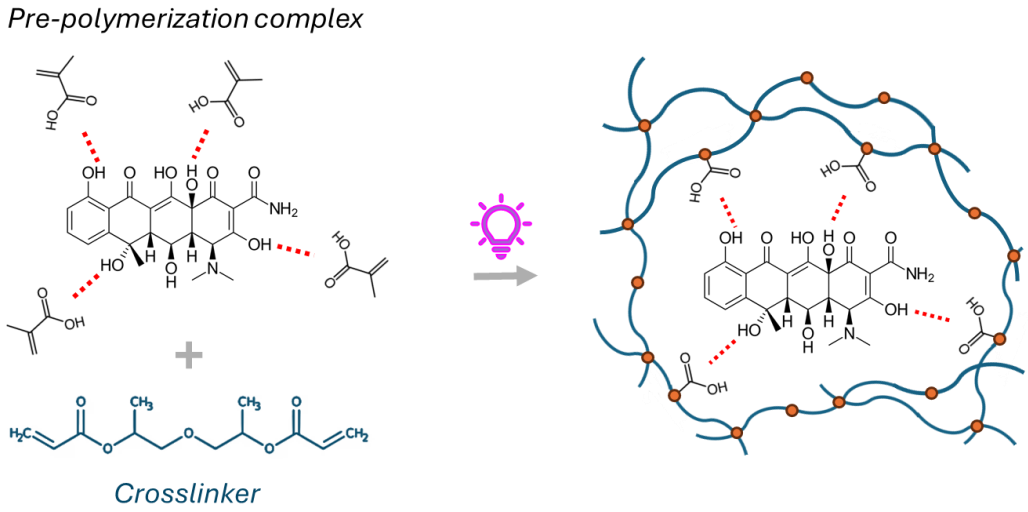

Figure 25: Schematic representation of the molecular imprint of oxytetracycline in methacrylic acid and dipropylene glycol diacrylate.

In summary, the optimized MIP formulation comprised: oxytetracycline as the template, methacrylic acid as the functional monomer, dipropylene glycol diacrylate as the crosslinker, BAPO as the initiator, and dimethyl sulfoxide as the solvent (Figure 26).

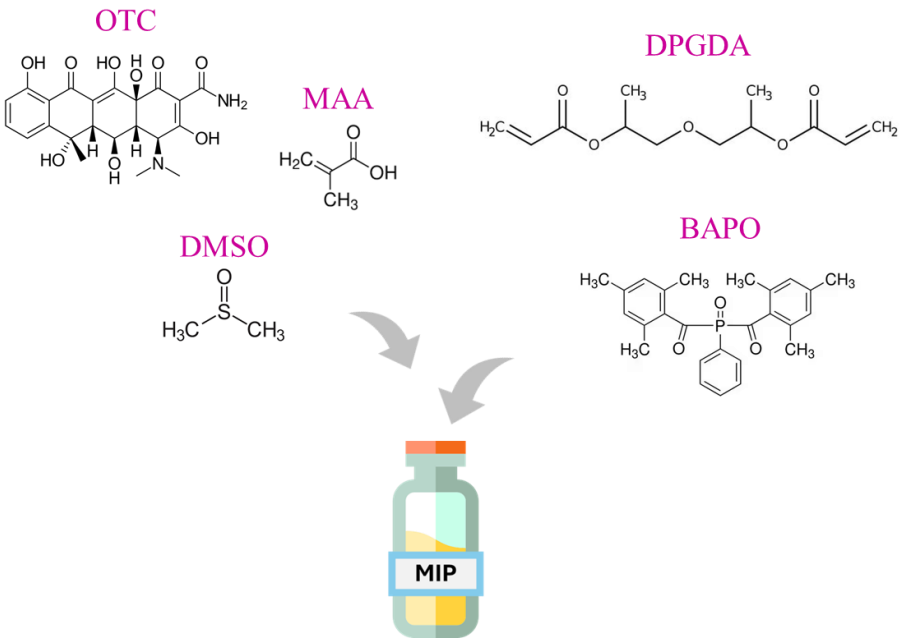

Figure 26: The components of the MIP's photocurable resin.

The same procedure was employed for the preparation of the so-called **Non-Imprinted Polymers (NIPs)**, with the difference of excluding the template. NIPs serve as controls to differentiate the effectiveness of molecular imprinting from the nonspecific affinity of the monomers for the template. Their inclusion is essential, as MIPs inevitably exhibit some degree of nonspecific interactions. Details of the preparation of the formulations are reported in Chapter 4.

3.1.2 Characterization Of The Formulations

Once the formulation was prepared, preliminary characterizations were conducted. Firstly, the viscosities of both MIP and NIP formulations were determined by **rheological** measurements, to investigate any potential impact of the antibiotic. The results revealed a comparable behaviour between the two resins, as shown in Figure 27(a). The viscosity values are suitable for DLP processing [118].

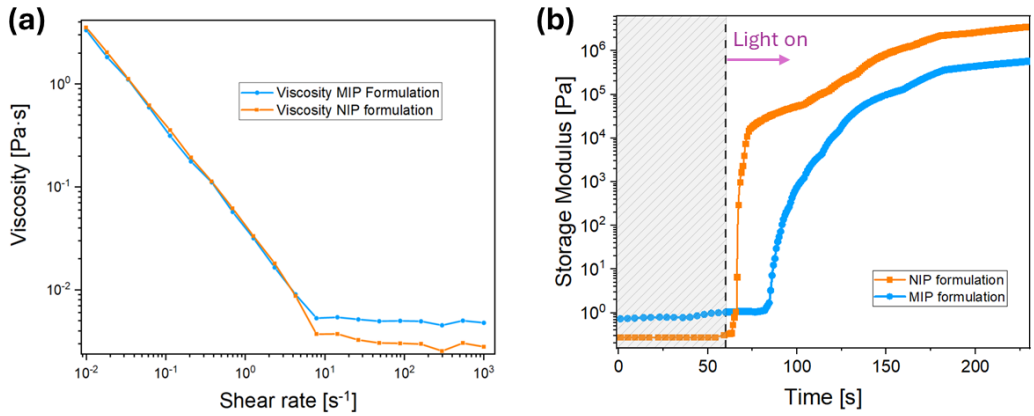

Figure 27: (a) Viscosity of MIP and NIP formulations under continuous shear rate sweep. (b) Real-time photorheological measure of the MIP and NIP formulations.

Secondly, real-time **photorheology** was employed to evaluate the effect on the polymerization kinetic of the OTC, in the MIP resin. As shown in Figure 27(b), the presence of the target molecule strongly interferes with the photopolymerization. It can be noted that the start of the polymerization is delayed: while the NIP formulation reacts almost immediately, the MIP formulation shows a delay time of about 20 seconds. Moreover, during the first 10 seconds of polymerization, the slope of the MIP curve is 99% less steep compared to that of the NIP curve, indicating that the MIP formulation has much slower reaction kinetics. The slower polymerization kinetics can be ascribed to the absorbance of the OTC within the range of irradiation of the employed 3D printer (385 nm), as shown in the UV-Vis spectrum in Figure 21. The antibiotic essentially behaves as a dye [119], competing with the photoinitiator in the absorbance of the light.

The photorheology also shows that the value of storage modulus G' plateau is lower in the formulation with the target molecule, reflecting a less rigid polymer network. This can be related to a hindering effect of the OTC on the crosslinking density, but also to a decrease of secondary forces in the network, with MMA's carboxylic group bonded to OTC instead of establishing bonds with ester moieties of the DPGDA.

To evaluate the stability of OTC following photopolymerization, the UV-Vis absorbance spectra of both the formulation and a thin printed layer were examined to determine whether spectral features associated with the presence of the antibiotic remained after printing. As shown in Figure 28, a difference in the spectra between the MIP and NIP is clearly visible. Given that the only difference between these two formulations is the presence of OTC, it can be reasonably assumed that this

spectral variation arises from the antibiotic's presence in the MIP formulation and printed sample. Furthermore, the fact that this spectral component persists in the printed sample, rather than being observed only in the formulation, suggests that OTC is retained in the polymerized material. While this may indicate a degree of stability following the photopolymerization process, a definitive assessment of OTC's chemical integrity remains challenging.

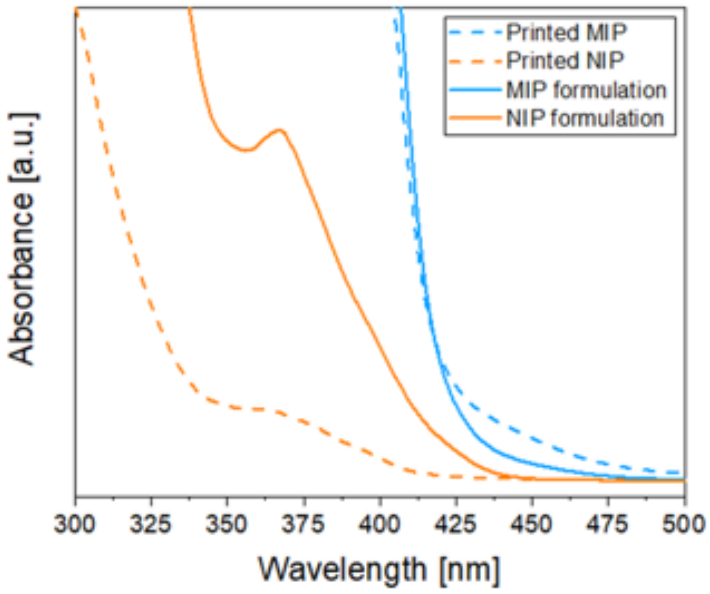

Figure 28: UV-visible spectra of MIP and NIP, both liquid formulations and thin printed samples. The graphs show the presence of a yellow component in the MIP spectra due to the presence of the OTC, which is absent in the NIP ones.

3.1.3 Printing Process

Photorheology gives an indication on the polymerization kinetics of the formulations, nevertheless, the optimum printing parameters must be found experimentally with the actual equipment, through a trial-and-error procedure, which is usually quite time-consuming.

The first design that was printed, was a multi-material disk consisting of two levels: a base made of DPGDA, 500 µm thick, with on top a 50 µm thick layer of MIP/NIP resin (Figure 29). The diameter of the disks was 10 mm, so that the sample could fit in a 48-well plate. The thickness of the MIP/NIP layer was minimized to have a thin active coating on a surface, mimicking a functionalization film.

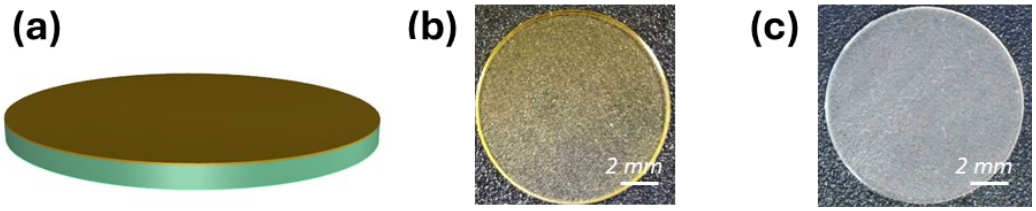

Figure 29: (a) Graphic representation of the multi-material disk: the base (in aquamarine) is 500 µm thick, while the MIP/NIP layer (in dark yellow) is 50 µm thick. Pictures of the printed MIP (b), and NIP (c).

Through iterative experiments, the optimal printing parameters in terms of time of light exposure, light intensity, and layer thickness, were found (Section 4.4). Consistent with the photorheological characterization, the MIP resin needed a longer time and a higher power to polymerize, compared to the NIP resin.

Once the printability of the formulation was tested with simple geometries as the disks, more complex objects were fabricated. In the context of this work, the most captivating aspect of 3D printing is the possibility of creating elaborate designs. To showcase this versatility, within the scope of developing MIPs for antibiotic recovery from water, a filter-shaped, micro-structured MIP has been 3D printed as proof of concept. The CAD of the filters is shown in Figure 30(a).

The printing of such complex geometry made evident how the presence of the OTC allowed to achieve a much better confinement of the polymerization process in the *xy* plane and lower light penetration on the *z-axis*. So, despite the relatively long printing time, it was possible to print high-resolution objects with the MIP formulation, with the finest feature achieved of 200 µm on the xy plane. The resulting filter is shown in Figure 30(b).

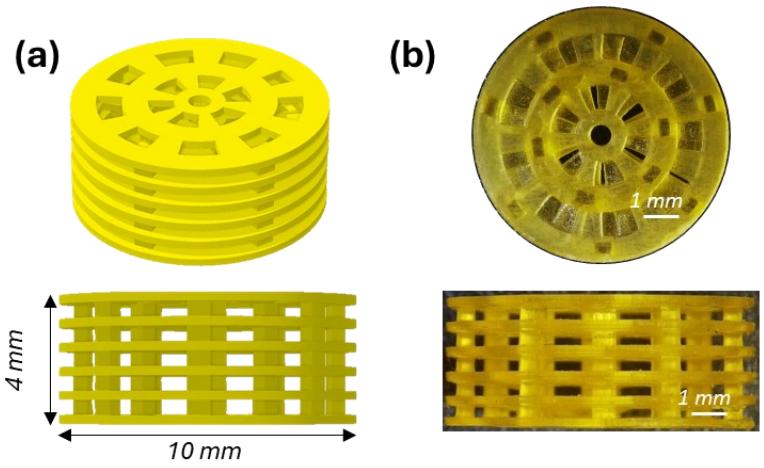

Figure 30: (a) CAD of the filter. (b) Picture of the printed MIP filter.

On the other hand, the corresponding NIP filters were not printed in this phase, due to the difficulty of printing with similar resolution the filter with the formulation without the antibiotic, confirming the essential role of the OTC in the printing process. The details of the printing process and the treatment of the samples are reported in Chapter 4 (Section 4.4).

Assessed the printability of the formulation, the next step was to prepare the sample for the molecular imprinting. This involved, first of all, washing the samples to free the cavities.

3.1.4 Template Extraction

Template removal is a fundamental yet challenging step in the preparation of MIPs. As reported in the literature, this process is often described as time-consuming and complex, even for systems involving microscopic particles or thin polymer layers. For bulky samples, such as those described in this work, the extraction process becomes even more demanding due to the increased diffusion path lengths and material density.

In this study, template removal was carried out using Ultrasound-Assisted Extraction (UAE) [27]. The samples were immersed in a methanol and acetic acid solution (9:1 v/v), and the washing process was conducted in cycles lasting several hours. Alternating the use of a tilting platform and an ultrasound bath ensured thorough extraction while minimizing potential damage to the samples. The intensity of the ultrasound bath was kept as low as possible to preserve the structural

integrity of the MIPs. The duration of the extraction process varied depending on the sample volume. For instance, the multi-material disk, which included a thin MIP layer, required only a few hours for complete template removal. Conversely, the all-MIP filters, significantly larger in volume, required several days to achieve the same result. To ensure comparability, NIP samples underwent the same washing protocol as the MIPs, despite not containing a template molecule, to have a reliable control.

During the washing process, the washing solution was iteratively replaced, and its UV-vis spectra were analysed to monitor the progress of template removal. The washing procedure was deemed complete when the spectra no longer displayed the characteristic OTC peak at 355 nm, and the spectrum of the washing solution of the sample is overlapped with clean methanol/acetic acid. An example is displayed in Figure 31.

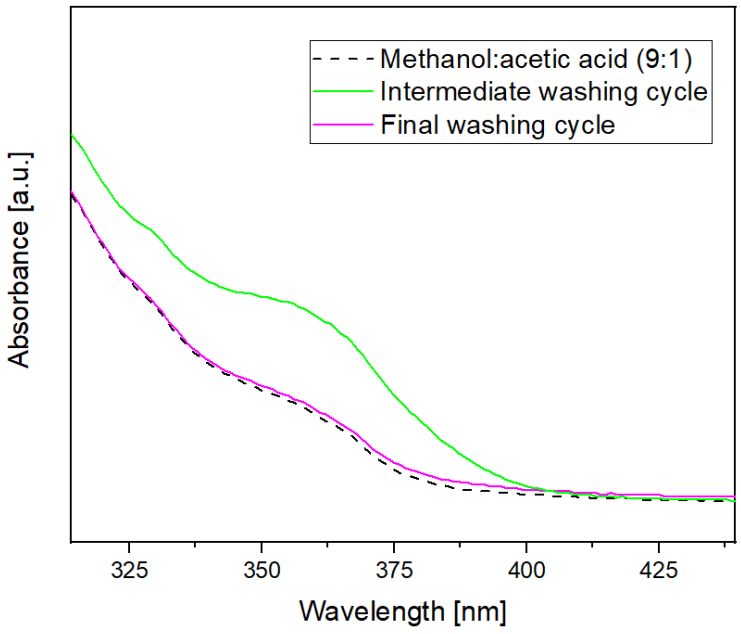

Figure 31: Representative spectra from an intermediate and final washing cycle, along with the reference clean methanol/acetic acid solution.

A notable visual indicator of the washing progress was the colour change in both the samples and the washing solution. Initially, the samples appeared yellow due to the presence of OTC, gradually becoming more transparent as the antibiotic was extracted. In contrast, the washing solutions transitioned from clear to pale yellow as they extracted the OTC. Figure 32 displays a filter after the rebinding phase, highlighting the visible differences before and after washing. Notably, the

samples showed an excellent structural resistance, preserving the integrity of the polymeric matrix after undergoing the washing procedure and the removal of the template.

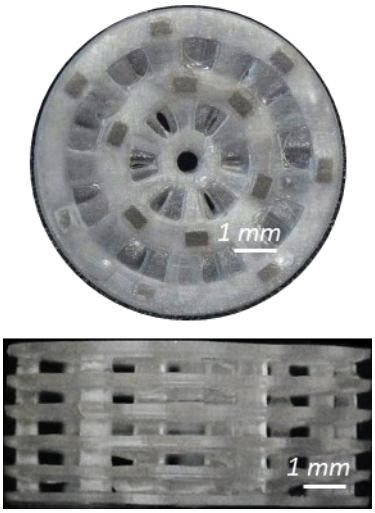

Figure 32: Picture of the MIP filter after the washing procedure.

3.1.5 Characterization Of The Samples

The accuracy of the printed MIP-objects with respect to the CAD was measured by a **3D scanner** (Figure 33). The results showed an excellent fidelity to the design, with discrepancies within ±50 µm. Larger deviations are related to the impossibility of the tool to scan internal cavities.

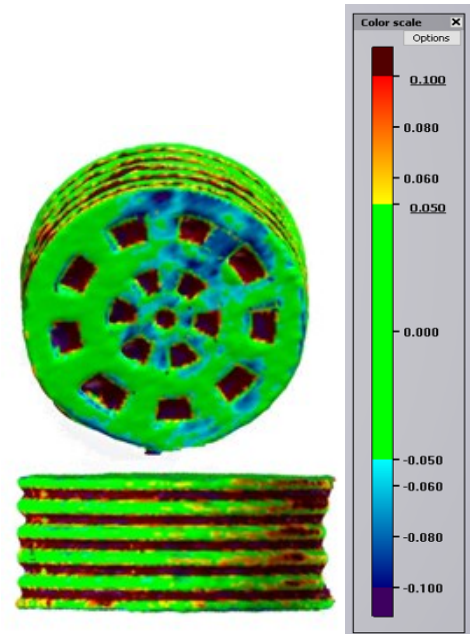

Figure 33: 3D scan of the printed filter.

Fourier-transform infrared (FT-IR) spectroscopy in attenuated total reflectance (ATR) mode was conducted both before and after resin polymerization (Figure 35) to assess the conversion of the C=C double bonds to C-C single bonds, thereby evaluating the efficiency of monomer-to-polymer transformation of the DPGDA, and the anchoring of MAA in the polymer matrix. Specifically, FT-IR ATR spectroscopy was done.

To calculate the acrylate conversion (%) for MIP and NIP formulations, the area subtended by the peaks corresponding to the C=C double bonds (A_{1630}) is normalized by the area subtended by a peak that is not involved in the polymerization process, namely A_{1730}, corresponding to the C=O bonds. The complete spectra, with the highlighted peak, are shown in Figure 34.

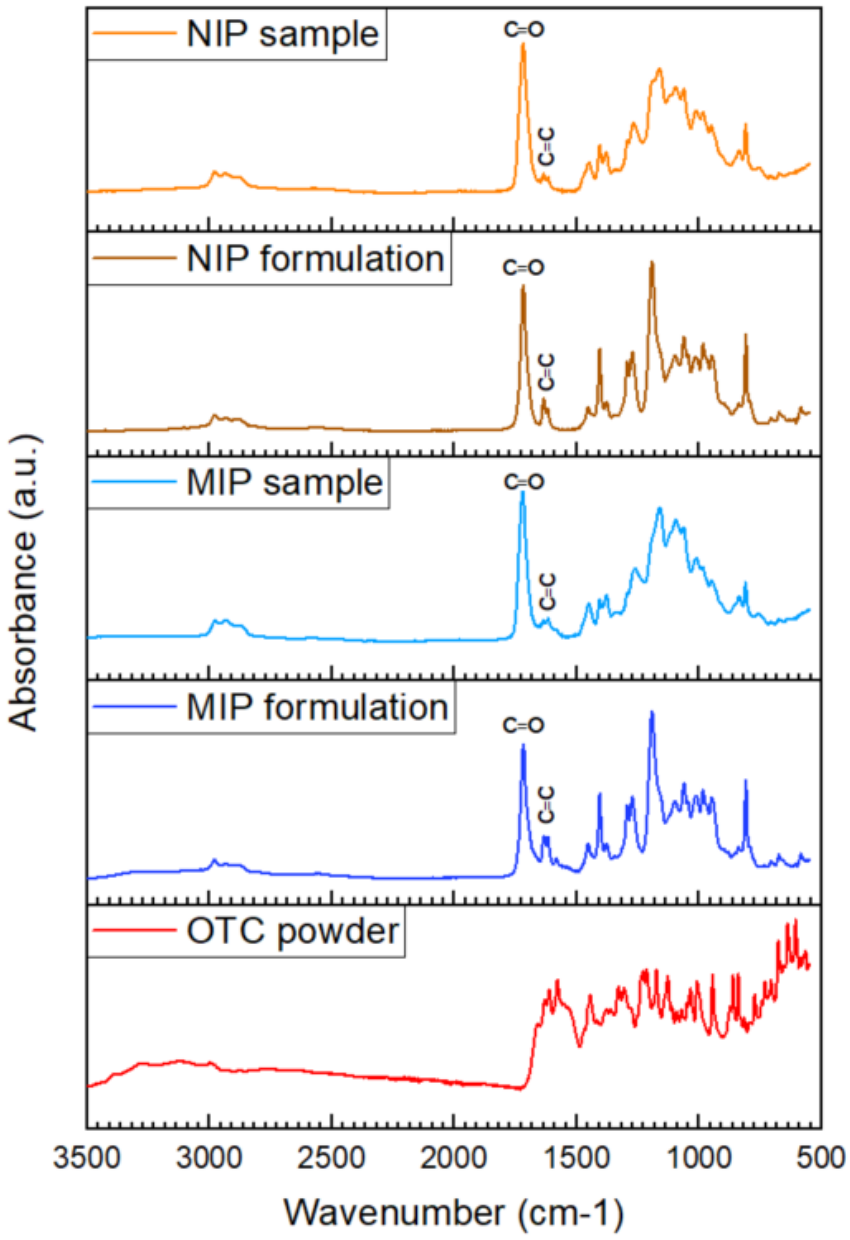

Figure 34: ATR FT-IR spectra of liquid formulations, printed sample, and Oxytetracycline powder.

The values of the areas are reported in Table 1. The acrylate conversion is calculated as shown in the following formula:

$$Acrylate\ conversion\ \% = (1 - \frac{A_{1630}(crosslinked)/A_{1730}(crosslinked)}{A_{1630}(formulation)/A_{1730}(formulation)}) \times 100$$

Table 1: Acrylate conversion (%) for MIP and NIP formulations after 3D printing

		Liquid Formulation	Printed Sample	Acrylate conversion [%]
MIP	A_{1730}	10,80	15,38	70,5
	A_{1630}	1,78	0,75	
NIP	A_{1730}	12,54	16,69	69,4
	A_{1630}	1,59	0,65	

Both MIP and NIP formulations achieved around 70% of acrylate bond transformation. Although not especially high, this degree of conversion is deemed suitable for 3D printing applications [120].

Additionally, the spectra of the MIP/NIP formulations and printed samples were compared to the spectrum of the Oxytetracycline powder. As depicted in Figure 35, a distinct peak at 1580 cm^{-1} in the OTC spectrum is present in the MIP formulation and, even if weaker, is recognizable in the spectra of the printed polymer. Meanwhile, this peak is absent in NIP. This observation confirms the presence of the antibiotic on the surface of the 3D-printed MIP.

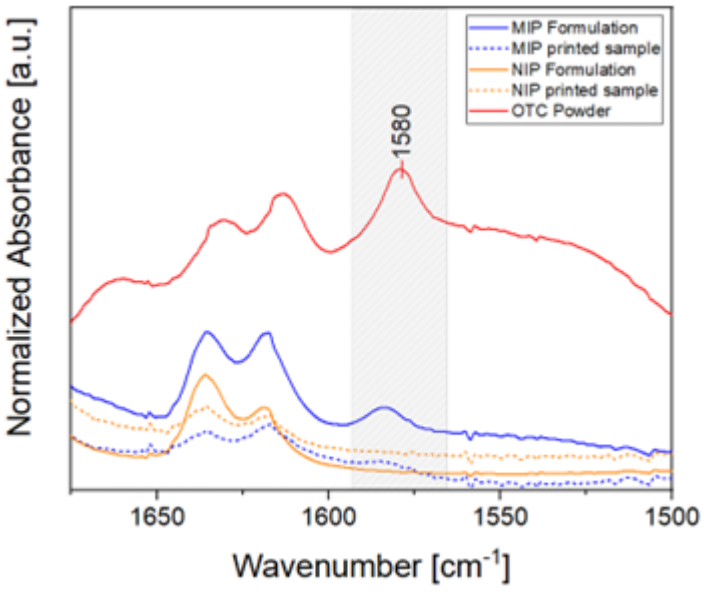

Figure 35: FT-IR spectra of both liquid formulations and printed samples, and the pure antibiotic in powder.

The following step was to assess the binding capability of the novel material.

3.1.6 Rebinding: Results And Discussion

To evaluate the rebinding efficiency, the samples were immersed in a solution containing the target molecule, namely the OTC. After a predetermined period (dependent on the experiment), the samples were removed from the solutions, and the UV-vis spectra of the solutions were analysed before and after contact with the samples. The comparison of these spectra allowed for the quantification of the template molecule removed from the solution, providing insight into the binding capacity of the samples. A detailed explanation of the procedure is reported in Section 4.5.

Several parameters can be calculated to characterize the binding performances of MIP [23][117]. In this work, the extent of the interaction between the polymer and the target molecule was described in terms of the percentage of OTC removed from the rebinding solution. The **Removal percentage** is calculated using the formula:

$$\%Removal = \frac{C_s - C_f}{C_s} \times 100$$

Where C_s is the initial concentration of OTC in the solution, and C_f is the amount of free OTC in the solution after the incubation with the polymer.

When possible, the **Imprinting Factor** (IF) was calculated as the ratio between the removal percentage of imprinted and non-imprinted polymer:

$$IF = \frac{\%Removal_{MIP}}{\%Removal_{NIP}}$$

The IF reflects the effectiveness of the imprinting process, meaning how much the inherent affinity of the polymer to the template increases due to the presence of the imprinted cavities. Another useful figure of merit is the **Binding Capacity** (BC), namely the amount of bound OTC divided by the weight of the MIP.

The first samples to be tested were the disks. As described in reference studies [111][112], the sample underwent rebinding using different concentrations of the binding solution (C_s), specifically 50 μм, 75 μм, 100 μм and 150 μм of OTC in deionized water, to compare the binding ability in the presence of a different amount of target. Water was chosen as solvent given the intended application in water purification.

The percent of removed target and the Imprinting Factor (IF) obtained from the experiments are detailed in Table 2. Comparison between MIP and NIP performances with different concentrations of the rebinding solutions. Under identical experimental conditions, the most effective binding performances were observed at the highest target concentration, as displayed in Figure 36. Specifically, the removal percentage reaches the highest value in the case of 150 μM solution, with nearly 14% of the target bound to the MIPs from the initial solution. This result is almost twice that of the 75 μM solution and 54% and 70% higher than the 50 μM and 100 μM respectively. This behaviour may suggest that the differences in binding performance between the MIP and NIP may not be as pronounced due to the limited number of interactions at low concentrations. This indicates that higher concentrations could magnify these differences, allowing the rebinding with the MIP to become more evident.

Table 2. Comparison between MIP and NIP performances with different concentrations of the rebinding solutions.

C_s (μM)	*Sample*	*%Removal*	*IF*
50	MIP	9.00±2.0	1.2
	NIP	7.46±0.4	
75	MIP	7.46±1.6	0.8
	NIP	9.07±2.9	
100	MIP	8.15±0.9	0.8
	NIP	9.4±1.7	
150	MIP	13.9±3.3	1.6
	NIP	8.6±3.6	

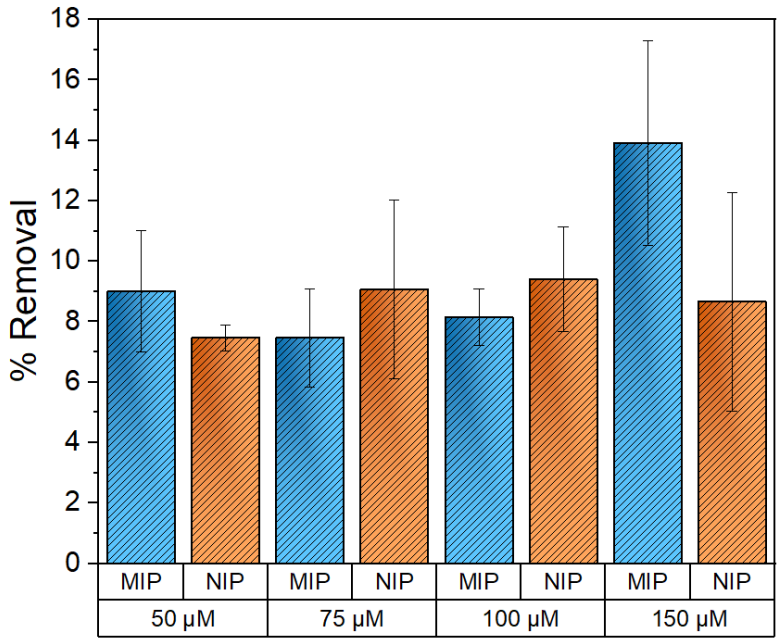

Figure 36: %Removal of MIP and NIP disks, with solutions at different concentrations of the target molecule. Data are means of triplicate measurements.

In all cases, a portion of non-specific binding occurs, evident from the non-negligible binding of NIPs. It should be noted that in molecular imprinting techniques the non-specific binding is often inevitable and generally arises from the inherent affinity of the target to the functional monomer, that provides functionalities independently from the presence of imprinted cavities [64].

Notably, for the 50 μM, 75 μM, and 100 μM solutions, the behaviour of both the imprinted and non-imprinted samples exhibited substantial similarity (Figure 36). However, with an increase in target concentration, the disparity between the two became more pronounced, as indicated by the Imprinting Factor (IF) reaching its peak with the 150 μM solution (Table 2). This behaviour may suggest that the differences in binding performance between the MIP and NIP may not be as pronounced due to the limited number of interactions at low concentrations. This indicates that higher concentrations could magnify these differences, allowing the rebinding with the MIP to become more evident.

Moreover, it is noticed that at the higher concentration the binding values for the NIP are comparable to the binding observed for both MIP and NIP at lower concentrations. This suggests that the non-specific binding component remains relatively constant across all conditions, while the contribution of specific binding

increases with target concentration, enhancing the differentiation between MIP and NIP.

The structural composition of the multi-material disks may be a factor of the aforementioned outcomes: part of the nonspecific interaction can be attributed to the presence of the "base" layer of the disk. This underlying layer lacks molecular imprinting specificity and contributes to the observed background binding. Indeed, the structural differentiation between the MIP and NIP disks is confined to the 50 μm thick "active" layer, where the imprinted sites are located. These considerations suggest the elimination of such non-functional components in the next designs, to increase the binding site differentiation and the specific rebinding capacity of MIP systems.

Considering the aforementioned results, the filter-shaped MIPs were tested under the most favourable binding condition of 150 μM solution of OTC. Apart from the three samples immersed in the standard OTC solution, three filters were also tested in a solution containing a different analyte, specifically the antibiotic Sulfadimethoxine (SDMO), instead of having a non-imprinted counterpart. SDMO is another antibiotic commonly found as a contaminant in aquatic environments [106], and it was chosen to assess the material's ability to distinguish between the target molecule (OTC) and structurally different compounds, providing insights into the imprinting selectivity of the MIPs.

The results were encouraging: the MIPs immersed in the OTC solution, removed 32.5% of OTC (Table 3). As anticipated, the filters outperformed the flat disks in terms of removal percentage. The enhanced binding observed is attributed to the higher surface area and the intricate geometry, which allows a more extensive interaction with the surrounding solution containing the target. Also, the Binding Capacity (BC) was calculated, showing that the filter bound 90 μg of OTC per g of polymer. Regarding the filters incubated in the solution containing SDMO (150 μM), the spectral analysis showed that the removal of SDMO was less than half of the binding of the equivalent samples with the OTC, as shown in Figure 37 and Table 3. This suggests that the OTC-imprinted polymer exhibits a significantly higher affinity for binding with the imprinted molecule compared to others. Such results could signify another promising characteristic of the investigated MIP.

Table 3: Binding performances of filter-shaped MIP

C_S (μM)	Analyte	%Removal	BC (μg g^{-1})
150	OTC	32.5±2.1	93.7±6.2
	SDMO	14.7±5.3	42.9±15.5

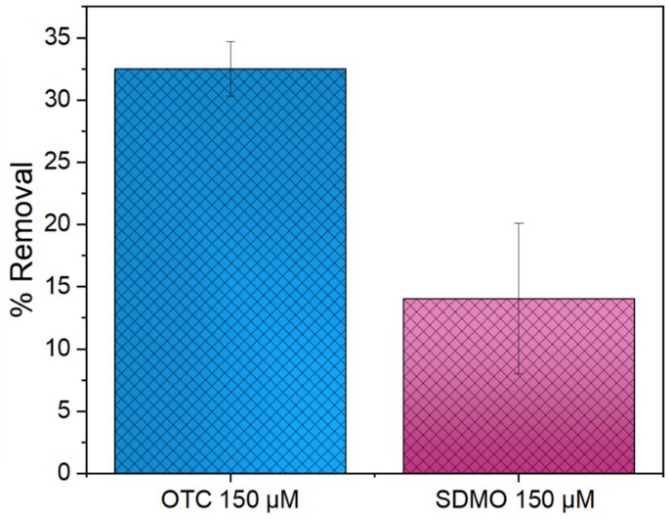

Figure 37: %Removal OTC-imprinted filters in solutions 150 μM of OTC or SDMO. Data are means of triplicate measurements.

3.2 Second Phase: Computational Investigation

In the second phase of the experimental work, a significant advancement was the incorporation of Density Functional Theory (DFT) calculations. This computational approach allowed a deeper investigation into the interactions between the template molecule (OTC) and the functional monomer (MAA). Specifically, DFT was utilized to model and analyse the binding interactions at different molar ratios, enabling the identification of the optimal ratio that minimized their interaction energy.

3.2.2 DFT Calculations

To evaluate the interaction between the template molecule (OTC) and the functional monomer (MAA), DFT calculations were conducted in two stages. Initially, the molecular system was optimized in vacuum to determine the geometrically stable structure of the OTC-MAA complex without external influences. This step provided a baseline understanding of the intrinsic molecular interactions. Subsequently, the solvent effects were introduced using a Polarizable

Continuum Model (PCM) to mimic the dielectric environment of the actual medium, specifically dimethyl sulfoxide. This allowed for a more realistic evaluation of the binding energy, reflecting the influence of solvation on the interaction.

In both cases, the counterpoise method was applied to correct for the Basis Set Superposition Error (BSSE), ensuring that the calculated binding energies accurately represented the interaction strength without overestimations caused by basis set overlap. The detailed workflow is described in Chapter 4 (Section 4.7).

The DFT calculations were performed at the B3LYP(D3BJ)/def2SVP level. Four molecular complexes with varying OTC: MAA molar ratios—1:4, 1:5, 1:6, and 1:7—were optimized using DFT. Table 4 reports the resulting binding energies. Notably, the interaction energy decreased by approximately 58% when moving from a 1:4 to a 1:5 ratio, while the change between 1:5 and 1:6 was less pronounced, showing a 5% decrease. Although the 1:7 ratio exhibited the highest binding energy, reducing the template concentration excessively may be not optimal in molecular imprinting.

Table 4: Binding Energies calculated for different template:monomer molar ratio.

OTC:MAA	**1:4**	**1:5**	**1:6**	**1:7**
Binding Energy [kcal/mol]	-46,25	-73,16	-76,84	-94,99

Balancing interaction strength with practical considerations of template concentration, the ratio 1:5 emerged as the most suitable choice. The optimized structure of this complex is depicted in Figure 38.

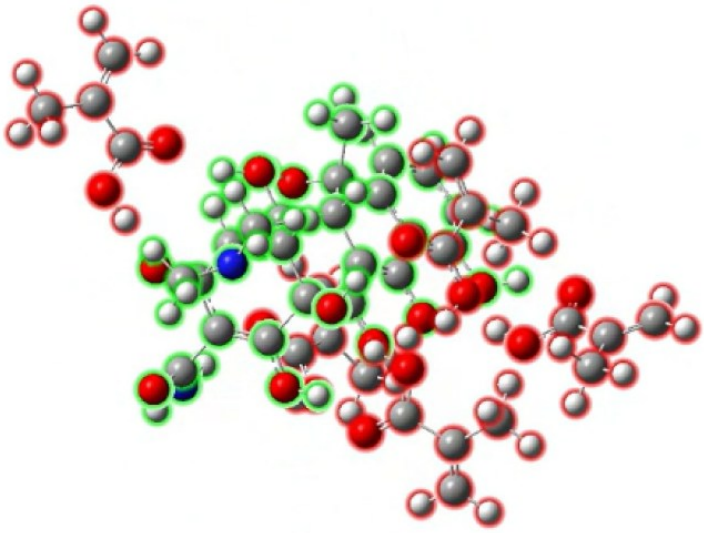

Figure 38: The complex OTC: MAA = 1: 5, optimized by DFT calculation at the B3LYP (D3BJ)/def2SVP level with the PCM solvent model (DMSO set as the solvent). Oxytetracycline molecule is in green, and Methacrylic acid molecules are in red. Result Visualization by Gauss- View 6.0.16.

Given these results, the chosen 1:5 molar ratio was implemented in all further synthesis and characterization experiments.

3.2.3 Characterization of the Formulations

The formulation was prepared with the same procedure as the previous one, with the only exception of the molar ratio. The ratio between the template, functional monomer, and crosslinker was OCT:MAA: DPGDA=1:5:20.

Rheological and photorheological characterizations were repeated for the new resin. The **rheological analysis** (Figure 39) reveals that at low shear rates, the NIP formulation exhibits a higher viscosity compared to the MIP formulation. The MIP resin demonstrates a more consistent viscosity profile across the range of tested shear rates. Both formulations display moderate shear-thinning behaviour as the shear rate increases, eventually reaching comparable low viscosity values. These viscosity measurements confirm the suitability of both formulations for DLP printing.

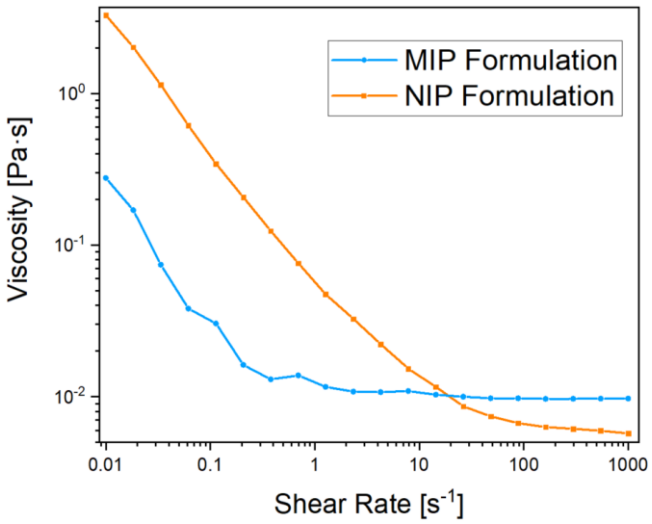

Figure 39: Viscosity of MIP and NIP formulations (1:5) under continuous shear rate sweep.

The **photorheological behaviour** of the 1:4 and 1:5 formulations did not exhibit significant differences (Figure 40). For both formulations, the NIP resin reacted rapidly upon UV exposure, completing the polymerization in approximately 20 seconds. Conversely, the MIP resin demonstrated a slower reaction time, reaching its maximum after 52 seconds. As discussed earlier, this discrepancy in polymerization kinetics can be attributed to the presence of the template molecule in the MIP formulation, which likely interferes with the network formation by competing with the photoinitiator for the UV radiation absorbance. Moreover, the two materials exhibited similar elastic moduli, as indicated by their comparable G' plateau values.

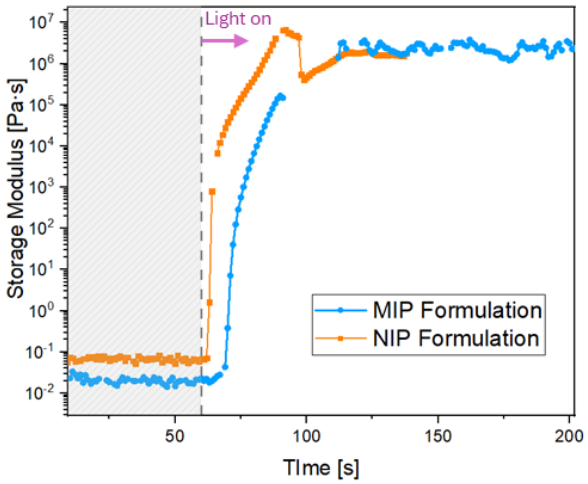

Figure 40: Real-time photorheological measure of the MIP and NIP formulations (1:5)

3.2.4 Printing New Samples

In this second phase, different samples were printed. Instead of using multi-material disks, full MIP/NIP disks were chosen. This change was made because the base layer of the multi-material disks interfered with the evaluation of specific rebinding. Indeed, it was not possible to distinguish between the specific rebinding of the MIP layer and the unspecific interactions of the thick base. Therefore, full MIP/NIP disks were printed. The diameter was maintained at 10 mm, and the height was set to 500 µm. The CAD and the pictures of printed samples are shown in Figure 41.

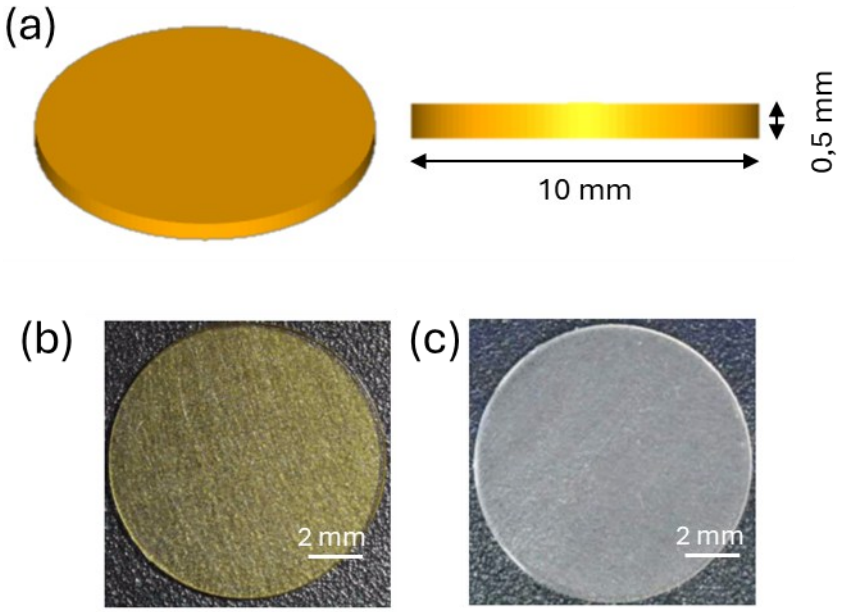

Figure 41: (a) CAD of the simple disk. Picture of the printed samples: MIP (a) and NIP (c) respectively.

To create a complex geometry with small features and a high surface area exposed to the solvent environment, also gyroid structures were printed. The CAD model of this geometry is shown in Figure 42(a). The geometry has a diameter of 9 mm and a height of 1.5 mm. The printed samples are displayed in Figure 42(b), showing a high resolution and excellent print quality.

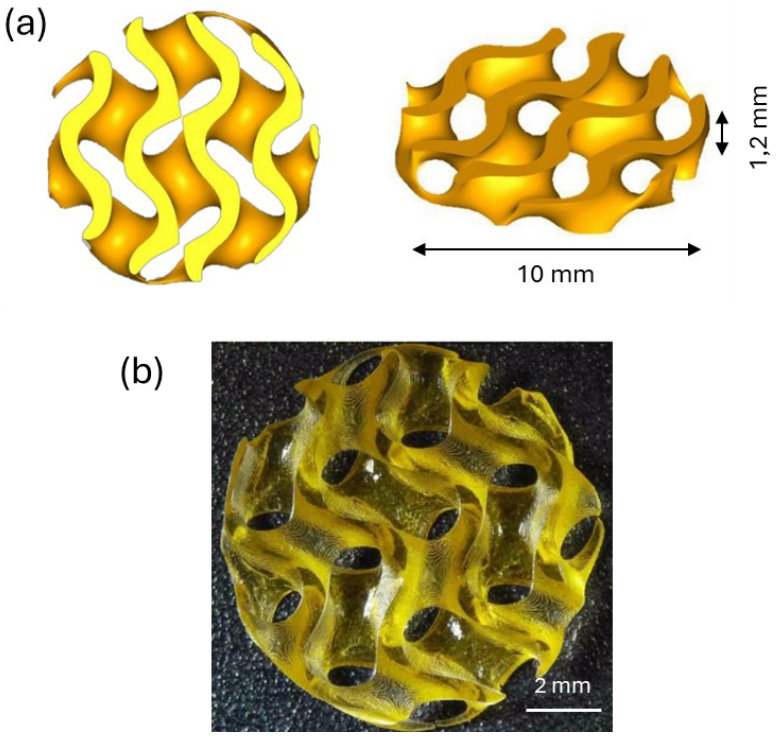

Figure 42: (a) CAD of the gyroid and (b) picture of the MIP printed sample.

Moreover, during this phase of the work, efforts were directed toward the fabrication of NIP gyroid, to have a proper non-imprinted counterpart. In the absence of OTC, which notably facilitates the printing process, a small amount of dye (0.01 phr of methyl red) was introduced as a substitute. The printing parameters were carefully optimized to ensure a satisfactory resolution, ultimately resulting in the successful fabrication of NIP gyroids (Figure 43).

Figure 43: picture of the NIP printed sample.

The same washing procedure of the filters was applied to the gyroid structures. Despite the complex geometry, the gyroids maintained good structural integrity after the washing process, demonstrating the robustness of the printed samples, as shown in Figure 44.

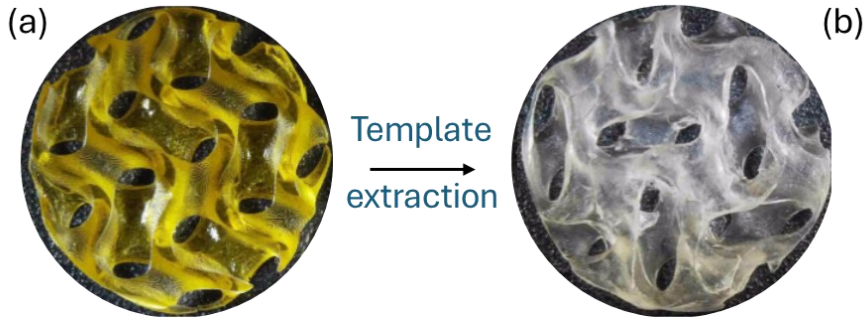

Figure 44: Pictures of the MIP-gyroid before (a) and after (b) the washing process.

3.2.5 Characterization Of The Samples

The 1:5 formulation demonstrated the capability to print high-resolution objects. This was confirmed through **3D scanning** of the printed gyroids, which revealed precise replication of the designed structures, as shown in Figure 45.

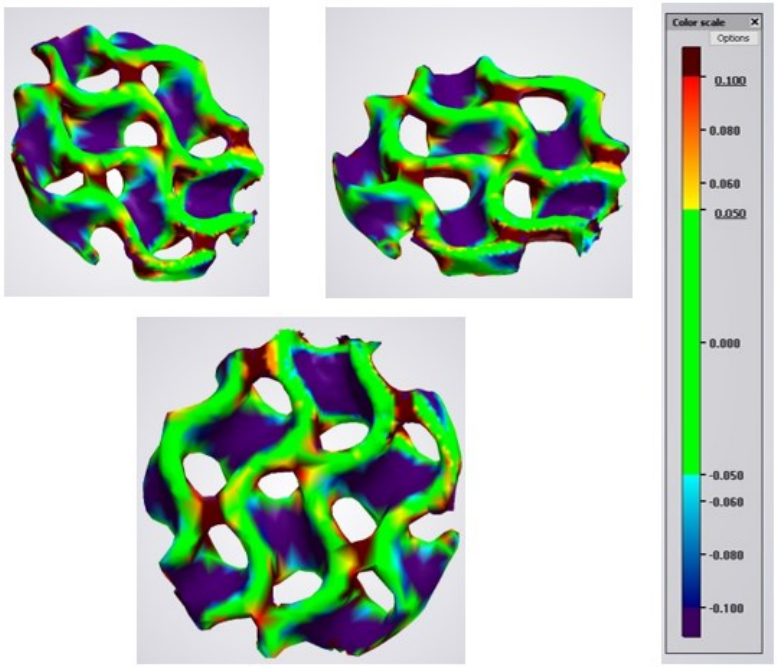

Figure 45: 3D scanning of MIP gyroid.

The **FT-IR spectroscopy** was performed also in this case. With the same procedure as above, the acrylate conversion was calculated. As shown in Table 5, both MIP and NIP resins have a high double bond conversion, of 89% and 80% respectively. It's interesting to notice that such values are higher than the formulation 1:4, which demonstrated a conversion of about 70%. This can be attributed to the higher amount of methacrylic acid.

Table 5: Percent acrylate conversion

		Liquid Formulation	Printed Sample	Acrylate conversion [%]
MIP	A_{1730}	10,95	17,3	89,8
	A_{1630}	1,04	0,17	
NIP	A_{1730}	11,15	19,66	80,8
	A_{1630}	0,96	0,32	

Interestingly, the MIP formulation exhibited a higher conversion rate than the NIP formulation. This difference could be influenced by factors such as the mobility of polymer chains during growth, which may be affected by interactions with the antibiotic. Nonetheless, the achieved conversion values confirm the formulation's suitability for DLP printing.

The spectra of the MIP and NIP formulations, as well as the printed samples, were analysed, yielding results consistent with those obtained in the first experimental phase. Figure 46 shows that the characteristic peak at 1580 cm^{-1} in the OTC spectrum is evident in both the MIP formulation and the printed sample, confirming the presence of OTC on their surfaces. Conversely, this peak is absent in the NIP spectra, as expected.

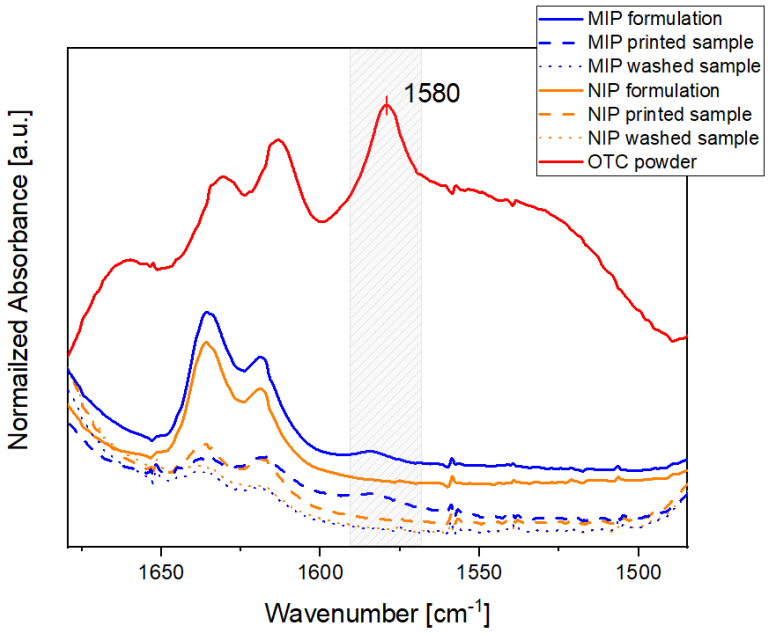

Figure 46: FT-IR spectra of liquid formulations (1:5) and printed samples, and the pure antibiotic in powder.

Additionally, the spectra were acquired for the MIP and NIP printed samples after washing. As shown in Figure 46, the peak at 1580 cm^{-1} disappears from the MIP samples, and the spectra of the MIP and NIP samples become overlapped. This observation indicates the successful removal of the template molecule from the polymer matrix.

A further analysis of these spectra was conducted to determine whether DMSO was removed during the washing procedure. A peak at 1060 cm^{-1}, assigned to the presence of DMSO (Figure 47(b)), and unrelated to OTC (Figure 47(a)), was detected in both MIP and NIP printed samples. However, this peak is substantially lower in the spectra of the washed samples, indicating that the amount of DMSO decreases after the washing procedure.

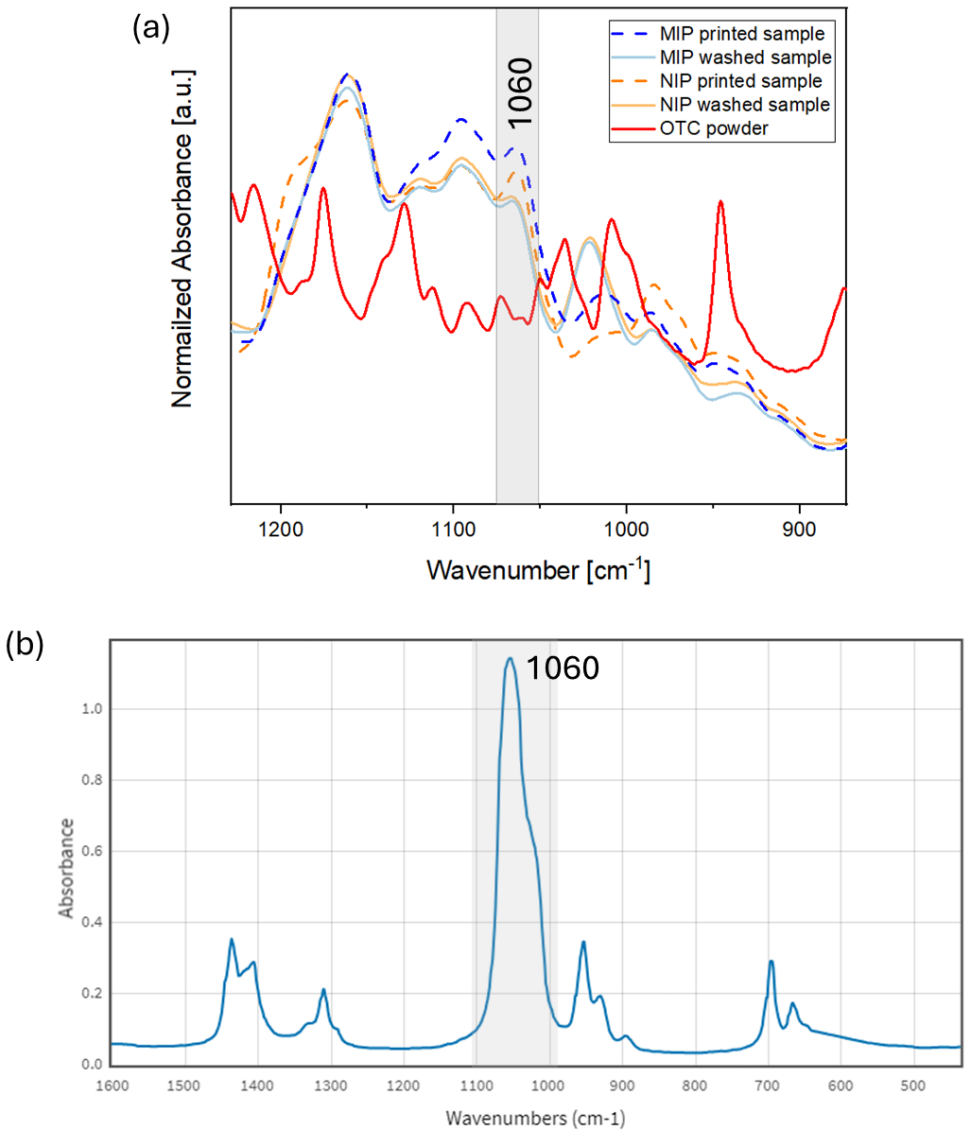

Figure 47: (a) FT-IR spectra of MIP and NIP samples both as printed and washed, and the pure antibiotic in powder. (b) IR spectra of DMSO reported from [121].

The new printed materials were also characterized in terms of thermal properties, by **Thermogravimetric** (TGA) and **Differential Scanning Calorimetry** (DSC) measures. TGA experiments and the derivative of this signal (DTG) showed that after the washing step, MIP and NIP samples have the same degradation mechanism, with two main degradation steps around 370°C and 380°C (Figure 48). This is consistent with the FT-IR experiments and indicates the successful removal of OTC.

On the contrary MIP and NIP pre-washing samples have clear differences, especially for the degradation mechanism at low temperatures (Figure 48(c)). NIP sample presents a first degradation step between 120 °C and 210 °C, which can be related to DMSO evaporation. On the other hand, MIP sample shows a shift towards higher temperatures, which can be associated to OTC degradation, as previously reported [122].

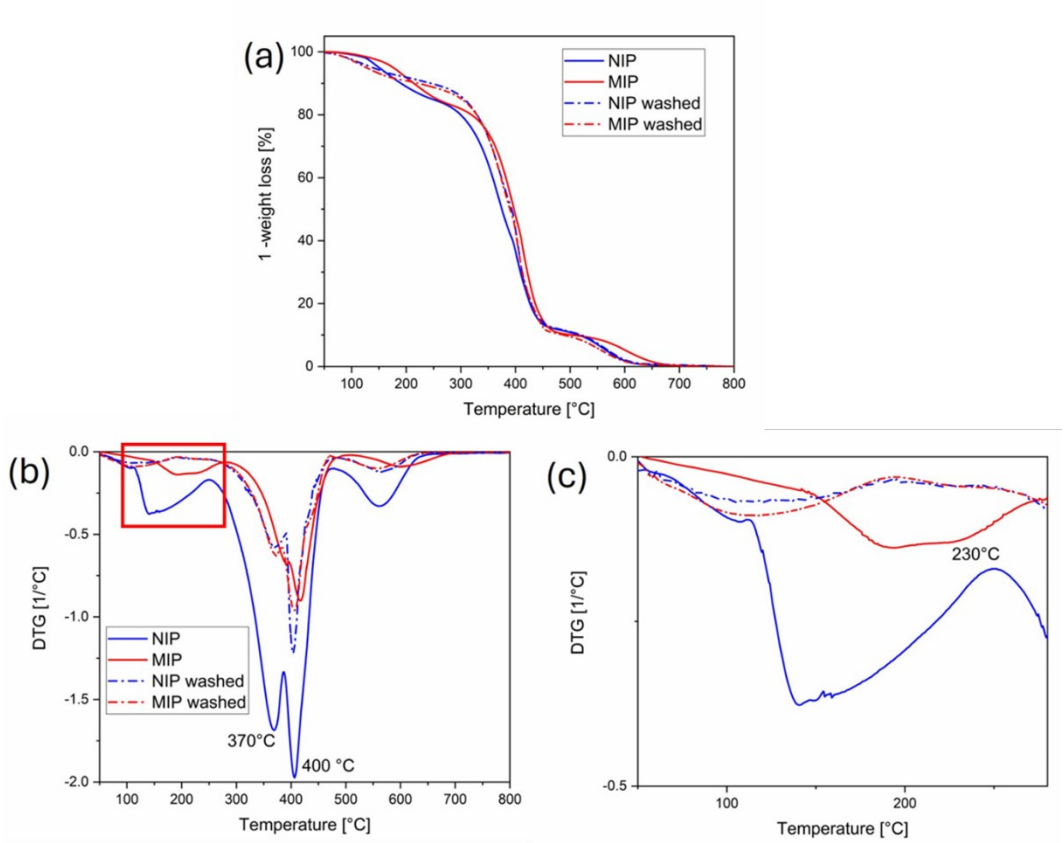

Figure 48: (a) TGA curves of NIP and MIP samples as printed and after washing step. (b) First derivative of TGA (DTG). (c) Magnification of DTG between 50°C and 270°C.

Observing DSC curves in Figure 49, it is also evident that in all the first heating cycles, an exothermic peak at temperatures higher than 100°C is present, which is not present in the second heating ramp. This peak can be associated to thermal polymerization of unreacted double bonds, which are still present in the polymeric matrix (see FT-IR results). This is consistent with the increase of T_g measure in all the samples in the second ramp except the MIP sample (Table 6).

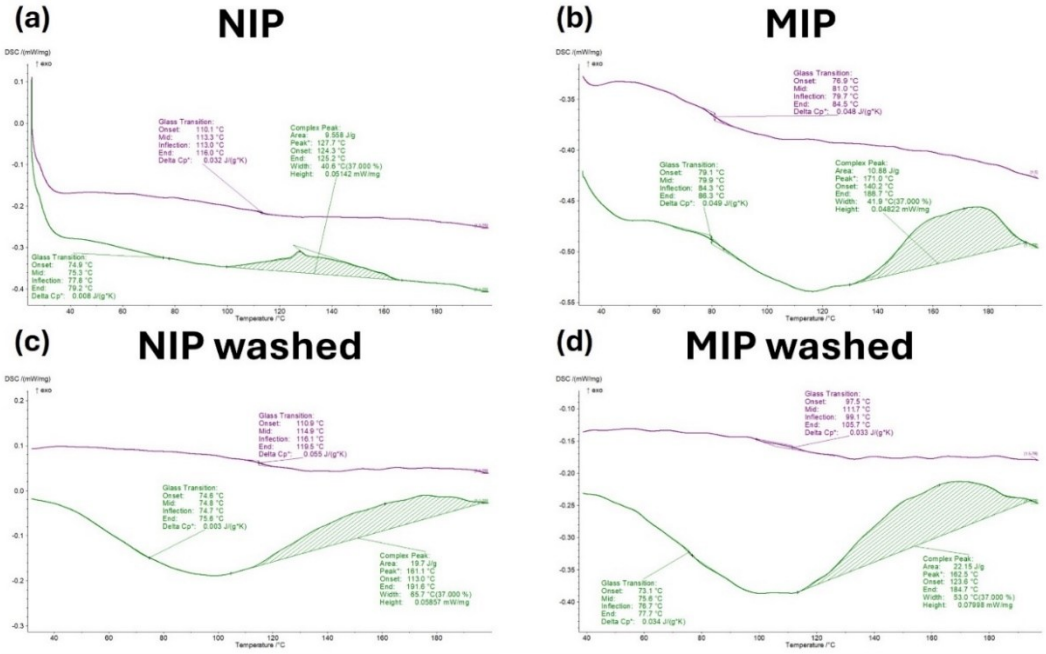

Figure 49: DSC curves of (a) NIP and (b) MIP samples after 3D printing and (c) NIP and (d) MIP samples after washing step. In all the graphs, the green curve refers to the first heating cycle, while the purple one refers to the second.

Table 6: T_g values obtained by DSC.

	T_g - first cycle [°C]	T_g - second cycle [°C]
NIP	78	113
MIP	84	80
NIP After Washing	74	116
MIP After Washing	77	100

In the MIP sample, it can be supposed that at higher temperatures degradation OTC may occur, as observed also in the TGA measures. This can affect final macromolecular organization which reflects in a different T_g. In any case, those conditions are not supposed to occur in the operational conditions of the materials.

Anyhow, both NIP and MIP are in the glassy state at room temperature, being the glass transition temperatures (T_g) above 75°C for both. This results in stiff objects easy to handle.

After the washing step all the materials maintained similar properties, demonstrating that washing step is effective for the removal of the antibiotic without damaging the structure. Unfortunately, repeated binding/washing cycles lead to stresses and damaging of the structures, which at the present stage limits the reusability of these 3D printed materials. This aspect is also under investigation for enhancements, as described in Section 3.3.2.

Atomic Force Microscopy (AFM) was performed on both MIP and NIP printed samples to evaluate their surface morphology and investigate whether the presence of the template could be detected. The surface maps in Figure 50, demonstrate an extremely low surface roughness in the nanometer range, indicating that the printing process produces highly smooth surfaces. No discernible differences in morphology were observed between the MIP and NIP samples. While AFM offers exceptional resolution, the OTC molecule is likely too small to be directly detected.

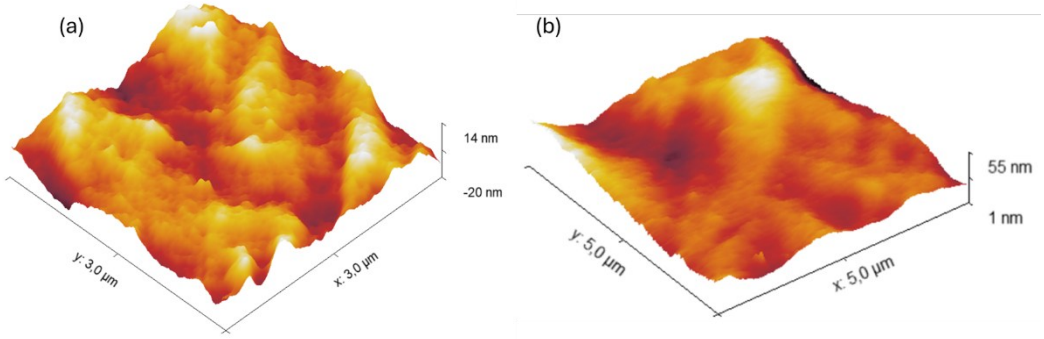

Figure 50: AFM topographic surface map of 3D-printed MIP (a) and NIP (b) samples.

As a last characterization, the effect of the washing step was also investigated by **Scanning Electronic Microscopy** (SEM). In Figure 51 micrographs of the surface of NIP and MIP samples are shown, both before and after the washing step. As expected, after 3D printing both NIP and MIP surfaces appear similar, since the only difference between the two formulations is in the presence of OTC, which has a sub-nm dimension and cannot be observed by SEM.

After the washing step both the surfaces seem smoother, but without any crack, indicating that some modification may occur in the polymer rearrangements, but without dramatically affecting the integrity of the sample.

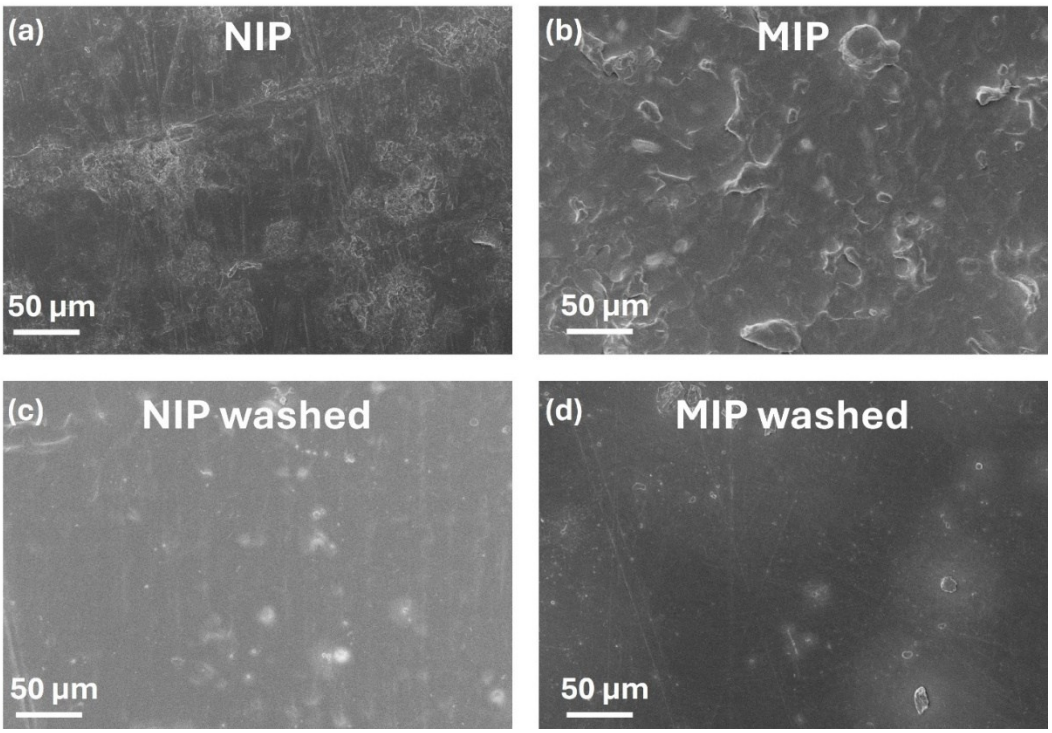

Figure 51: SEM surface pictures of (a) NIP and (b) MIP samples after 3D printing, and (c) NIP and (d) MIP samples after the washing step.

3.2.6 Rebinding: Results And Discussion

The disk and gyroid samples were tested under the same conditions as described in the previous section, with one modification: the percentage removal (%Removal) was evaluated at intervals of 3, 5, and 24 hours to assess temporal behaviour.

The rebinding performance of the disk samples was tested first, revealing a moderate rebinding capability. These samples achieved a removal of 6.3%, with a gradual increase over time, as shown in Figure 52. Specific rebinding by the MIPs consistently exceeded the non-specific rebinding observed in the NIPs, although some non-specific interactions were still present.

Interestingly, the %Removal for the disk samples was comparable to that of the multi-material disks discussed in Section 3.1.6. This suggests that the binding of the target molecule primarily occurs at the surface of the objects, with minimal contribution from the bulk volume. This hypothesis is further supported by the observation that in the simple disk geometry, the specific %Removal shows only a modest increase over time, indicating a rapid saturation of binding sites.

Notably, the level of non-specific rebinding in the disk samples was lower compared to the multi-material disks. This reduction can likely be attributed to the absence of the additional "base" layer present in the multi-material samples, which contributes to non-specific interactions.

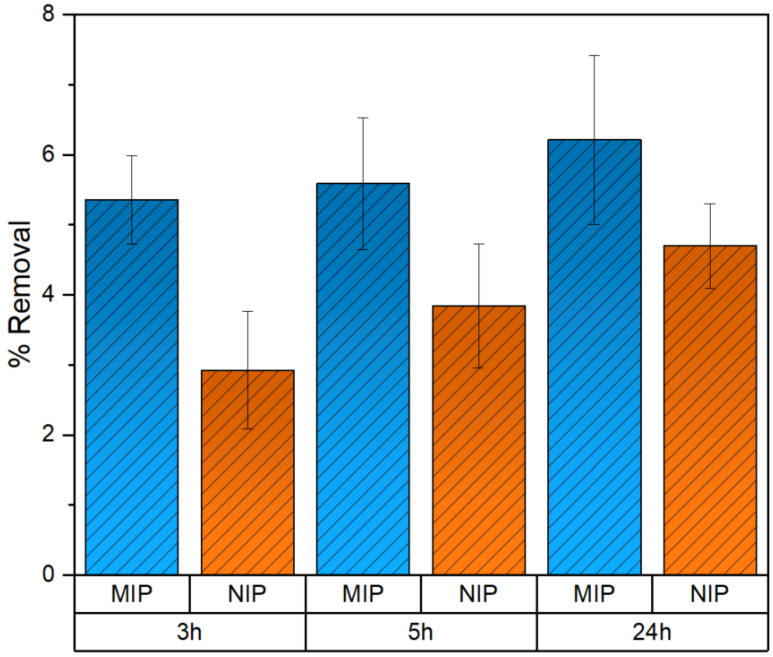

Figure 52: %Removal of the MIP and NIP disks, in solutions of 150 μM of OTC. Data are means of triplicate measurements.

Next, the gyroid were tested. This complex structure demonstrated promising results. The higher surface area exhibited by the samples led to a steady increase over time of the %Removal, exceeding 18% after 24 hours, as shown in Figure 53. While non-specific rebinding also increased, it remained significantly lower compared to the MIP-specific binding.

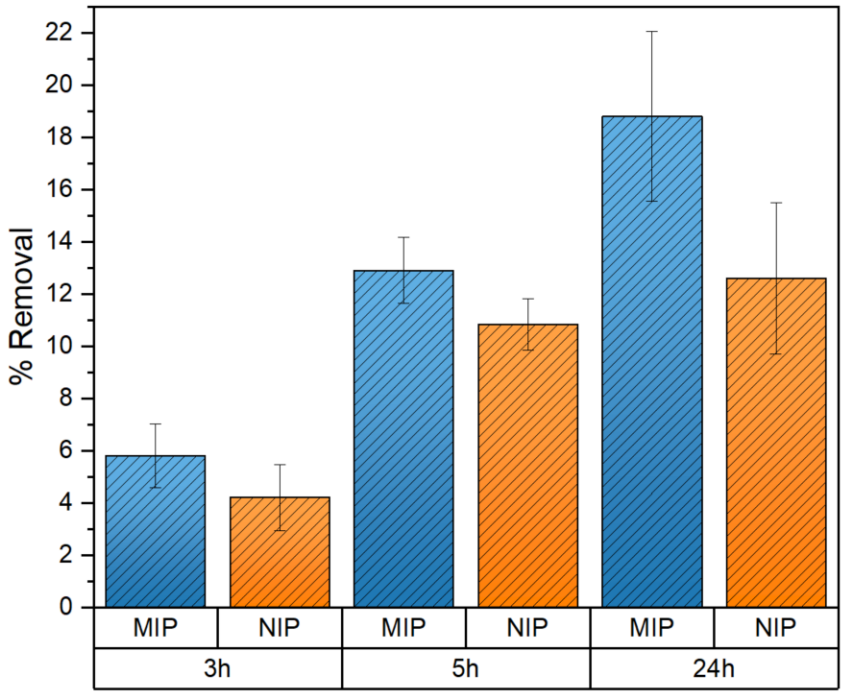

Figure 53: %Removal of the MIP and NIP gyroids, in solutions of 150 μM of OTC. Data are means of triplicate measurements.

As expected, the gyroids demonstrated superior performance compared to the disks, highlighting the enhanced potential of the gyroid geometry for capturing the target molecule. In Table 7 the performances are given in terms of %Removal, Imprinting Factor and Binding Capacity.

Table 7 :Comparison between MIP and NIP performances, of disks and gyroid samples.

Geometry	*Sample*	*%Removal*	*IF*	BC [μg g^{-1}]
Disk	MIP	15.65±3.4	1.7	55.5±10.7
	NIP	9.19±3.0		41.72±5.3
Gyroid	MIP	18.8±3.2	1.5	187.66±32.4
	NIP	12.6±2.9		125.8±28.93

In conclusion, the performance of the different MIP geometries was compared, revealing important insights into their binding capabilities. As just said, the gyroid samples demonstrated superior removal efficiency compared to the disk-shaped samples, likely due to their increased surface area and optimized geometry.

On the other hand, when comparing the gyroids to the filters reported in the previous section (keeping in mind that the resin formulation is different), the filters might initially appear more efficient: the %Removal of the filters was 32.5%, versus 18.8% of the gyroids. However, it must be noted that the filters were substantially larger in size compared to the samples. The better performance of the gyroids is evident when examining the Binding Capacity, which reflects the amount of target bound per gram of polymer. As shown Figure 54, the BC in the gyroids was found to be twice that of the filters, highlighting their superior efficiency in capturing the target molecule.

The improved performance of the gyroids can be attributed to their geometry, characterized by more intricate features that allowed a higher exchange with the solvent, as well as the optimized formulation.

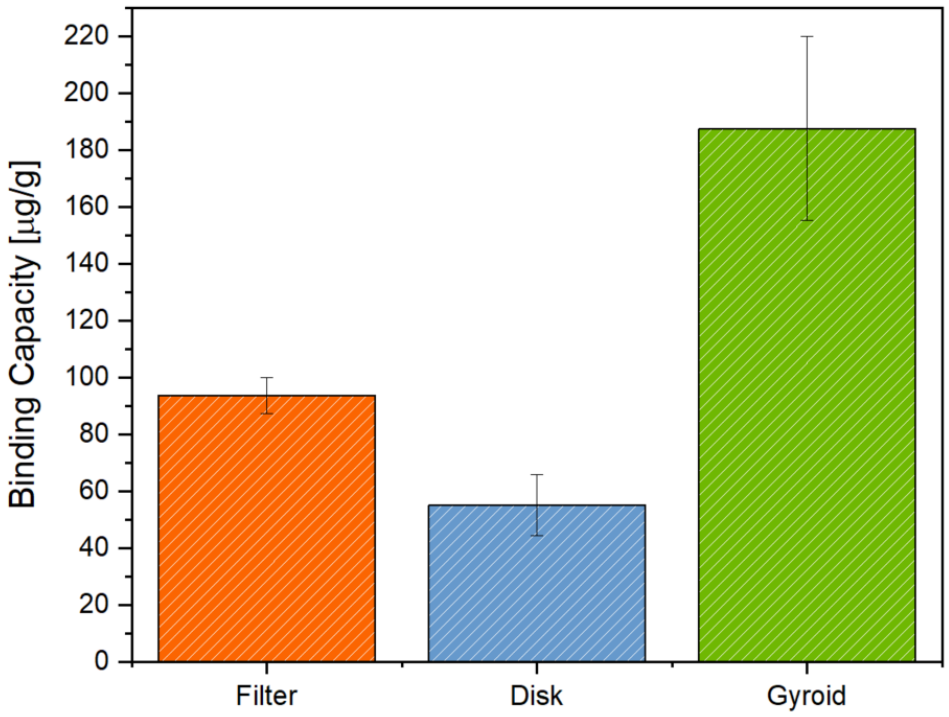

Figure 54: Comparison in terms of Binding Capacity between three different geometries, the filter (formulation 1:4), the disk and the gyroid (formulation 1:5).

3.3 Additional Tests

3.3.1 Exploring Micrometric Porosity

In an effort to enhance MIPs' performance, additional experiments were conducted to explore the inclusion of micrometric porosity in the printed samples. The aim was to combine the well-established technique of salt leaching with the complex shaping capabilities provided by additive manufacturing. This approach sought to increase the surface area of the samples and evaluate whether this would lead to improved binding performance.

Three formulations were prepared, maintaining the molar ratio of OTC:MAA:DPGDA = 1:5:20, and adding 20 phr of salt. For these experiments, common NaCl salt was manually ground using a mortar before being mixed with the other components. As usual, the resin mixtures also included 0.8 phr of BAPO as the photoinitiator and 15 phr of DMSO as the solvent. The preparation procedure followed the same steps described in the earlier sections of this thesis. The differences lie in the addition of salt in the resin, and in its removal after the printing. The removal of the salt is done by immersing the samples in water, before the template extraction in methanol and acetic acid.

The incorporation of salt into the resin introduced some complexities in the printing process. Indeed, the salt tended to precipitate during the printing. Moreover, its presence affected the fidelity of the printed samples to the CAD, resulting in samples with layer thicknesses greater than expected and an overall decreased resolution.

The multi-material disks were printed, including the salt exclusively in the MIP/NIP layer and not in the base. FESEM images of these samples reveal the presence of micrometric porosity in the MIP/NIP layer, while the base appears compact and with no pores (Figure 55). However, the lack of interconnectivity among the pores is evident.

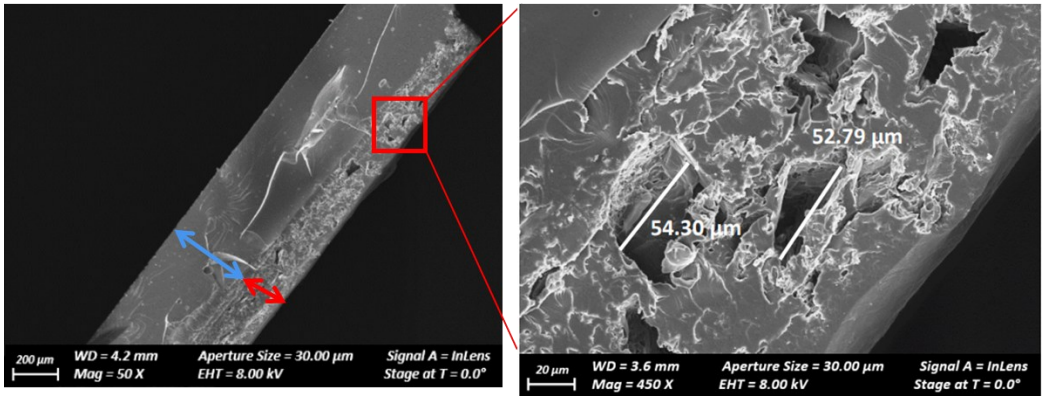

Figure 55: FESEM image of NIP disk, after the washing of the salt particles. The blue arrow indicates the "base", without any porosity, and the red arrow indicates the NIP layer, with the pores.

Also, a simplified version of a filter, featuring only one thick floor, was printed. The CAD is shown in Figure 56(a). Additionally to the MIP filters (Figure 56(b)), also NIP filters were fabricated, adding 0.8phr of methyl red dye to assist with the printing process (Figure 56(c)).

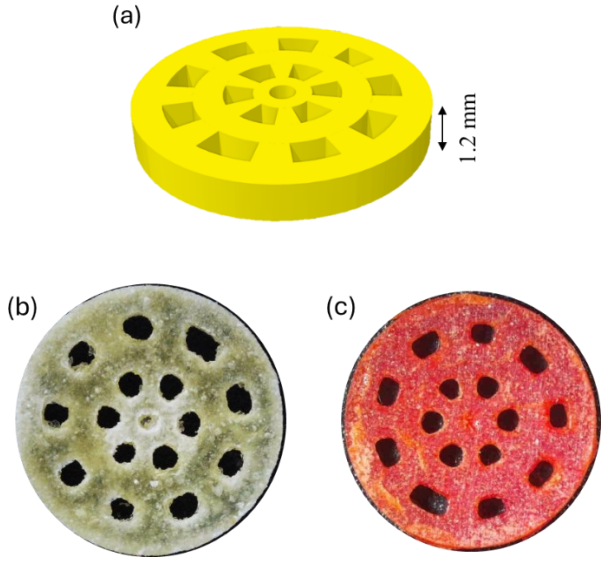

Figure 56: (a) CAD of a single floor filter. Picture of the filters printed including the salt particles, MIP (b), and NIP (c). The red colour of the NIP filter is due to the presence of a dye.

In the FESEM image shown in Figure 57, the printing layers of the MIP filters are visible. It's possible to see that the layers are thicker than they should be (around 200 µm instead of the 100 µm set as slice thickness on the printing software).

Moreover, the pores are visible, even if neither interconnected nor homogeneous (Figure 58).

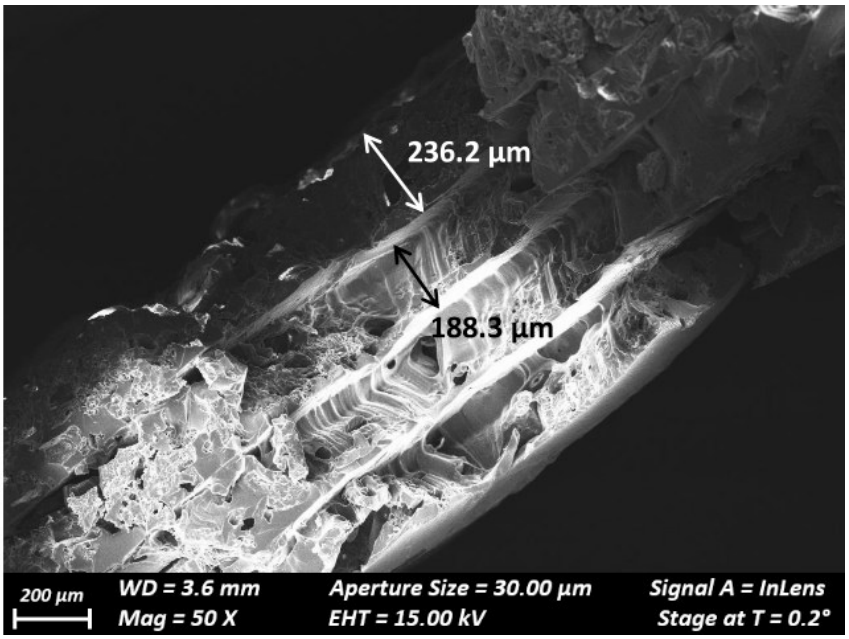

Figure 57: FESEM image of a MIP filter. In the section of the sample, the non-homogeneous printing layers are visible.

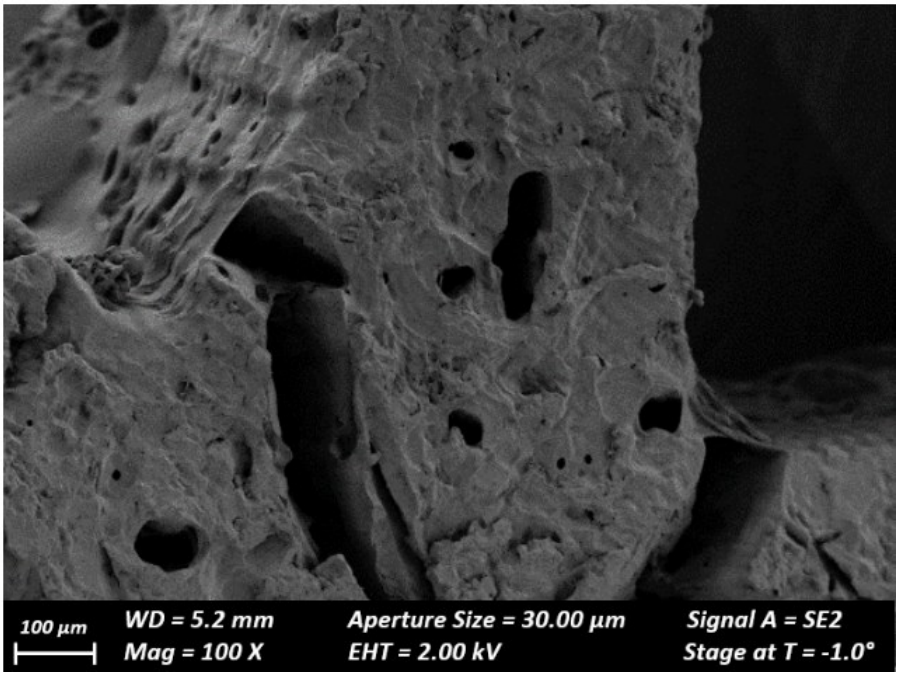

Figure 58: Some pores noticeable on the surface of a NIP filter.

A preliminary rebinding test was performed with the MIP and NIP filters, in a solution of 100 µM of OTC in deionized water. After 72 hours, the percent removal resulted not particularly improved compared to non-porous filters, and with a significant non-specific removal. Indeed, the MIP filters rebound only 8.2% more than the NIP ones (Figure 59).

The lack of interconnected pores likely hindered the exchange efficiency with the rebinding solution, limiting the effectiveness of the porosity. Furthermore, for a given weight of the sample, the amount of template (and therefore the degree of imprinting) was lower in the porous filters compared to their non-porous counterparts.

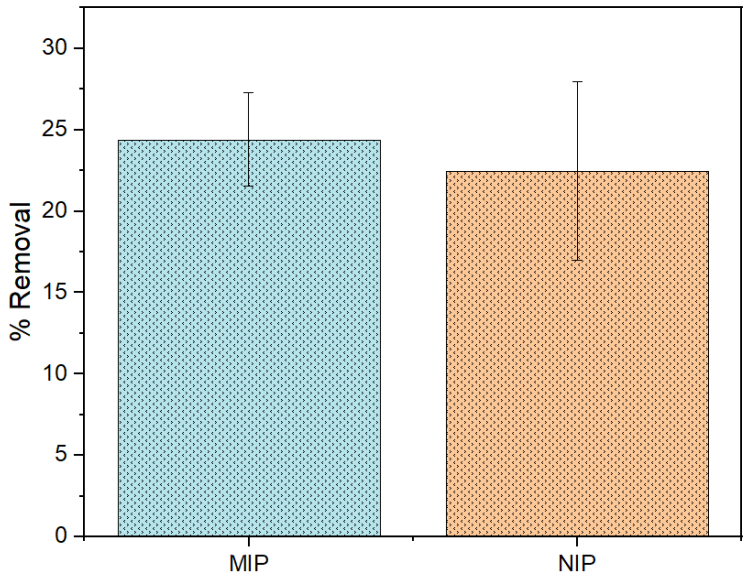

Figure 59: Percent removal in MIP and NIP single-floor, porous filters.

In any case, it should be noted that, due to changes in samples' geometry and volume, a direct comparison between this and previous experiments is not entirely consistent.

Despite these challenges, the results should not discourage further efforts to incorporate porosity into 3D-printed MIPs. Process optimization could potentially address the "bulkiness" of the 3D-printed MIP, enabling easier extraction of the template, and a general better performance and functionality.

3.3.2 Exploring Reusability

An additional aspect explored in this work was the potential reusability of the 3D-printed MIP samples. The purpose of investigating reusability stems from the desire to make MIP more sustainable and cost-effective. Reusable objects could significantly lower the costs associated with their production and application, as fewer new materials would be needed over time. A reusability strategy aligns with the sustainability purpose of the work itself. Additionally, this capability could expand the range of applications for MIPs, making them more practical for real-world scenarios where repeated use is often a key requirement.

Therefore, some disks and gyroid samples were tested in this direction. After completing the initial rebinding process, the samples were subjected to a second washing step under the same conditions as the first washing procedure. However, the main limitation in reusability was the important structural damage and surface modifications observed.

Although the secondary washing led to the release of the previously bound antibiotic, testing such compromised samples for a secondary rebinding would misrepresent their specific binding capabilities. This damage to the polymer matrix may stem from the repeated exposure to alternating solvents, such as the organic washing solution and the water-based rebinding solution, which can induce stress on the material. The impact of this process was more pronounced in thinner, more fragile geometries, as the disks (Figure 60 (1) and (2)). On the other hand, the gyroid geometry maintained better structural integrity, with fewer compromises (Figure 60 (3)).

To improve the reusability of these devices and correctly test the ability of repeated binding, future work should focus on refining the washing protocol to fully regenerate the samples while minimizing structural damage. Additionally, prioritizing the development of robust and intricate geometries like gyroids could enhance the durability and performance of the devices during repeated use cycles.

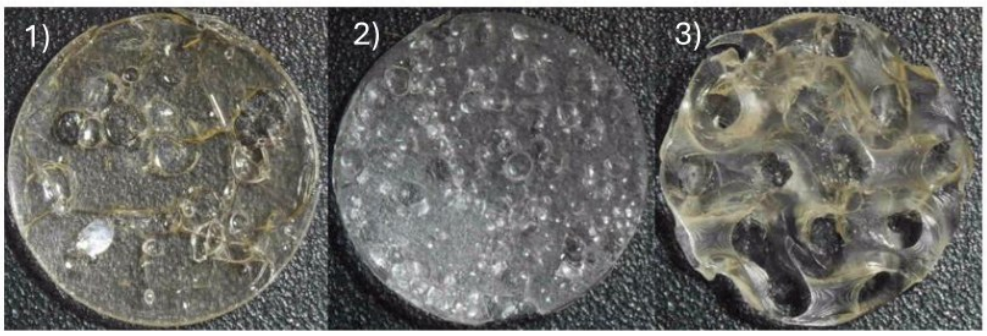

Figure 60: Samples washed after the rebinding (1) MIP disk, (2) NIP disk, (3) MIP gyroid.

3.4 Conclusions And Future Work

This thesis represents a significant step forward in the integration of DLP 3D printing with Molecular Imprinting Technology, showcasing its potential to create innovative materials for environmental remediation. By fabricating macroscopic, self-standing MIP structures tailored for the selective removal of antibiotics from water, this work introduces a novel approach that bridges molecular recognition with advanced manufacturing techniques.

The results highlight the versatility and promise of 3D-printed MIPs, particularly for addressing complex environmental challenges. Indeed, the reported experiments validate the material's capability to collect the target molecule from the aqueous solution. It's important to notice that the performances are quite limited compared to the well-established techniques that usually involve MIP in nanoparticles, which for the removal of OTC may reach over 80% of removal and binding capacity in the order of mg g^{-1} [117][110][112][113]. However, a direct comparison with established studies on nanoparticles MIPs would be inherently biased, as nanoparticles typically exhibit significantly higher surface area, and thus higher site accessibility and faster mass transfer compared to the bulkier, macroscopic polymers presented here.

On the other hand, the few existing studies on 3D-printed MIPs have substantial differences in terms of template molecules and polymer composition [19][57]. Nonetheless, the binding capacity observed in this work is in line with the results reported in such studies, consistently with the novelty of the fabrication technique.

Despite these promising outcomes, several challenges remain. Reproducibility emerged as a significant limitation, with variability observed in the fabrication process and binding performance of the MIPs. Additionally, the reusability of the

samples was constrained by structural damage and degradation, likely stemming from repeated exposure to alternating solvent environments. These challenges underline the need for further refinement in material design and process optimization.

Future work should prioritize enhancing the mechanical and chemical resistance of the polymer matrix to improve the reusability of 3D-printed MIPs. Introducing controlled porosity into the structures represents another key direction, as porous geometries could display an increased surface area and thus improve the target interaction with the imprinted cavity. Ultimately, the goal is to explore practical implementation in environmental systems, such as water filtration devices or integrated sensing platforms.

Chapter 4

Experimental Apparatus and Methodologies

4.1 Materials

Oxytetracycline hydrochloride, methacrylic acid, Phenylbis(2,4,6-trimethylbenzoyl)phosphine oxide (BAPO), dimethyl sulfoxide, Methyl Red and Sulfadimethoxine were purchased from Sigma-Aldrich (Milan, Italy). Dipropylene Glycol Diacrylate was purchased by Allnex.

4.2 Formulation preparation

The photocurable ink was prepared by mixing the oxytetracycline and the methacrylic acid, with a template: functional monomer: crosslinker molar ratio of 1:4:20 or 1:5:20, depending on the experiment. The addition of a solvent was deemed necessary due to the difficulty of dispersing the OTC, and the minimum quantity of DMSO required for a clear pre-polymerization complex solution was determined to be 10.6% wt. The solution underwent stirring for one hour at room temperature. Separately, BAPO (0.8% of crosslinker) was added to the crosslinker, DPGDA, and dissolved with the help of an ultrasound bath.

The crosslinker solution was then added drop by drop into the other one, while stirring. The solution was thoroughly mixed until achieving homogeneity, as verified by the transparency of the formulation. At this point, the photocurable MIP formulation was obtained. For the Non-Imprinted Polymers (NIPs) formulation, the OTC was excluded. In Figure 61, a picture of the prepared formulations. To print the NIP gyroids, Methyl Red was added to the resin (0.01 phr).

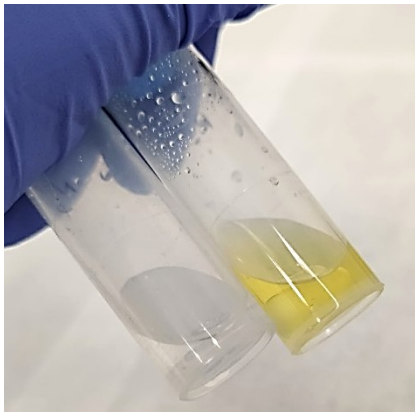

Figure 61: Pictures of the two formulations: NIP (transparent) and MIP (yellow).

4.3 Characterizations

Viscosities of MIP and NIP formulations were evaluated through rheological measurements by the Anton Paar Physica MCR 302 rheometer, in a 25 mm diameter parallel plate mode, with a gap of 0.2 mm between plates and constant temperature of 25°C. The rotation shear ramp test was performed between 0.01 s^{-1} and 1000 s^{-1}. To evaluate the effect of the antibiotic on the kinetic of the photopolymerization, real-time photorheology measures were performed. OTC absorbs in the range of exposure of the DLP, competing with the photoinitiator in the absorbance of light.

The formulations with the antibiotic (MIP resin) and without the antibiotic (NIP resin) were compared. Photorheology of the two formulations was performed with the Anton Paar MCR 302 rheometer in plate-plate configuration. The light source was a Hamamatsu Photonics C8 UV lamp, with a light intensity of 50 mW cm^{-2}. The real-time photorheology was performed with a quartz bottom plate, temperature set to 25°C, and with 1% strain amplitude and angular velocity of 10 rad s^{-1}. After the stabilization time (60 s), the light was turned on and the change in the viscoelastic properties of the material during polymerization was measured over time.

UV-visible spectra of both resin and printed object were collected to compare MIP and NIP, using the BioTek Synergy HTX Multi-Mode Microplate Reader (Agilent), in the range 250-450 nm.

Moreover, Fourier Transform Infrared (FT-IR) spectroscopy was conducted on the liquid formulations and printed samples. Thermo Fisher Scientific Nicolet™ iS50 Spectrometer was used, in attenuated total reflectance (ATR) mode, in the range of 4000–550 cm^{-1}. The degree of conversion was determined by calculating the area at the peak corresponding to the C=C bond (1638 cm^{-1}) before and after polymerization. The quantification of the peak areas was carried out with Omnic™ Software (Thermo Fisher Scientific) after the normalization at the peak of the C=O bond at 1720 cm^{-1}, as it remains unaffected by the polymerization process.

Thermogravimetric analysis (TGA) was performed using a Netzsch TG 209 F1 Libra instrument in the range between 25 and 800 °C, with a heating rate of 10 °C/min in air atmosphere (flux 50 ml min^{-1}). The first derivative of TGA (DTG) was employed to evidence degradation mechanisms. Differential scanning calorimetry (DSC) measurements were performed with a Netzsch DSC 204 F1 Phoenix instrument, equipped with a low temperature probe. All the tests were performed in nitrogen atmosphere with the following thermal method: between 20°C and 200 °C with a heating rate of 10 °C min^{-1}, 10 minutes isothermal at 200°C, cooling cycle 200°C-20°C with a cooling rate of 10 °C min^{-1}, 15 minutes at 20°C, second heating cycle between 20°C and 200 °C with a heating rate of 10 °C min^{-1}. The T_g was defined as the midpoint of the heat capacity change observed in the DSC thermogram and calculated with Proteus software.

The Atomic Force Microscopy (AFM) was operated by Bruker Innova, in tapping mode, with a 300 kHz resonance frequency. The probe tip used was the RTESPA-300. The images were post-processed using Gwyddion software.

The morphology of the sample was also investigated by a Zeiss Supra 40 FESEM, equipped with a GEMINI II column and EDS analyzer, where a probe current of 1200 pA and an accelerating voltage between 5.00 and 15.00 kV were used.

4.4 3D Printing and 3D scanning

The Asiga MAX X UV 27 DLP printer was employed (Figure 62), with a LED light irradiation at 385 nm. The CAD models were designed with Rhinoceros

software and then uploaded in *.stl* format in the proprietary printer software (Asiga Composer). The diameter of all the objects was 10 mm, to fit the samples inside the wells of a 48-multi-well plate, in which the different stages of the experiment take place.

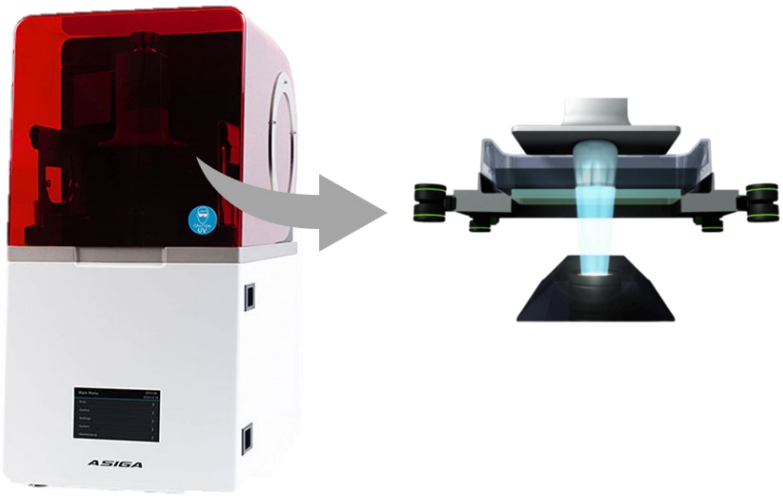

Figure 62: The employed priter, Asiga MAX X UV 27 DLP printer

For the fabrication of the multi-material disks, the first 500 µm of the structure were printed using a resin formulation containing only the crosslinker and the photoinitiator. Once this initial portion was completed, the printing process was paused, and the resin in the vat was replaced with the MIP or NIP resin formulation. The final 50 µm of the disk, representing the active layer, were then printed.

Layer thickness, light intensity, and exposure time depend on the formulation (MIP/NIP) and the geometry of the object. In the following tables, the detailed printing parameters are listed for each type of sample and formulation.

Table 8: Printing parameters of samples of formulation 1:4:20 (OTC:MAA:DPGDA)

MIP - disk	Burn-in	Range 1	Range 2
Range thickness (µm)	0-100	100-500	500-550
Light Intensity (mW/cm^2)	20	20	48
Exposure Time (s)	4.5	3.5	33.5
Slice Thickness (µm)	50	50	25

NIP - disk	Burn-in	Range 1	Range 2
Range thickness (µm)	0-100	100-500	500-550
Light Intensity (mW/cm^2)	20	20	40
Exposure Time (s)	4.5	3.5	5
Slice Thickness (µm)	50	50	25

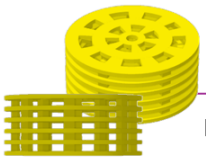

MIP - filter	Burn-in	Floors	Pillars
Range thickness (µm)	0-100	200	500
Light Intensity (mW/cm^2)	40	40	41
Exposure Time (s)	30	30	32
Slice Thickness (µm)	50	50	50

Table 9: Printing parameters of samples of formulation 1:5:20 (OTC:MAA:DPGDA)

MIP - disk	Burn-in	Range 1
Range thickness (µm)	0-200	200-500
Light Intensity (mW/cm^2)	50	47
Exposure Time (s)	32	35
Slice Thickness (µm)	25	50

NIP - disk	Burn-in	Range 1
Range thickness (µm)	0-200	200-500
Light Intensity (mW/cm^2)	20	20
Exposure Time (s)	3.5	4.5
Slice Thickness (µm)	25	50

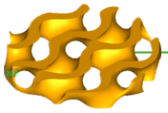

MIP - gyroid	Burn-in	Range 1
Range thickness (µm)	0-200	200-1500
Light Intensity (mW/cm^2)	50	47
Exposure Time (s)	32	35
Slice Thickness (µm)	25	40

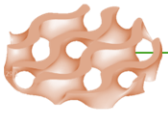

NIP - gyroid	Burn-in	Range 1
Range thickness (µm)	0-100	200-1500
Light Intensity (mW/cm^2)	20	20
Exposure Time (s)	6	5
Slice Thickness (µm)	15	40

The accuracy of the printed objects to the CAD model was evaluated by the 3Shape E3 scanner, whose acquisition was compared to the CAD models by a proprietary scanner software to obtain the deviation map. After printing, the samples undergo two post-polymerization steps. First, they are washed in ethanol to remove any unpolymerized resin, and then post-cured in a UV chamber (Asiga Flash) for 120 s to finalize the polymerization.

4.5 Washing Process and Rebinding

To remove the template within the polymer matrix, the samples go through a washing procedure using a solution of methanol and acetic acid (9:1 v/v). The samples are immersed in the washing solution and then placed in an ultrasound bath or on a tilting platform for several hours, depending on their volume. The washing is considered completed when the UV-vis spectra of the solutions no longer show the characteristic peak of the OTC at 355 nm.

After the washing process that emptied the binding cavities, the samples were ready to interact with the solution containing the target molecule. Thus, the batch rebinding takes place, meaning the MIPs fully immersed in a solution of deionized water and OTC, at the defined concentration depending on the experiment. The samples were placed in a well of a 48-well plate, immersed in 750 µL of the binding

solution, and left on a tilting platform, inside an incubator to maintain the temperature stable at 26°C (Figure 63).

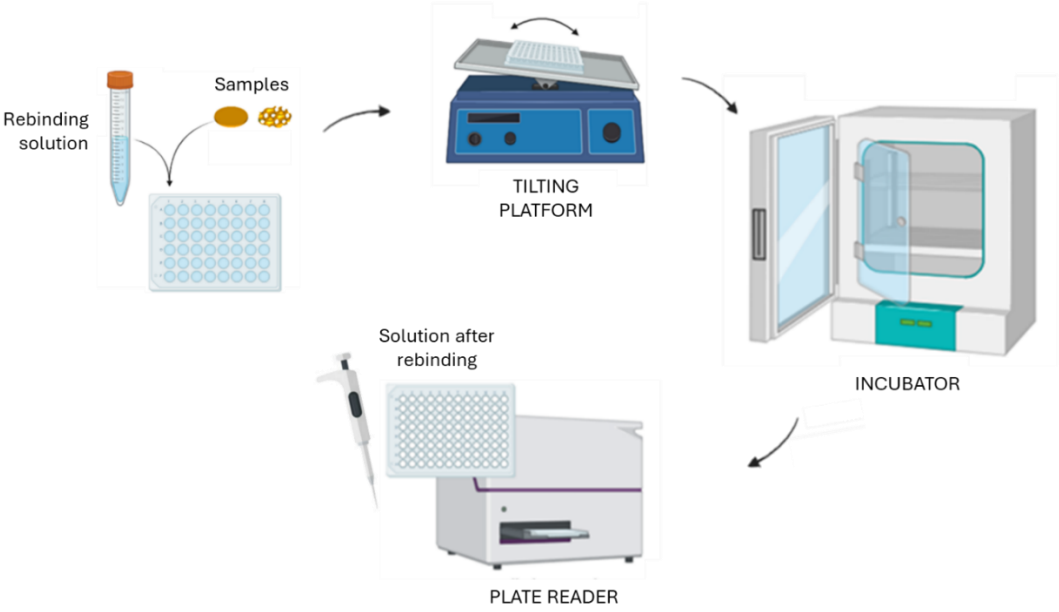

Figure 63: Rebinding process. The samples are immersed in the rebinding solution and placed on a tilting platform inside an incubator for a defined period. After this time, an aliquot of the rebinding solution is collected, and its spectrum is compared to that of the solution before rebinding.

To assess the binding ability of the samples, UV-visible spectra of aliquots of the binding solutions were acquired both before and after exposure to the polymer, allowing a comparative analysis. Specifically, spectrophotometry was performed using the BioTek Synergy HTX Multi-Mode Microplate Reader (Agilent), in the range 300-450 nm, 1 nm intervals, and a UV-Vis-NIR Spectrophotometer Cary 5000 (Varian, Agilent) was used, range 200-450 nm, 1 nm intervals. Figure 64 presents an example of the spectra of the rebinding solution, illustrating the comparison before and after contact with the samples.

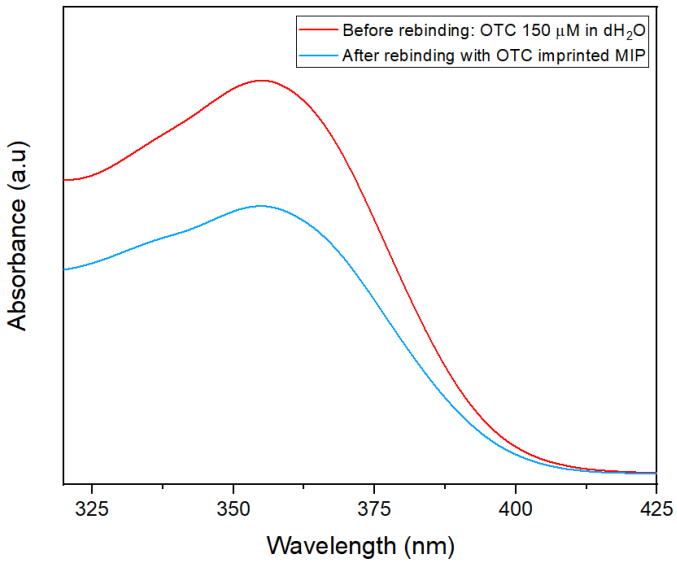

Figure 64: Uv-vis Absorbance spectra of the OTC solution before the rebinding (in red) and after it (in blue). The decrease in the absorbance implies a decrease of concentration of the target molecule.

The calibration curve of the OTC was obtained, to predict the concentration in an unknown sample through the Beer-Lambert law. Figure 65(a) shows the spectra collected at different molarities of OTC, and Figure 65(b) the resulting calibration curve.

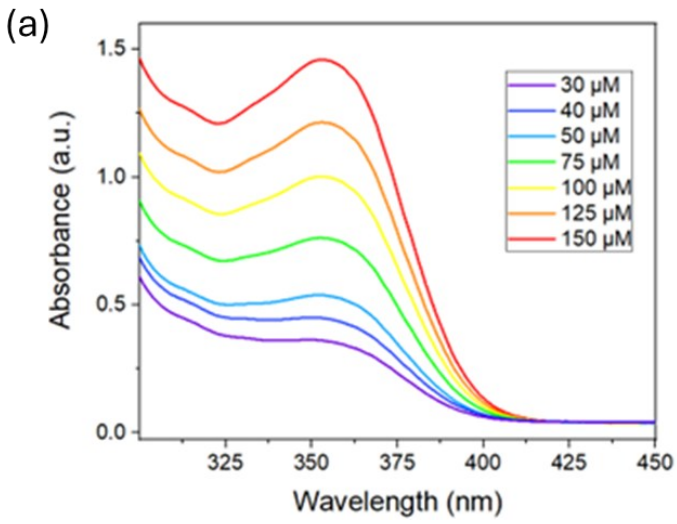

(b)

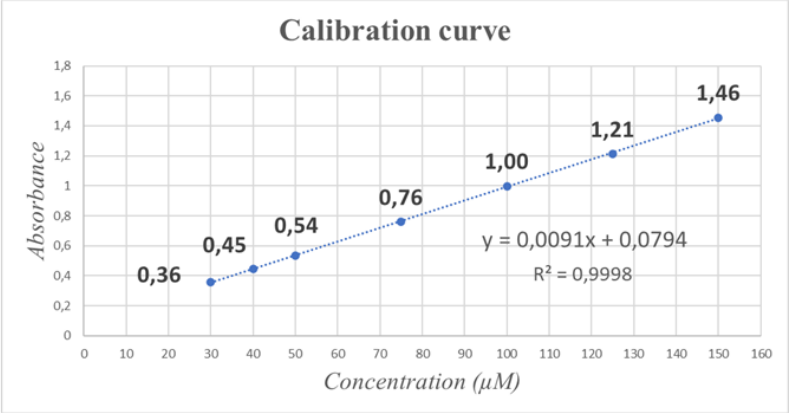

Figure 65: (a) UV-vis absorbance spectra of the Oxytetracycline solution in water, at different concentrations. (b) The resulting calibration curve.

The absorbance values were translated into concentrations, and the binding performances were evaluated, calculating the removal percentage, the imprinting factor, and the binding capacity.

4.7 Computational Analysis of MIP Components

To design the MIP, DFT calculation was performed by Gaussian 16 at the B3LYP(D3BJ)/def2SVP level with the IEFPCM solvent model. Gaussian is a widely used computational chemistry software package designed to perform electronic structure calculations. It is named after the Gaussian functions used in the computations. The resulting optimized geometries were visualized by GaussView 6.0.16.59 Four. The binding energies at different molar ratios were calculated at the B3LYP/ def2TZVP level, using the counterpoise method.

The workflow for DFT Calculations included the following steps:

1. **Geometry Optimization** (in vacuum): the molecular system comprising OTC and MAA was carefully set up to allow potential interactions such as hydrogen bonding. Geometry optimization was then performed to identify the lowest-energy configuration of the OTC-MAA complex, ensuring that the spatial arrangement of the molecules represented their most stable structure without interference from external environmental factors (in vacuum).
2. **Binding Energy Calculation** (in vacuum): this calculation required determining the total energy of the complex system and separately calculating

the energies of the individual OTC and MAA molecules using the same basis set. The binding energy ΔE was derived from these values using the formula:

$$\Delta E = E_{complex} - (E_{OTC} + \sum E_{MAA}) - BSSE$$

To ensure accuracy, the **counterpoise method** was applied to correct for Basis Set Superposition Error (BSSE). This correction prevents overestimation of the binding energy caused by the overlap of basis sets used to approximate the molecular wavefunctions, a common issue in DFT calculations.

3. **Inclusion of Solvent Effects:** the influence of the solvent environment was incorporated using the Integral Equation Formalism Polarizable Continuum Model (IEFPCM) to mimic the dielectric properties of the solvent, DMSO in this case. The optimized geometry obtained in vacuum was recalculated in the solvent environment to account for the screening effects of the solvent on the interactions. Binding energy calculations were done with BSSE correction.

4. **Molar Ratio Determination**: the above process is repeated for different molar ratios of OTC:MAA. In this case: 1:4, 1:5, 1:6 and 1:7.

Finally, the binding energies obtained for each ratio are then compared, and the optimal ratio is selected.

Chapter 5

Electrodeposited MIPs

The work presented in this chapter was done during a six-month internship as a visiting student in Prof. Tsuyoshi Minami's group at the Institute of Industrial Science, University of Tokyo. During these months I had the opportunity to adapt their well-established protocol in functionalizing electrodes with electrochemical deposition of MIP to the template molecule of interest in my thesis. The lab provided all the equipment and materials used in the following work.

Electropolymerization is a highly effective approach for forming polymer films directly on electrode surfaces, particularly advantageous for developing electrochemical sensors. This technique provides control on the thickness and structure of the resulting film, by adjusting polymerization conditions, such as applied voltage or the number of cyclic scans [123]. Nevertheless, its versatility is restricted by the narrow selection of functional monomers suitable for this method [34].

The work focused on the fabrication of electrodeposited Oxytetracycline-imprinted polymer. Indeed, OTC was used as the template molecule to maintain consistency with the general focus of the thesis. This approach highlights the potential of MIPs created via electropolymerization for sensing applications, where the ability to integrate MIP with electronic components is crucial.

O-phenylenediamine (OPD) (Figure 66) was selected as the monomer due to its widespread use and suitability for electropolymerization in sensor applications[124][125]. Its ability to form uniform and thin polymer films under mild electrochemical conditions makes it particularly advantageous for creating MIP-based electrochemical sensors or in general to obtain MIP-functionalized electrodes [89].

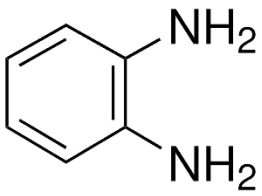

Figure 66: o-Phenylenediamine chemical structure.

The electropolymerization of MIP follows the basic principle of non-covalent imprinting, described in the previous chapters. Firstly, OTC and OPD interact in the pre-polymerization mixture, through non-covalent interactions [126]. When a potential is applied to the working electrode, the monomer undergoes an electrochemical reaction, initiating its polymerization and leading to the deposition of a polymer film on the electrode surface. During this process, the template molecule is essentially trapped within the growing polymer matrix. After the polymerization is complete, the template is removed by washing with a suitable solvent. This extraction leaves behind cavities in the polymer that are complementary in size, shape, and functionality to the template molecule, enabling the MIP to selectively recognize and bind the template.

In the next sections, the design and fabrication of a MIP-functionalized electrode are described.

5.1 DFT calculations

The initial step involved using DFT calculations to evaluate whether the interaction between the template and the functional monomer was sufficiently strong, as this aspect is not well-established in the literature. The same methodology previously described (Section 3.2.2) was used to evaluate the Binding Energy of the interaction between the Oxytetracycline and o-phenylenediamine.

The DFT calculation (at the B3LYP(D3BJ)/def2SVP level) for OTC and OPD was performed for four different molar ratios and resulted in the binding energies displayed in Table 10.

Table 10: Binding energy calculated at different molar ratios of OTC and OPD.

OTC: OPD	1:3	1:4	1:5	1:6
Binding Energy [kcal/mol] (BSSE Corrected)	-62,28	-81,98	-96,02	-102,99

Given both the results of the calculations and the previous works of Minami et al. [127][128], the selected molar ratio for further fabrication was 1:5, which displayed a satisfactory binding strength. The optimized geometry of the complex is shown in Figure 67.

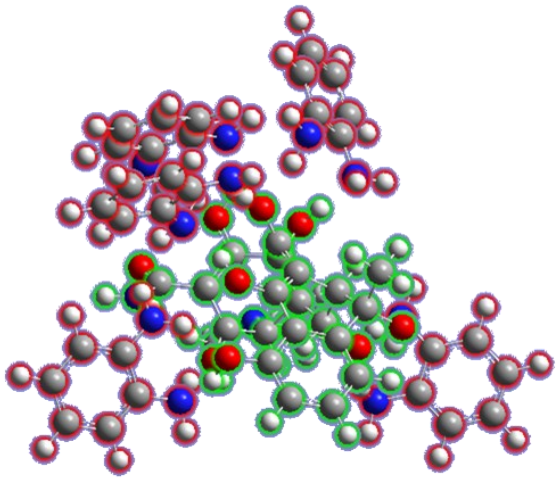

Figure 67: The preorganized structure of Oxytetracycline (highlighted in green) and O-phenylenediamine (highlighted in red) at the 1:5 molar ratio optimized by DFT calculation at the B3LYP(D3BJ)/def2SVP level.

5.2 Fabrication Process for Electrodeposited MIPs

Firstly, the gold electrode was created by thermal deposition on a PEN film, with a thickness of 100 nm and an area of 15 mm². Then, the electrode surface was modified by depositing a **gold nanostructure** (AuNS) using chronoamperometry (CA), within a three-electrode electrochemical setup (Ag/AgCl reference electrode and a Pt wire counter electrode). This electrochemical deposition process was performed in a 100 mM $HAuCl_4$ solution at a potential of −0.1 V for 60 seconds.

The nanostructure enhances the effective surface area of the electrode, which can improve the sensitivity and performance of the MIP layer, and enhance the adhesion of the polymer layer on the gold [128]. The resulting nanostructure is shown in Figure 68.

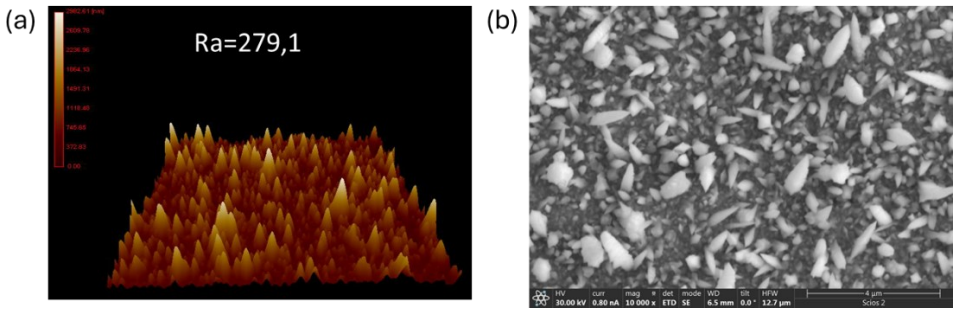

Figure 68: Characterizations of the nanostructured gold electrode by (a) AFM and (b) SEM.

The MIP formulation was prepared by mixing the template molecule (OTC), and the functional monomer (OPD), at the optimized molar ratio 1:5. To improve the dispersion of the template molecule within the solution, DMSO was added in a small quantity (500 µl per 15 ml of solution). The solution was stirred thoroughly to ensure a homogeneous mixture, which is crucial for uniform polymerization and optimal imprinting during electrodeposition.

The MIP layer was deposited on the gold nanostructured electrode surface using cyclic voltammetry (CV). Applying a cyclic potential to the electrode, this technique induces polymerization of the functional monomer and forms a thin, adherent polymer layer on the electrode surface. The **electrochemical polymerization** was performed in an acetate buffer solution (100 mM) at pH 5.2 and 25 °C, with a potential range from 0.0 to +0.8 V, a scan rate of 75 mV/s, and 20 cycles. For the fabrication of the NIP membrane, the same procedure was followed, except OTC was omitted from the solution.

The cyclic voltammetry plot in Figure 69 displays the changes in the peak currents of the electrode during the electrochemical polymerization of the MIP. The distinct peak at 0.35 V denotes the irreversible oxidation of OPD [129]. The progressive decrease in peak currents with increasing scan cycles indicates that the electrode surface was being gradually coated with a non-conductive polymer layer [130].

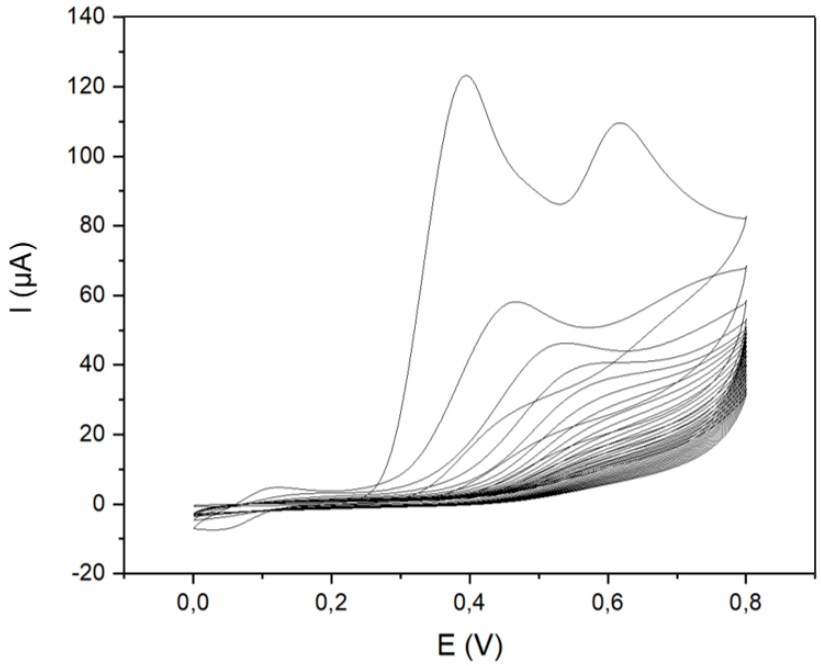

Figure 69: Deposition of the MIP membrane on the surface of the AuNS electrode by cyclic voltammetry

Following polymerization, the template molecule (OTC) was removed from the MIP layer to create the molecular recognition sites. This was achieved by incubating the electrode in a methanol:acetic acid solution (9:1) while gently stirring.

5.3 DPV Measurements: Results and Discussion

Each step of the fabrication and the following rebinding experiment were characterized through a specific electroanalytical technique, namely **Differential Pulse Voltammetry** (DPV). DPV was performed in a three-electrode setup: the working electrode coated by the MIP layer, Ag/AgCl reference electrode, and a platinum wire counter electrode. The electrolyte solution contains potassium ferricyanide ($K_3Fe(CN)_6$, 5 mM) and potassium chloride (KCl, 100 mM). Potassium ferricyanide acts as an electrochemical probe by providing redox-active species, which serves as the electron transfer mediator.

In DPV, a sequence of voltage pulses is superimposed on a linearly increasing baseline potential. During each pulse, the current is measured twice: just before the start and at the end of the pulse. The difference between these current measurements is recorded, effectively minimizing the contribution of capacitive currents and

enhancing the signal associated with faradaic processes [131]. This approach yields a voltammogram where the peak current corresponds to the reaction of the redox-active species.

When the potassium ferricyanide is used as redox probe, the applied potential drives the oxidation or reduction of the ion pair near the electrode surface [132] :

$$[Fe(CN)_6]^{3-} + e^- \leftrightarrow [Fe(CN)_6]^{4-}$$

This reaction involves the transfer of an electron between the redox species and the electrode. The applied pulse temporarily creates conditions favourable for this electron transfer, and the resulting current is recorded. The magnitude of the current is proportional to the number of electrons transferred during the reaction, which depends on the accessibility of the redox species to the electrode surface. In the case of an electrode coated with the MIP, the ability of the ion pair to reach the electrode depends on the permeability of the MIP film (Figure 70). This makes DPV a powerful tool for evaluating the selectivity and binding properties of MIP coatings.

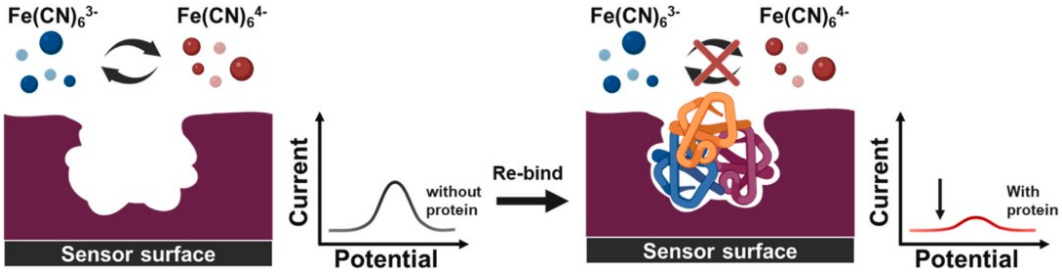

Figure 70: Scheme of the mechanism of MIP-based electrochemical sensor, reprint from [133].

Let's examine how this is applied in a practical experiment. The process is schematically described step by step in Figure 71(a), while the corresponding DPV measures of a successful experiment are in Figure 71(b):

(1) The measure is first performed on bare gold.
(2) The current peak has its maximum after the nanostructuring of the electrode.
(3) When the MIP membrane is deposited, the current drops to zero, due to the formation of an insulating layer between the electrode and the electrolyte, that interrupts the electron transfer of the $[Fe(CN)_6]^{3-}/[Fe(CN)_6]^{4-}$ ion pair on the electrode surface.
(4) The sample is washed. The emptying of the imprinted cavities allows again the approach of ions $[Fe\ (CN)_6]^{3-/4-}$ to the electrode, through the membrane.

(5) The rebinding takes place by incubating the electrode into solutions spiked with increasing concentrations of the target (OTC), and checking each step with the DPV measure. During the incubation with the target analyte, the rebinding of the OTC into the imprinted cavities causes again a progressive obstruction to the ions. Essentially, the fact that the charge exchange becomes more and more difficult (reflected by the decrease in the current) reveals the effective binding of OTC with the MIP.

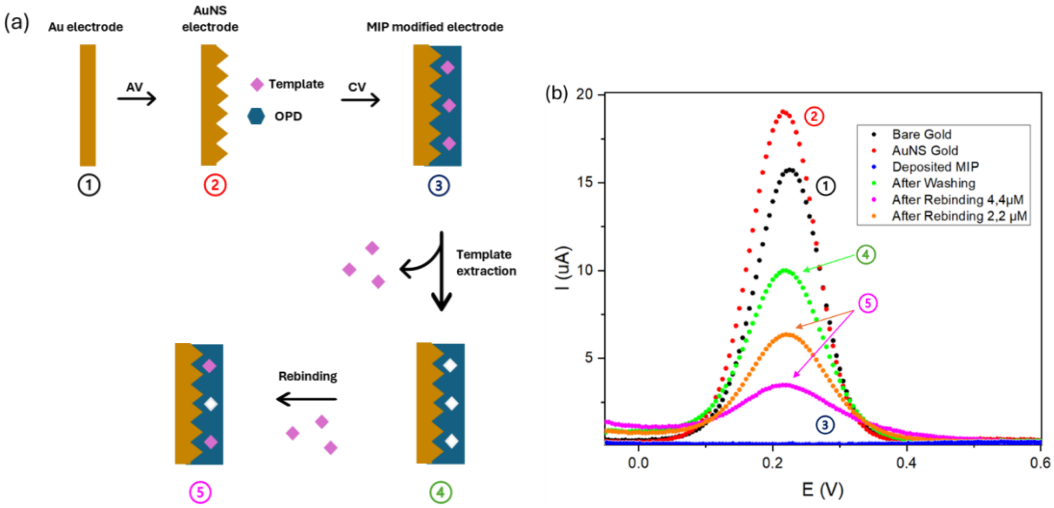

Figure 71: (a) Schematic description of the fabrication step of a MIP-based electrode, and (b) the corresponding DPV measures.

After this positive experiment, MIP and NIP electrodes were tested under similar experimental conditions. As illustrated in Figure 72, the current curves for the MIP electrode progressively decreased with increasing OTC concentrations, indicating a clear response to the target analyte. In contrast, the NIP electrode showed minimal to no response to OTC, highlighting the specificity of the MIP for the target molecule. This underscores the selective binding capability of the MIP electrode.

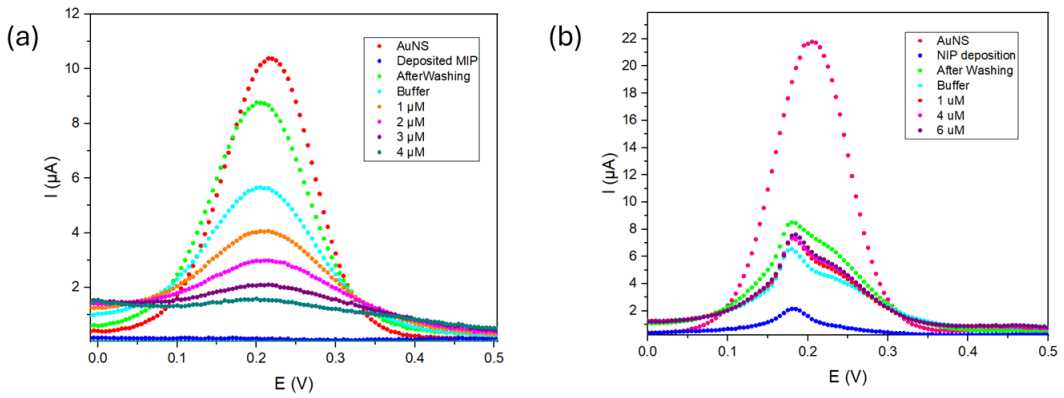

Figure 72: DPV results of the MIP (a) and NIP (b) functionalized electrodes, upon increasing concentration of OTC.

Such different behaviour is particularly clear in the graph shown in Figure 73, where the normalized difference between the peak current after incubation with increasing analyte concentrations (I_p) and the initial peak current before incubation (I_{p0}) is shown.

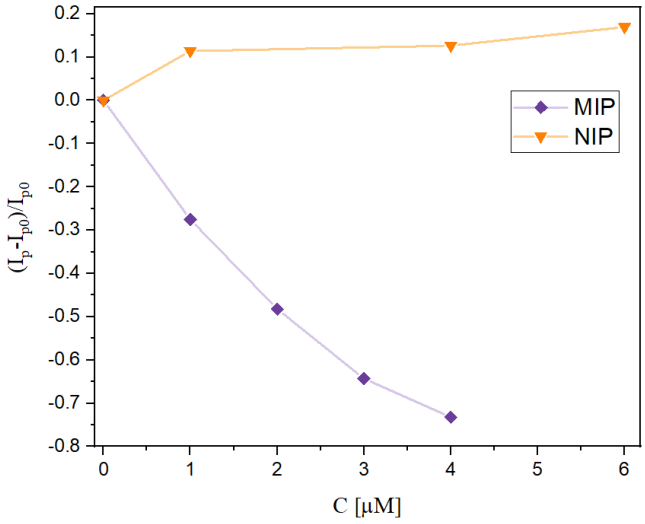

Figure 73: The difference between the peak current after incubation (I_p) and the initial peak current before incubation (I_{p0}) is plotted as a function of analyte concentration. The data highlights the distinct response of the MIP electrode, which shows a progressive decrease in normalized peak current with increasing analyte concentration, compared to the NIP electrode, which exhibits minimal change.

Regarding the small peak present in the DPV of the NIP electrode (Figure 72(b)), it may be caused by a non-perfectly uniform deposition of the polymer layer, with portions of the underlying gold electrode exposed. These exposed areas can allow the redox activity of ferrocyanide, potentially resulting in the appearance of a small peak in the voltametric measurements.

After further investigations, it was observed that the sensitivity range and saturation point varied among electrodes, even when fabricated using the same procedure. In Figure 74, the DPVs obtained from two separate experiments are presented. In these experiments, smaller analyte concentrations were tested to study sensitivity.

In both cases, signal saturation—indicated by the absence of further decreases in the curve despite increasing analyte concentrations—occurred around 0.6–0.8 µM. This contrasts with the previous experiment, shown in Figure 72(a), where the electrode continued to detect concentrations up to 4 µM. These discrepancies in rebinding ranges and saturation points are likely attributable to limited reproducibility in the fabrication of the MIP electrode.

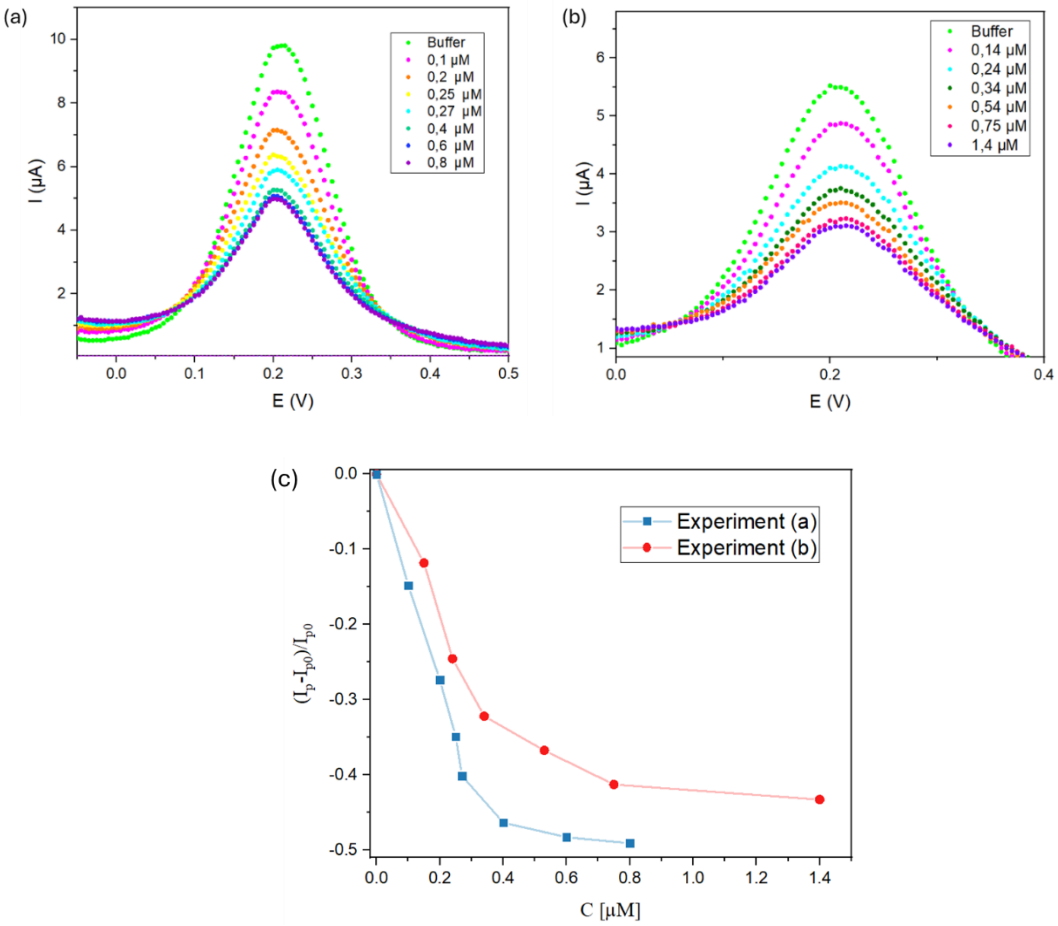

Figure 74: (a) and (b) DPV results of two experiments with increasing analyte concentration, and corresponding plot of the peak currents.

5.4 Conclusions and Future Applications

This chapter focused on the fabrication and testing of MIP-modified electrodes and their ability to selectively detect the target analyte. The results demonstrated the potential of these electrodes to achieve analyte-specific binding, as evident from the distinct response of MIP-modified electrodes compared to their NIP counterparts.

However, some limitations and challenges were identified, which need to be addressed to optimize performance and ensure reliable application. One key finding was the limited reproducibility of the fabricated electrodes. A possible explanation could be the variations in the electrode surface, likely caused by the non-perfectly reproducibility of the deposition of gold nanostructures. An illustrative example of two electrodes with consistently different surface characteristics is provided in Figure 75.

An additional explanation may be that the polymer layer results thinner than the sharp nanostructures, and thus the exposed imprinted area varies between electrodes, leading to inconsistent binding.

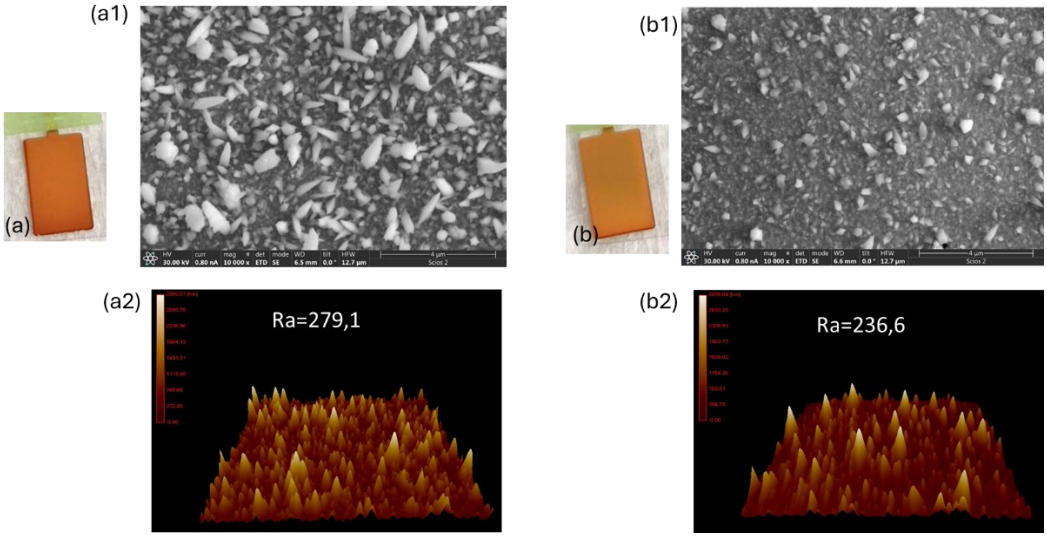

Figure 75: Pictures of two distinct electrodes (a) and (b), and their SEM and AFM characterizations, respectively (a1), (b1) and (a2), (b2).

Therefore, while the nanostructured surface offers advantages, these may be outweighed by the drawbacks of a non-uniform surface, leading to inconsistent binding sites and, consequently, non-uniform sensor performance.

Additionally, it was observed that the storage time of the fabricated electrodes was a critical factor. After a few inconsistent attempts, it became clear that the electrodes must be tested for rebinding within a day or two after fabrication to avoid performance degradation. This highlights a significant limitation in their practical applicability, as long-term stability and usability are essential for real-world sensor deployment.

Despite these challenges, the electrodes showed promise for future integration into transistor-based sensor systems, as demonstrated by Prof. Minami's work, where the MIP-based electrode was successfully integrated as the gate electrode in an Organic-Field Effect Transistor (Figure 76). Such systems could enhance the sensitivity of analyte detection, paving the way for applications in environmental and biomedical monitoring.

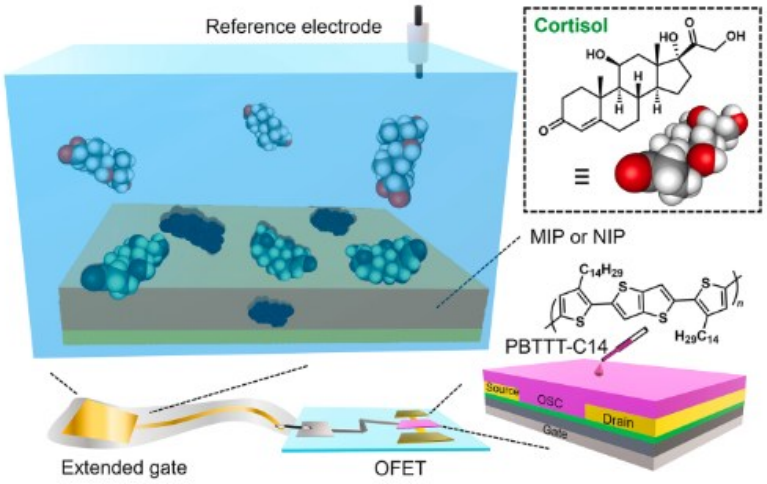

Figure 76: Conceptual demonstration of the extended-gate OFET functionalized with the MIP membrane for the detection of cortisol, reprint from Minami et al. work [127].

Future efforts should focus on improving the reproducibility of the electrode fabrication process and extending the storage stability of the electrodes. Once a stable and reliable electrode fabrication process is established, the next step will be to implement these electrodes in transistor-based sensing platforms following a similar approach to Minami's work. This would open possibilities for real-world applications in analytical sensing of the electrodeposited MIPs.

Chapter 6

General Conclusions

This thesis represents a significant step forward in the integration of Digital Light Processing 3D printing with Molecular Imprinting Technology, showcasing its potential in developing innovative materials for environmental remediation and sensing applications. By fabricating macroscopic, self-standing MIP structures tailored for the selective removal of antibiotics from water, this work bridges molecular recognition principles with advanced manufacturing techniques. The experimental findings provide valuable insights into the formulation, optimization, and performance of 3D-printed MIPs, while also identifying critical challenges that need to be addressed for their practical application.

The results demonstrate that 3D-printed MIPs can selectively capture Oxytetracycline from aqueous solutions, with binding performance influenced by factors such as polymer composition, structural design, and surface area. The use of computational modelling through Density Functional Theory played a crucial role in optimizing the interactions between the template and functional monomer, ensuring an effective molecular imprinting process. Furthermore, the fabrication of complex geometries, such as gyroids, revealed the potential of structural optimization in enhancing binding efficiency by increasing accessible surface area and improving mass transfer.

Despite these promising findings, key challenges emerged throughout the research. Reproducibility remained a limiting factor, as variations in polymerization conditions and fabrication parameters influenced binding performance.

Additionally, the structural integrity of the printed MIPs posed a significant barrier to their reusability, as repeated solvent exposure led to degradation and reduced efficiency over multiple cycles. Future work should focus on improving the mechanical and chemical resistance of the polymer matrix to enhance durability and enable multiple reuse cycles.

Another important avenue for future research is the introduction of controlled porosity within the printed structures. The findings suggest that molecular recognition predominantly occurs at the surface of the MIPs, indicating that internal porosity could enhance analyte diffusion and improve overall binding capacity. Strategies such as salt-leaching or emulsion templating should be explored to fabricate porous MIPs while maintaining structural integrity.

Beyond environmental remediation, this work also explored the application of MIPs in electrochemical sensing through the fabrication of electrodeposited MIPs for potential integration into sensor platforms. These electrodes demonstrated selectivity toward OTC, highlighting the versatility of MIPs in analytical applications. However, challenges in reproducibility and stability were observed, largely due to variations in the electrode surface and polymer film thickness. Future efforts should focus on refining the electrode fabrication process and improving storage stability to ensure reliable sensor performance. Ultimately, these electrodes could be integrated into transistor-based sensors, as demonstrated in previous works, expanding their applicability to biomedical and environmental monitoring.

Overall, this research highlights the potential of advanced fabrication strategies for developing innovative MIP-based materials, paving the way for their broader application in environmental remediation, sensing, and other high-impact technological fields.

Bibliography

[1] P.S. Agutter, D.N. Wheatley, About Life: Concepts in Modern Biology, 1st ed., Springer Dordrecht, 2007. https://doi.org/https://doi.org/10.1007/978-1-4020-5418-1.

[2] E. Persch, O. Dumele, F. Diederich, Molecular Recognition in Chemical and Biological Systems, Angew. Chemie Int. Ed. (2015) 3290–3327. https://doi.org/10.1002/anie.201408487.

[3] P.C. Mariju, J. Navarro, From Molecular Recognition to the " Vehicles " of Evolutionary Complexity : An Informational Approach, Int. J. Mol. Sci. 22 (2021) 11965. https://doi.org/https://doi.org/10.3390/ ijms222111965.

[4] O.I. Parisi, F. Francomano, M. Dattilo, F. Patitucci, S. Prete, F. Amone, F. Puoci, The Evolution of Molecular Recognition: From Antibodies to Molecularly Imprinted Polymers (MIPs) as Artificial Counterpart, J. Funct. Biomater. 13 (2022). https://doi.org/10.3390/jfb13010012.

[5] B. Chen, S. Piletsky, A.P.F. Turner, Molecular recognition: Design of "keys," Comb. Chem. High Throughput Screen. 5 (2002) 409–427.

[6] J. Manhas, H.I. Eldestein, J.N. Leonard, L. Morsut, The evolution of synthetic receptor systems, Nat. Chem. Biol. 18 (2022) 244–255. https://doi.org/https://doi.org/10.1038/s41589-021-00926-z.

[7] R.M. Lequin, Enzyme Immunoassay (EIA)/ Enzyme-Linked Immunosorbent Assay (ELISA), 2418 (2005) 2415–2418. https://doi.org/10.1373/clinchem.2005.051532.

[8] L. Lunelli, F. Barbaresco, G. Scordo, C. Potrich, L. Vanzetti, S.L. Marasso, M. Cocuzza, C.F. Pirri, C. Pederzolli, PDMS-based microdevices for the

capture of MicroRNA biomarkers, Appl. Sci. 10 (2020). https://doi.org/10.3390/app10113867.

[9] M. Barra, G. Tomaiuolo, V.R. Villella, S. Esposito, A. Liboà, P. D'Angelo, S.L. Marasso, M. Cocuzza, V. Bertana, E. Camilli, V. Preziosi, Organic Electrochemical Transistor Immuno-Sensors for Spike Protein Early Detection, Biosensors 13 (2023). https://doi.org/10.3390/bios13070739.

[10] V. Preziosi, M. Barra, V.R. Villella, S. Esposito, P. D'Angelo, S.L. Marasso, M. Cocuzza, A. Cassinese, S. Guido, Immuno-Sensing at Ultra-Low Concentration of TG2 Protein by Organic Electrochemical Transistors, Biosensors 13 (2023). https://doi.org/10.3390/bios13040448.

[11] M. Segantini, M. Parmeggiani, A. Ballesio, G. Palmara, F. Frascella, S.L. Marasso, M. Cocuzza, Design of a Portable Microfluidic Platform for EGOT-Based in Liquid Biosensing, Sensors 22 (2022) 1–15. https://doi.org/10.3390/s22030969.

[12] M.J. Whitcombe, I. Chianella, L. Larcombe, S.A. Piletsky, J. Noble, R. Porter, A. Horgan, The rational development of molecularly imprinted polymer-based sensors for protein detection, Chem. Soc. Rev. 40 (2011) 1547–1571. https://doi.org/10.1039/c0cs00049c.

[13] K. Haupt, A. V Linares, M. Bompart, B.T.S. Bui, Molecularly Imprinted Polymers, Top Curr Chem 325 (2012) 1–28. https://doi.org/10.1007/128_2011_307.

[14] G. Ertürk, B. Mattiasson, Molecular imprinting techniques used for the preparation of biosensors, Sensors (Switzerland) 17 (2017) 1–17. https://doi.org/10.3390/s17020288.

[15] M. V. Polyakov, Adsorption properties and structure of silica gel, Zhurnal Fizieskoj Khimii/Akademiya SSSR 2 (1931) 799–805.

[16] G. Wulff, A. Sahran, The use of polymers with enzyme-analogous structures for the resolution of racemates, Angew. Chemie Int. Ed. English 46 (1972) 334–342. https://doi.org/10.1002/anie.197203341.

[17] T. Takagishi, I.M. Klotz, Macromolecule-small molecule interactions; introduction of additional binding sites in polyethyleneimine by disulfide cross–linkages, Biopolymers 11 (1972) 483–491. https://doi.org/10.1002/bip.1972.360110213.

[18] R. Arshady, K. Mosbach, Synthesis of Substrate-selective Polymers by Host-Guest Polymerization, Makromol. Chem. 182 (1981) 687–692.

[19] R. Rezanavaz, M. Petcu, M.-J. Le Guen, A. Dubois, Three-Dimensional Printing of Molecularly Imprinted Polymers by Digital Light Processing for Copper Ion Sequestration, 3D Print. Addit. Manuf. (2022). https://doi.org/10.1089/3dp.2022.0107.

[20] S. Akgönüllü, S. Kılıç, C. Esen, A. Denizli, Molecularly Imprinted Polymer-Based Sensors for Protein Detection, Polymers (Basel). 15 (2023). https://doi.org/10.3390/polym15030629.

[21] M. Antipchik, J. Reut, A. Öpik, V. Syritski, MIP-based electrochemical sensor for direct detection of Hepatitis C virus via E2 envelope protein, Talanta 250 (2022) 123737. https://doi.org/https://doi.org/10.1016/j.talanta.2022.123737.

[22] S. Piletsky, F. Canfarotta, A. Poma, A.M. Bossi, Molecularly Imprinted Polymers for Cell Recognition, Trends Biotechnol. 38 (2020) 368–387. https://doi.org/10.1016/j.tibtech.2019.10.002.

[23] D.A. Spivak, Optimization, evaluation, and characterization of molecularly imprinted polymers, Adv. Drug Deliv. Rev. 57 (2005) 1779–1794. https://doi.org/10.1016/j.addr.2005.07.012.

[24] T. Sajini, B. Mathew, A brief overview of molecularly imprinted polymers: Highlighting computational design, nano and photo-responsive imprinting, Talanta Open 4 (2021) 100072. https://doi.org/10.1016/j.talo.2021.100072.

[25] H. Yang, H.B. Liu, Z.S. Tang, Z.D. Qiu, H.X. Zhu, Z.X. Song, A.L. Jia, Synthesis, performance, and application of molecularly imprinted membranes: A review, J. Environ. Chem. Eng. 9 (2021) 106352. https://doi.org/10.1016/j.jece.2021.106352.

[26] A. Bossi, S.A. Piletsky, E. V Piletska, P.G. Righetti, A.P.F. Turner, Surface-Grafted Molecularly Imprinted Polymers for Protein Recognition, 73 (2001) 5281–5286.

[27] R.A. Lorenzo, A.M. Carro, C. Alvarez-Lorenzo, A. Concheiro, To remove or not to remove? The challenge of extracting the template to make the cavities available in molecularly imprinted polymers (MIPs), Int. J. Mol. Sci. 12 (2011) 4327–4347. https://doi.org/10.3390/ijms12074327.

[28] Y.P. Song, L. Zhang, G.N. Wang, J.X. Liu, J. Liu, J.P. Wang, Dual-dummy-template molecularly imprinted polymer combining ultra performance liquid chromatography for determination of fluoroquinolones and sulfonamides in pork and chicken muscle, Food Control 82 (2017) 233–242.

[29] F. Bates, Design and development of molecularly imprinted polymers and imprinted sensors, Univ. Autònoma Barcelona. Dep. Química. (2016) 1–258.

[30] L. Chen, X. Wang, W. Lu, X. Wu, J. Li, Molecular imprinting: Perspectives and applications, Chem. Soc. Rev. 45 (2016) 2137–2211. https://doi.org/10.1039/c6cs00061d.

[31] E. Mohsenzadeh, V. Ratautaite, E. Brazys, S. Ramanavicius, S. Zukauskas, D. Plausinaitis, A. Ramanavicius, Application of computational methods in the design of molecularly imprinted polymers (review), TrAC - Trends Anal. Chem. Anal. Chem. 171 (2024) 117480. https://doi.org/https://doi.org/10.1016/j.trac.2023.117480.

[32] N. Murdaya, A.L. Triadenda, D. Rahayu, A.N. Hasanah, A Review: Using Multiple Templates for Molecular Imprinted Polymer: Is It Good?, Polymers (Basel). 14 (2022) 1–22. https://doi.org/10.3390/polym14204441.

[33] A. Anene, R. Kalfat, Y. Chevalier, S. Hbaieb, Design of Molecularly Imprinted Polymeric Materials: The Crucial Choice of Functional Monomers, Chem. Africa 3 (2020) 769–781. https://doi.org/10.1007/s42250-020-00180-1.

[34] E. Paruli, O. Soppera, K. Haupt, C. Gonzato, Photopolymerization and Photostructuring of Molecularly Imprinted Polymers, ACS Appl. Polym. Mater. 3 (2021) 4769–4790. https://doi.org/10.1021/acsapm.1c00661.

[35] Y.-W. Tang, G.-Z. Fang, S. Wang, J.-L. Li, Covalent imprinted polymer for selective and rapid enrichment of ractopamine by a noncovalent approach, Anal. Bioanal. Chem. 401 (2011) 2275–2282. https://doi.org/doi:10.1007/s00216-011-5280-0.

[36] M. Dinc, C. Esen, B. Mizaikoff, Recent advances on core e shell magnetic molecularly imprinted polymers for biomacromolecules, Trends Anal. Chem. 114 (2019) 202–217. https://doi.org/10.1016/j.trac.2019.03.008.

[37] M. Mabrouk, S.F. Hammad, A.A. Abdella, F.R. Mansour, Tips and tricks for successful preparation of molecularly imprinted polymers for analytical applications: A critical review, Microchem. J. 193 (2023) 109152. https://doi.org/10.1016/j.microc.2023.109152.

[38] R.J. Umpleby, S.C. Baxter, Y. Chen, R.N. Shah, K.D. Shimizu, Characterization of molecularly imprinted polymers with the Langmuir - Freundlich isotherm, Anal. Chem. 73 (2001) 4584–4591. https://doi.org/10.1021/ac0105686.

[39] A.J. Richard, Characterization of the binding properties of molecularly imprinted polymers, 2015.

[40] S.A. Piletsky, E. V. Piletska, K. Karim, K.W. Freebairn, C.H. Legge, A.P.F. Turner, Polymer Cookery: Influence of Polymerization Conditions on the Performance of Molecularly Imprinted Polymers, Macromoleules 35 (2002) 7499–7504. https://doi.org/10.1021/acs.langmuir.6b00554.

[41] S. Beyazit, B. Tse Sum Bui, K. Haupt, C. Gonzato, Molecularly imprinted polymer nanomaterials and nanocomposites by controlled/living radical polymerization, Prog. Polym. Sci. 62 (2016) 1–21. https://doi.org/10.1016/j.progpolymsci.2016.04.001.

[42] M. Bompart, K. Haupt, Molecularly imprinted polymers and controlled/living radical polymerization, Aust. J. Chem. 62 (2009) 751–761. https://doi.org/10.1071/CH09124.

[43] A. Spangenberg, L. Chia Gomez, J.-P. Malval, O. Soppera, Y. Fuchs, X.A. Ton, K. Haupt, Preparation of Molecularly Imprinted Polymers by Two-Photon Stereolithography, EP3112021A1, 2017.

[44] L. Ye, K. Mosbach, Molecularly imprinted microspheres as antibody binding mimics, React. Funct. Polym. 48 (2001) 149–157. https://doi.org/10.1016/S1381-5148(01)00050-5.

[45] L. Chen, S. Xu, J. Li, Recent advances in molecular imprinting technology: Current status, challenges and highlighted applications, Chem. Soc. Rev. 40 (2011) 2922–2942. https://doi.org/10.1039/c0cs00084a.

[46] R.M. Roland, S.A. Bhawani, M.N.M. Ibrahim, Synthesis of molecularly imprinted polymer by precipitation polymerization for the removal of ametryn, BMC Chem. (2023) 1–20. https://doi.org/10.1186/s13065-023-01084-0.

[47] D. Xiao, Y. Jiang, Y. Bi, Molecularly imprinted polymers for the detection of illegal drugs and additives: a review, Microchim. Acta 185 (2018). https://doi.org/10.1007/s00604-018-2735-4.

[48] A.G. Mayes, K. Mosbach, Molecularly imprinted polymer beads: suspension polymerization using a liquid perfluorocarbon as the dispersing phase, Anal. Chem. 68 (1996) 3769–3764. https://doi.org/10.1021/ac960363a.

[49] L. Geng, X. Kou, J. Lei, H. Su, G. Ma, Z. Su, Preparation , characterization and adsorption performance of molecularly imprinted microspheres for erythromycin using suspension polymerization, J. Chem. Technol.

Biotechnol. 87 (2011) 635–642. https://doi.org/10.1002/jctb.2757.

[50] G. Zhao, J. Liu, M. Liu, X. Han, Y. Peng, X. Tian, Synthesis of Molecularly Imprinted Polymer via Emulsion Polymerization for Application in Solanesol Separation, Appl. Sci. 10 (2020) 2068. https://doi.org/doi:10.3390/app10082868.

[51] D. Bitas, V. Samanidou, Molecularly imprinted polymers as extracting media for the chromatographic determination of antibiotics in milk, Molecules 23 (2018) 4–6. https://doi.org/10.3390/molecules23020316.

[52] L. Wan, Z. Chen, C. Huang, X. Shen, Core-shell molecularly imprinted particles, Trends Anal. Chem. 95 (2017) 110–121. https://doi.org/10.1016/j.trac.2017.08.010.

[53] S. Ramanavičius, I. Morkvėnaitė-vilkončienė, U. Samukaitė-bubnienė, V. Ratautaitė, I. Plikusienė, R. Viter, A. Ramanavičius, Electrochemically Deposited Molecularly Imprinted Polymer-Based Sensors, Sensors 22 (2022). https://doi.org/10.3390/s22031282.

[54] A.-M. Gavrilă, E.-B. Stoica, T.-V. Iordache, A. Sârbu, Modern and Dedicated Methods for Producing Molecularly Imprinted Polymer Layers in Sensing Applications, Appl. Sci. 12 (2022) 3080. https://doi.org/10.3390/app12063080.

[55] C. Dong, H. Shi, Y. Han, Y. Yang, R. Wang, J. Men, Molecularly imprinted polymers by the surface imprinting technique, Eur. Polym. J. 145 (2021) 110231. https://doi.org/10.1016/j.eurpolymj.2020.110231.

[56] L.P.C. Gomez, A. Spangenberg, X.A. Ton, Y. Fuchs, F. Bokeloh, J.P. Malval, B. Tse Sum Bui, D. Thuau, C. Ayela, K. Haupt, O. Soppera, Rapid Prototyping of Chemical Microsensors Based on Molecularly Imprinted Polymers Synthesized by Two-Photon Stereolithography, Adv. Mater. 28 (2016) 5931–5937. https://doi.org/10.1002/adma.201600218.

[57] B. Keitel, A.D. Batista, S. Schimana, B. Mizaikoff, M. Dinc, Emulsion-Free 3D Printing of Inherently Porous Molecularly Imprinted Polymers with Tailored Macroscopic Geometries, ACS Appl. Polym. Mater. 6 (2024) 3690–3695. https://doi.org/10.1021/acsapm.3c02744.

[58] G. Gonzalez, I. Roppolo, C.F. Pirri, A. Chiappone, Current and emerging trends in polymeric 3D printed microfluidic devices, Addit. Manuf. 55 (2022) 102867. https://doi.org/10.1016/j.addma.2022.102867.

[59] A. Salas, M. Zanatta, V. Sans, I. Roppolo, Chemistry in light-induced 3D

printing, ChemTexts 9 (2023) 1–16. https://doi.org/10.1007/s40828-022-00176-z.

[60] M. Caprioli, I. Roppolo, A. Chiappone, L. Larush, C.F. Pirri, S. Magdassi, 3D-printed self-healing hydrogels via Digital Light Processing, Nat. Commun. 12 (2021) 1–10. https://doi.org/10.1038/s41467-021-22802-z.

[61] S. Bae, B. Kim, Effects of Cellulose Nanocrystal and Inorganic Nanofillers on the Morphological and Mechanical Properties of Digital Light Processing (DLP) 3D-Printed Photopolymer Composites, Appl. Sci. 11 (2021) 6835. https://doi.org/10.3390/app11156835.

[62] Z. Dai, J. Liu, S. Tang, Y. Wang, Y. Wang, R. Jin, Optimization of enrofloxacin-imprinted polymers by computer-aided design, J. Mol. Model. 21 (2015) 290. https://doi.org/10.1007/s00894-015-2836-5.

[63] L. Xie, N. Xiao, L. Li, X. Xie, Y. Li, Theoretical Insight into the Interaction between Chloramphenicol and Functional Monomer (Methacrylic Acid) in Molecularly Imprinted Polymers, Int. J. Mol. Sci. 21 (2020) 4193. https://doi.org/10.3390/ijms21114139.

[64] R. Rodríguez-Dorado, A.M. Carro, I. Chianella, K. Karim, A. Concheiro, R.A. Lorenzo, S. Piletsky, C. Alvarez-Lorenzo, Oxytetracycline recovery from aqueous media using computationally designed molecularly imprinted polymers, Anal. Bioanal. Chem. 408 (2016) 6845–6856. https://doi.org/10.1007/s00216-016-9811-6.

[65] I. Tsyrulneva, O. Zaporozhets, E. Piletska, S. Piletsky, Molecular modelling and synthesis of a polymer for the extraction of amiloride and triamterene from human urine, Anal. Methods 6 (2014) 3429–3435. https://doi.org/10.1039/c4ay00318g.

[66] B.C.G. Karlsson, J. O'Mahony, J.G. Karlsson, H. Bengtsson, L.A. Eriksson, I.A. Nicholls, Structure and dynamics of monomer-template complexation: An explanation for molecularly imprinted polymer recognition site heterogeneity, J. Am. Chem. Soc. 131 (2009) 13297–13304. https://doi.org/10.1021/ja902087t.

[67] S. Suryana, Mutakin, Y. Rosandi, A.N. Hasanah, An update on molecularly imprinted polymer design through a computational approach to produce molecular recognition material with enhanced analytical performance, Molecules 26 (2021). https://doi.org/10.3390/molecules26071891.

[68] M. Bitar, E. Bou-Maroun, A. Lerbret, N. Ouaini, P. Cayot, Binding characteristics of molecularly imprinted polymers based on fungicides in

hydroalcoholic media, J. Sep. Sci. 38 (2015) 3607–3614. https://doi.org/10.1002/jssc.201500543.

[69] T. Cowen, K. Karim, S. Piletsky, Computational Approaches in the Design of Synthetic Receptors – A Review, Anal. Chim. Acta 936 (2016) 62–74. https://doi.org/10.1016/j.aca.2016.07.027.

[70] E. Mohsenzadeh, V. Ratautaite, E. Brazys, S. Ramanavičius, Š. Žukauskas, D. Plaušinaitis, A. Ramanavičius, Design of molecularly imprinted polymers (MIP) using computational methods: A review of strategies and approaches, WIREs Comput. Mol. Sci. 14 (2024) 1713.

[71] Y. Zhao, D.G. Truhlar, Density functional theory for reaction energies: Test of meta and hybrid meta functionals, range-separated functionals, and other high-performance functionals, J. Chem. Theory Comput. 7 (2011) 669–676. https://doi.org/10.1021/ct1006604.

[72] L. Jun-Bo, S. Yang, T. Shan-Shan, J. Rui-Fa, Theoretical and experimental research on the self-assembled system of molecularly imprinted polymers formed by salbutamol and methacrylic acid, J. Sep. Sci. 38 (2015) 1065–1071. https://doi.org/10.1002/jssc.201401309.

[73] M. Busato, R. Distefano, F. Bates, K. Karim, A.M. Bossi, J.M. López Vilariño, S. Piletsky, N. Bombieri, A. Giorgetti, MIRATE: MIps RATional dEsign Science Gateway, J. Integr. Bioinform. 15 (2018) 1–6. https://doi.org/10.1515/jib-2017-0075.

[74] J.J. Belbruno, Molecularly Imprinted Polymers, Chem. Rev. 119 (2019) 94–119. https://doi.org/10.1021/acs.chemrev.8b00171.

[75] O.K. Castell, D.A. Barrow, A.R. Kamarudin, C.J. Allender, Current practices for describing the performance of molecularly imprinted polymers can be misleading and may be hampering the development of the field, J. Mol. Recognit. 24 (2011) 1115–1122. https://doi.org/10.1002/jmr.1161.

[76] Z. Song, J. Li, W. Lu, B. Li, G. Yang, Y. Bi, M. Arabi, X. Wang, J. Ma, L. Chen, Molecularly imprinted polymers based materials and their applications in chromatographic and electrophoretic separations, Trends Anal. Chem. 146 (2022). https://doi.org/10.1016/j.trac.2021.116504.

[77] V. Pichon, K. Haupt, Affinity separations on molecularly imprinted polymers with special emphasis on solid-phase extraction, J. Liq. Chromatogr. Relat. Technol. 29 (2006) 989–1023. https://doi.org/10.1080/10826070600574739.

[78] M.I. Malik, H. Shaikh, G. Mustafa, M.I. Bhanger, Recent Applications of Molecularly Imprinted Polymers in Analytical Chemistry, Sep. Purif. Rev. 48 (2019) 179–219. https://doi.org/10.1080/15422119.2018.1457541.

[79] D. Stevenson, H.F. El-Sharif, S.M. Reddy, Selective extraction of proteins and other macromolecules from biological samples using molecular imprinted polymers, Bioanalysis 8 (2016) 2255–2263. https://doi.org/10.4155/bio-2016-0209.

[80] C.C. Villa, T.S. Leidy, G.A. Valencia, S. Ahmed, T.J. Gutiérrez, Molecularly imprinted polymers for food applications : A review, Trends Food Sci. Technol. 111 (2021) 642–669. https://doi.org/10.1016/j.tifs.2021.03.003.

[81] Y.K. Lv, J.Q. Zhang, Z.Y. Guo, W. Zhang, H.W. Sun, Determination of tetracyclines residues in egg, milk, and milk powder by online coupling of a precolumn packed with molecular imprinted hybrid composite materials to RP-HPLC-UV, J. Liq. Chromatogr. Relat. Technol. 38 (2015) 1–7. https://doi.org/10.1080/10826076.2013.873873.

[82] Z.O. Uygun, H.D. Ertugrul Uygun, N. Ermis, E. Canbay, Molecularly Imprinted Sensors — New Sensing Technologies, Biosens. - Micro Nanoscale Appl. (2015). https://doi.org/10.5772/60781.

[83] O.S. Ahmad, T.S. Bedwell, C. Esen, A. Garcia-Cruz, S.A. Piletsky, Molecularly Imprinted Polymers in Electrochemical and Optical Sensors, Trends Biotechnol. 37 (2019) 294–309. https://doi.org/10.1016/j.tibtech.2018.08.009.

[84] M.C. Moreno-Bondi, F. Navarro-Villoslada, E. Benito-Pena, J.L. Urraca, Molecularly Imprinted Polymers as Selective Recognition Elements in Optical Sensing, Curr. Anal. Chem. 4 (2008) 316–340. https://doi.org/10.2174/157341108785914925.

[85] H.D. Ertuğrul Uygun, M. Nalan Demir, The Role of Molecularly Imprinted Polymers in Sensor Technology: Electrochemical, Optical and Piezoelectric Sensor Applications, J. Turkish Chem. Soc. Sect. A Chem. 10 (2023) 1081–1098. https://doi.org/10.18596/jotcsa.1285655.

[86] A. Azizi, C.S. Bottaro, A critical review of molecularly imprinted polymers for the analysis of organic pollutants in environmental water samples, J. Chromatogr. A 1614 (2020) 460603. https://doi.org/10.1016/j.chroma.2019.460603.

[87] F.A. Amarh, A. Kangmennaa, E.S. Agorku, R.B. Voegborlo, A state-of-the-art review of trends in molecularly imprinted polymers in the clean-up of

pesticides in environmental samples, Sustain. Environ. 10 (2024). https://doi.org/10.1080/27658511.2023.2298067.

[88] T. Sergeyeva, O. Piletska, S. Piletsky, Rationally designed molecularly imprinted polymer membranes as antibody and enzyme mimics in analytical biotechnology, BBA Adv. 3 (2023) 100070. https://doi.org/10.1016/j.bbadva.2022.100070.

[89] A. Adumitrăchioaie, M. Tertiş, A. Cernat, R. Săndulescu, C. Cristea, Electrochemical methods based on molecularly imprinted polymers for drug detection. A review, Int. J. Electrochem. Sci. 13 (2018) 2556–2576. https://doi.org/10.20964/2018.03.75.

[90] K.K. Dar, S. Shao, T. Tan, Y. Lv, Molecularly imprinted polymers for the selective recognition of microorganisms, Biotechnol. Adv. 45 (2020) 107640. https://doi.org/10.1016/j.biotechadv.2020.107640.

[91] S. He, L. Zhang, S. Bai, H. Yang, Z. Cui, X. Zhang, Y. Li, Advances of molecularly imprinted polymers (MIP) and the application in drug delivery, Eur. Polym. J. 143 (2021) 110179. https://doi.org/10.1016/j.eurpolymj.2020.110179.

[92] R. Suravajhala, H.R. Burri, B. Malik, Selective Targeted Drug Delivery Mechanism via Molecular Imprinted Polymers in Cancer Therapeutics, Curr. Top. Med. Chem. 20,22 (2020) 1993–1998. https://doi.org/10.2174/1568026620666200622150710.

[93] J.W. Lowdon, H. Diliën, P. Singla, M. Peeters, T.J. Cleij, B. van Grinsven, K. Eersels, MIPs for commercial application in low-cost sensors and assays – An overview of the current status quo, Sensors Actuators, B Chem. 325 (2020). https://doi.org/10.1016/j.snb.2020.128973.

[94] Y.L. Mustafa, A. Keirouz, H.S. Leese, Molecularly imprinted polymers in diagnostics: accessing analytes in biofluids, J. Mater. Chem. B 10 (2022) 7418–7449. https://doi.org/10.1039/d2tb00703g.

[95] D.A. Gkika, A.K. Tolkou, D.A. Lambropoulou, D.N. Bikiaris, P. Kokkinos, I.K. Kalavrouziotis, G.Z. Kyzas, Application of molecularly imprinted polymers (MIPs) as environmental separation tools, RSC Appl. Polym. 2 (2024) 127–148. https://doi.org/10.1039/d3lp00203a.

[96] H.Y. Hijazi, C.S. Bottaro, Molecularly imprinted polymer thin-film as a micro-extraction adsorbent for selective determination of trace concentrations of polycyclic aromatic sulfur heterocycles in seawater, J. Chromatogr. A 1617 (2020) 460824.

https://doi.org/10.1016/j.chroma.2019.460824.

[97] J. Meléndez-Marmolejo, L. Díaz de León-Martínez, V. Galván-Romero, S. Villarreal-Lucio, R. Ocampo-Pérez, N.A. Medellín-Castillo, E. Padilla-Ortega, I. Rodríguez-Torres, R. Flores-Ramírez, Design and application of molecularly imprinted polymers for adsorption and environmental assessment of anti-inflammatory drugs in wastewater samples, Environ. Sci. Pollut. Res. 29 (2022) 45885–45902. https://doi.org/10.1007/s11356-022-19130-0.

[98] Y. Hao, R. Gao, L. Shi, D. Liu, Y. Tang, Z. Guo, Water-compatible magnetic imprinted nanoparticles served as solid-phase extraction sorbents for selective determination of trace 17beta-estradiol in environmental water samples by liquid chromatography, J. Chromatogr. A 1396 (2015) 7–16. https://doi.org/https://doi.org/10.1016/j.chroma.2015.03.083.

[99] P. Grenni, V. Ancona, A. Barra Caracciolo, Ecological effects of antibiotics on natural ecosystems: A review, Microchem. J. 136 (2018) 25–39. https://doi.org/10.1016/j.microc.2017.02.006.

[100] O.B. Jonas, A. Irwin, F.C.J. Berthe, F.G. Le Gall, P. V Marquez, Drug-resistant infections : a threat to our economic future (Vol. 2) : final report (English), 2017. https://doi.org/10.1596/26707.

[101] Global antimicrobial resistance and use surveillance system (GLASS) Report 2022, 2022. https://www.who.int/publications/i/item/9789240062702.

[102] C.O. Okoye, R. Nyaruaba, R.E. Ita, S.U. Okon, C.I. Addey, C.C. Ebido, A.O. Opabunmi, E.S. Okeke, K.I. Chukwudozie, Antibiotic resistance in the aquatic environment: Analytical techniques and interactive impact of emerging contaminants, Environ. Toxicol. Pharmacol. 96 (2022) 103995. https://doi.org/https://doi.org/10.1016/j.etap.2022.103995.

[103] P. Lucci, O. Núñez, M.T. Galceran, Solid-phase extraction using molecularly imprinted polymer for selective extraction of natural and synthetic estrogens from aqueous samples, J. Chromatogr. A 1218 (2011) 4828–4833. https://doi.org/https://doi.org/10.1016/j.chroma.2011.02.007.

[104] A.G. Ayankojo, J. Reut, V.B.C. Nguyen, R. Boroznjak, V. Syritski, Advances in Detection of Antibiotic Pollutants in Aqueous Media Using Molecular Imprinting Technique—A Review, Biosensors 12 (2022). https://doi.org/10.3390/bios12070441.

[105] N. Tarannum, S. Khatoon, B.B. Dzantiev, Perspective and application of

molecular imprinting approach for antibiotic detection in food and environmental samples: A critical review, Food Control 118 (2020) 107381. https://doi.org/10.1016/j.foodcont.2020.107381.

[106] L.A. Tom, N.A. Schneck, C. Walter, Improving the imprinting effect by optimizing template:monomer:cross-linker ratios in a molecularly imprinted polymer for sulfadimethoxine, J. Chromatogr. B Anal. Technol. Biomed. Life Sci. 909 (2012) 61–64. https://doi.org/10.1016/j.jchromb.2012.10.020.

[107] F. Barahona, B. Albero, J.L. Tadeo, A. Martín-Esteban, Molecularly imprinted polymer-hollow fiber microextraction of hydrophilic fluoroquinolone antibiotics in environmental waters and urine samples, J. Chromatogr. A 1587 (2019) 42–49. https://doi.org/10.1016/j.chroma.2018.12.015.

[108] J. Yin, Z. Meng, M. Du, C. Liu, M. Song, H. Wang, Pseudo-template molecularly imprinted polymer for selective screening of trace β-lactam antibiotics in river and tap water, J. Chromatogr. A 1217 (2010) 5420–5426. https://doi.org/10.1016/j.chroma.2010.06.044.

[109] L.R. Rocha, C.R.T. Tarley, Tetracyclines and an Overview of the Preconcentration/Extractions Method Based on Molecularly Imprinted Polymers, in: S. Patra, M. Sillanpaa (Eds.), Mol. Imprinted Polym. as Artif. Antibodies Environ. Heal., Springer, Cham, 2024. https://doi.org/https://doi.org/10.1007/978-3-031-58995-9_13.

[110] M.P. Divya, Y.S. Rajput, R. Sharma, Synthesis and application of tetracycline imprinted polymer, Anal. Lett. 43 (2010) 919–928. https://doi.org/10.1080/00032710903491039.

[111] W. Cai, R.B. Gupta, Molecularly-imprinted polymers selective for tetracycline binding, Sep. Purif. Technol. 35 (2004) 215–221. https://doi.org/10.1016/S1383-5866(03)00143-6.

[112] M. Sánchez-Polo, I. Velo-Gala, J.J. López-Peñalver, J. Rivera-Utrilla, Molecular imprinted polymer to remove tetracycline from aqueous solutions, Microporous Mesoporous Mater. 203 (2015) 32–40. https://doi.org/10.1016/j.micromeso.2014.10.022.

[113] R. Suedee, T. Srichana, T. Chuchome, U. Kongmark, Use of molecularly imprinted polymers from a mixture of tetracycline and its degradation products to produce affinity membranes for the removal of tetracycline from water, J. Chromatogr. B 811 (2004) 191–200. https://doi.org/10.1016/j.jchromb.2004.08.044.

[114] B.D. Abera, I. Ortiz-gómez, B. Shkodra, F.J. Romero, G. Cantarella, L. Petti, A. Salinas-castillo, P. Lugli, A. Rivadeneyra, Laser-induced graphene electrodes modified with a molecularly imprinted polymer for detection of tetracycline in milk and meat, Sensors 22 (2022) 1–17. https://doi.org/10.3390/s22010269.

[115] Y. Ma, X. Liao, Y. Zhao, L. Qiu, Y. Yao, S. Wang, X. Yang, X. Hu, Fabrication of magnetic molecularly imprinted polymers based on aptamers and β-cyclodextrin for synergistic recognition and separation of tetracycline, Anal. Chim. Acta 1236 (2022) 340572. https://doi.org/https://doi.org/10.1016/j.aca.2022.340572.

[116] E. Camilli, V. Bertana, F. Frascella, M. Cocuzza, S. Luigi, I. Roppolo, Digital light processing 3D printing of molecularly imprinted polymers for antibiotic removal, React. Funct. Polym. 208 (2025) 106164. https://doi.org/10.1016/j.reactfunctpolym.2025.106164.

[117] J.F.F. Aguilar, J.M. Miranda, J.A. Rodriguez, M.E. Paez-Hernandez, I.S. Ibarra, Selective removal of tetracycline residue in milk samples using a molecularly imprinted polymer, J. Polym. Res. 27 (2020). https://doi.org/10.1007/s10965-020-02139-9.

[118] J.W. Stansbury, M.J. Idacavage, 3D printing with polymers: Challenges among expanding options and opportunities, Dent. Mater. 32 (2016) 54–64. https://doi.org/10.1016/j.dental.2015.09.018.

[119] M. Gastaldi, F. Cardano, M. Zanetti, G. Viscardi, C. Barolo, S. Bordiga, S. Magdassi, A. Fin, I. Roppolo, Functional Dyes in Polymeric 3D Printing :, (2021). https://doi.org/10.1021/acsmaterialslett.0c00455.

[120] G. Gonzalez, A. Chiappone, K. Dietliker, C.F. Pirri, I. Roppolo, Fabrication and Functionalization of 3D Printed Polydimethylsiloxane-Based Microfluidic Devices Obtained through Digital Light Processing, Adv. Mater. Technol. 5 (2020) 1–10. https://doi.org/10.1002/admt.202000374.

[121] No Title, (n.d.). https://webbook.nist.gov/cgi/cbook.cgi?ID=C67685&Type=IR-SPEC&Index=2#Refs.

[122] P. Cervini, B. Ambrozini, L.C.M. Machado, A.P.G. Ferreira, E.T.G. Cavalheiro, Thermal behavior and decomposition of oxytetracycline hydrochloride, J. Therm. Anal. Calorim. (2015). https://doi.org/10.1007/s10973-015-4447-x.

[123] R. Gabai, N. Sallacan, V. Chegel, T. Bourenko, E. Katz, I. Willner,

Characterization of the swelling of acrylamidophenylboronic acid-acrylamide hydrogels upon interaction with glucose by faradaic impedance spectroscopy, chronopotentiometry, quartz-crystal microbalance (QCM), and surface plasmon resonance (SPR) experiments, J. Phys. Chem. B 105 (2001) 8196–8202. https://doi.org/10.1021/jp0111618.

[124] P.S. Sharma, A. Pietrzyk-Le, F. D'Souza, W. Kutner, Electrochemically synthesized polymers in molecular imprinting for chemical sensing, Anal. Bioanal. Chem. 402 (2012) 3177–3204. https://doi.org/10.1007/s00216-011-5696-6.

[125] X. Li, Y. He, F. Zhao, W. Zhang, Z. Ye, Molecularly imprinted polymer-based sensors for atrazine detection by electropolymerization of o-phenylenediamine, RSC Adv. 5 (2015) 56534–56540. https://doi.org/10.1039/c5ra09556e.

[126] W. Lian, S. Liu, J. Yu, J. Li, M. Cui, W. Xu, J. Huang, Determination of Oxytetracycline with a Gold Electrode Modified by Chitosan-Multiwalled Carbon Nanotube Multilayer Films and Gold Nanoparticles, Anal. Lett. 46 (2013) 1117–1131. https://doi.org/10.1080/00032719.2012.751540.

[127] Y. Sasaki, Y. Zhang, H. Fan, K. Ohshiro, Q. Zhou, W. Tang, X. Lyu, T. Minami, Accurate cortisol detection in human saliva by an extended-gate-type organic transistor functionalized with a molecularly imprinted polymer, Sensors Actuators B Chem. 382 (2023) 133458. https://doi.org/10.1016/j.snb.2023.133458.

[128] Q. Zhou, Y. Sasaki, K. Ohshiro, H. Fan, V. Montagna, C. Gonzato, K. Haupt, T. Minami, An organic transistor for the selective detection of tropane alkaloids utilizing a molecularly imprinted polymer, J. Mater. Chem. B 10 (2022) 6808–6815. https://doi.org/10.1039/d2tb01067d.

[129] J. Li, F. Jiang, X. Wei, Molecularly imprinted sensor based on an enzyme amplifier for ultratrace oxytetracycline determination, Anal. Chem. 82 (2010) 6074–6078. https://doi.org/10.1021/ac100667m.

[130] S. Yeasmin, B. Wu, Y. Liu, A. Ullah, L.-J. Cheng, Nano gold-doped molecularly imprinted electrochemical sensor for rapid and ultrasensitive cortisol detection, Biosens. Bioelectron. 114142 (2022). https://doi.org/https://doi.org/10.1016/j.bios.2022.114142.

[131] D. Kealey, P.J. Haines, Electrochemical Methods - Fundamentals And Applications, 2020. https://doi.org/10.4324/9780203645444-14.

[132] Y. Koç, U. Morali, S. Erol, H. Avci, Investigation of electrochemical

behavior of potassium ferricyanide/ferrocyanide redox probes on screen printed carbon electrode through cyclic voltammetry and electrochemical impedance spectroscopy, Turkish J. Chem. 45 (2021) 1895–1915. https://doi.org/10.3906/kim-2105-55.

[133] W.T. Ting, M.J. Wang, M.M.R. Howlader, Interleukin-6 electrochemical sensor using poly(o-phenylenediamine)-based molecularly imprinted polymer, Sensors Actuators B Chem. 404 (2024) 135282. https://doi.org/10.1016/j.snb.2024.135282.